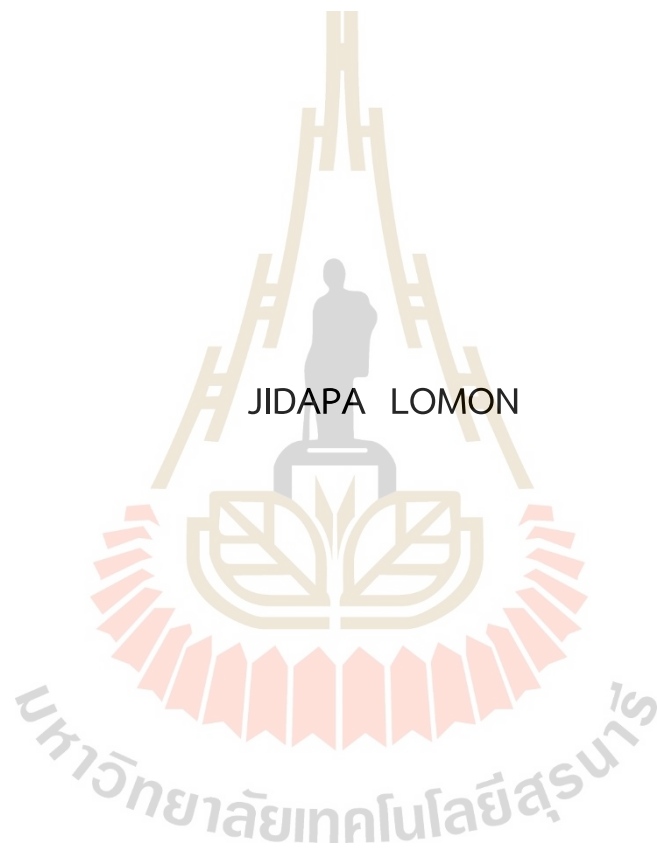


DEVELOPMENT OF LITHIUM BORATE BASED GLASS DOPED WITH  
TRANSITION METALS FOR BATTERY CATHODE



A Thesis Submitted in Partial Fulfillment of the Requirements for the  
Degree of Doctor of Philosophy in Applied Physics  
Suranaree University of Technology  
Academic Year 2023

การพัฒนาแก้วลิเทียมบอเรตเจือด้วยโลหะทรานซิชัน  
เพื่อใช้เป็นแคโทดของแบตเตอรี่



นางสาวจิตาภา ลมอ่อน

วิทยานิพนธ์นี้เป็นส่วนหนึ่งของการศึกษาตามหลักสูตรปริญญาวิทยาศาสตรดุษฎีบัณฑิต

สาขาวิชาฟิสิกส์ประยุกต์

มหาวิทยาลัยเทคโนโลยีสุรนารี

ปีการศึกษา 2566

DEVELOPMENT OF LITHIUM BORATE BASED GLASS DOPED WITH  
TRANSITION METALS FOR CATHODE OF GLASS BATTERY

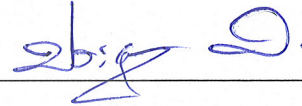
Suranaree University of Technology has approved this thesis submitted in  
partial fulfillment of the requirements for the Degree of Doctor of Philosophy.

Thesis Examining Committee



(Prof. Dr. Supree Pinitsoontorn)

Chairperson



(Assoc. Prof. Dr. Prayoon Songsiriritthigul)

Member (Thesis Advisor)



(Dr. Pinit Kidkhunthod)

Member (Thesis Co-Advisor)



(Asst. Prof. Dr. Nattapol Laorodphan)

Member



(Dr. Wiwat Nuansing)

Member



(Assoc. Prof. Dr. Yupaporn Ruksakulpiwat)

Vice Rector for Academic Affairs

and Quality Assurance



(Prof. Dr. Santi Maensiri)

Dean of Institute of Science

จิตาภา ลมอ่อน : พัฒนาแก้วลิเทียมบอเรตเจือด้วยโลหะทรานซิชันเพื่อใช้เป็นแคโทดของ  
แบตเตอรี่ (DEVELOPMENT OF LITHIUM BORATE BASED GLASS DOPED WITH  
TRANSITION METALS FOR BATTERY CATHODE) อาจารย์ที่ปรึกษา : รองศาสตราจารย์  
ดร.ประยูร ส่งสิริฤทธิกุล, 119 หน้า

คำสำคัญ : แก้วลิเทียมบอเรต/ นิกเกิล-แมงกานีส-โคบอลต์/ แบตเตอรี่แก้ว/วิธีการหลอมแล้วทำให้  
เย็นตัวลง / ไซคลิกโวลแทมเมทรี

วิทยานิพนธ์มุ่งเน้นไปที่การพัฒนาส่วนประกอบแก้วลิเทียมบอเรตเพื่อวัตถุประสงค์ในการใช้  
แบตเตอรี่แก้ว ซึ่งทำได้โดยการนำโลหะทรานซิชันมารวมกันในสัดส่วนที่ต่างกัน กระบวนการผลิตแก้ว  
เกี่ยวข้องกับวิธีการหลอมแล้วทำให้เย็นตัวลง เทคนิคการเลี้ยวเบนรังสีเอกซ์ ใช้เพื่อศึกษาโครงสร้าง  
ของแก้วลิเทียมบอเรตที่ได้รับอย่างเป็นระบบ การตรวจสอบสถานะออกซิเดชันของแก้วดำเนินการ  
โดยใช้เทคโนโลยีแสงซินโครตรอน การดูดกลืนรังสีเอกซ์ ครอบคลุมสองเทคนิค: การแยกสเปกตรัม  
การดูดกลืนรังสีเอกซ์ใกล้ขอบพลังงาน และเทคนิคสเปกโทรสโกปีของอนุภาคอิเล็กทรอนิกส์ที่ถูก  
ปลดปล่อยด้วยรังสีเอกซ์ เพื่อตรวจสอบคุณสมบัติทางแม่เหล็กของแก้วที่ผลิตได้ มีการใช้แมกนีโต  
มิเตอร์ตัวอย่างแบบสั้น ต่อจากนั้น ตัวอย่างแก้วลิเทียมบอเรตที่เจือด้วยโลหะทรานซิชันได้รับการ  
วิเคราะห์เพื่อหาคุณลักษณะทางเคมีไฟฟ้าโดยใช้เทคนิคไซคลิกโวลแทมเมทรี ผลการวิจัยระบุว่า  
คุณลักษณะภายนอกของแก้วบอเรตอาจมีการปรับเปลี่ยนตามชนิดและสัดส่วนของโลหะทรานซิชันที่  
รวมอยู่ในชิ้นงานทดสอบ โดยตัวอย่างทั้งหมดมีสีน้ำตาลและม่วงเข้มซึ่งเกิดจากนิกเกิลและโคบอลต์  
ผลจากการศึกษาสถานะออกซิเดชันของแก้วลิเทียมบอเรตที่เจือด้วยโลหะทรานซิชันประกอบด้วย  
 $Mn^{2+}$ ,  $Mn^{3+}$ ,  $Co^{2+}$  และ  $Ni^{2+}$  สถานะออกซิเดชันเหล่านี้เกิดการเปลี่ยนแปลงเมื่อปริมาณนิกเกิลใน  
ตัวอย่างเพิ่มขึ้น ซึ่งส่งผลอย่างมากต่อสมบัติไฟฟ้าเคมีและสมบัติทางแม่เหล็กของตัวอย่าง จากผลการ  
วิเคราะห์ของตัวอย่างของแก้วลิเทียมบอเรตทั้งหมด พบว่าเมื่อแก้วลิเทียมบอเรตเจือด้วยนิกเกิลและ  
โคบอลต์ในอัตราส่วน 4:1 จะแสดงคุณลักษณะทางเคมีไฟฟ้าที่เหนือกว่าการเตรียมแก้วลิเทียมบอเรต  
ที่เจือด้วยโลหะทรานซิชันในอัตราส่วนอื่น ซึ่งแสดงค่าที่บันทึกไว้สูงถึง 122 F/g

สาขาวิชาฟิสิกส์  
ปีการศึกษา 2566

ลายมือชื่อนักศึกษา จิตาภา ลมอ่อน  
ลายมือชื่ออาจารย์ที่ปรึกษา ประยูร ส่งสิริฤทธิกุล  
ลายมือชื่ออาจารย์ที่ปรึกษาร่วม ปณิต ฤทธิกุล

JIDAPA LOMON : DEVELOPMENT OF LITHIUM BORATE BASED GLASS DOPED WITH  
TRANSITION METALS FOR BATTERY CATHODE. THESIS ADVISOR : ASSOC. PROF.  
PRAYOON SONGSIRIRITTHIGUL, Ph.D. 119 PP.

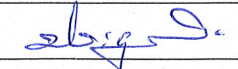
Keyword: Lithium-borate glass / melting-quenching technique / XAS / XPS / VSM /  
cyclic voltammetry / NMC / Glass battery.

The thesis focuses on the development of lithium-borate glass compositions for the purpose of glass batteries, achieved through the incorporation of transition metals in different proportions. The process of glass production involves the melting-quenching technique. The X-ray diffraction (XRD) technique was employed to systematically study the structure of the obtained lithium borate glasses. The investigation of the oxidation status of the glass was conducted utilizing synchrotron light technology. X-ray absorption spectroscopy (XAS) encompasses two techniques: X-ray absorption near edge structure (XANES) and X-ray electron spectroscopy (XPS). In order to investigate the magnetic properties of the produced glass, a vibrating sample magnetometer (VSM) was used. Subsequently, the lithium-borate glass samples doped with transition metals were analyzed for their electrochemical characteristics using the cyclic voltammetry (CV) technique. The findings show that the kind and quantity of transition metals present in the specimen may have an impact on the exterior properties of borate glass. All of the samples are colored a deep brownish-purple due to the presence of nickel and cobalt. Lithium borate glass was doped with  $Mn^{2+}$ ,  $Mn^{3+}$ ,  $Co^{2+}$ , and  $Ni^{2+}$ . Their oxidation states were investigated. These oxidation states shifted as nickel concentrations in the sample grew. This considerably impacts the electrochemical and magnetic characteristics of the sample. The electrochemical properties of manufactured lithium borate glass at a constant temperature were found to be superior when the glass was doped with nickel and

cobalt at a ratio of 4:1. The highest measured value for this component is 122 F/g.



School of Physics  
Academic Year 2023

Student's signature   
Advisor's signature   
Co-advisor's signature Pinitk.

## ACKNOWLEDGEMENT

The successful completion of this thesis would not have been possible without the invaluable support and assistance provided by numerous individuals. I would like to extend my heartfelt appreciation for their invaluable support.

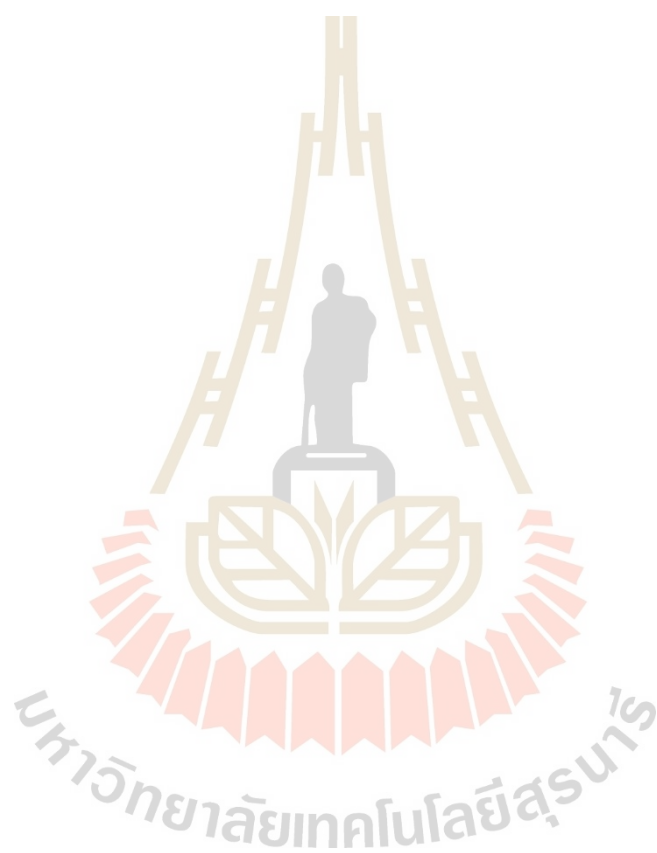
I would like to express my gratitude to Assoc. Prof. Dr. Prayoon Songsiriritthigul for serving as my thesis adviser during my PhD study and research. I am really thankful for the unwavering support provided throughout my academic endeavor. I appreciate the insightful talks and the valuable knowledge shared, particularly in terms of guiding my research efforts towards presenting the research findings with the utmost clarity. I am deeply grateful and privileged to have the opportunity to work and study under your esteemed leadership. I express my appreciation to my co-advisor, Dr. Pinit Kidkhunthod, for continually providing me with possibilities for novel collaborations that have yielded exceptional achievements. Whenever I encountered a state of perplexity, he provided guidance in the form of a robust strategy aimed at identifying a single solution to address the situation at hand. I would like to extend my heartfelt gratitude to Prof. Dr. Supree Pinitsoontorn for their valuable contribution as a member of my thesis committee. I express my gratitude to Dr. Wiwat Nuansing and Assistant Professor Dr. Nattapol Laorodphan for their perceptive inquiries and constructive feedback on my thesis.

I would like to express my gratitude to the staff members at the Novel Glass Laboratory, namely Dr. Jintara Padchagri, Sumeth Siriroj, and Mr. Amorntep, for their guidance and instruction in the process of manufacturing LiBO<sub>3</sub> using the Melt-Quenching Technique. The individual provided guidance and assistance at moments of confusion, aiding in the exploration of potential solutions to the given problem. Furthermore, They provided assistance in the process of revising the manuscript.

I would like to extend my sincere appreciation to the entire staff at the School of Physics for their invaluable contributions in facilitating my academic growth. Their enlightening lectures, extensive documentation, and insightful insights shared during seminars have greatly enhanced my understanding of the subject matter. Additionally, I would like to extend my appreciation to the students at the Institute of Science for

their steadfast camaraderie. In closing, I would like to extend my sincere appreciation to my parents, whose unwavering support has been vital in facilitating my personal and academic growth.

Jidapa Lomon



# CONTENTS

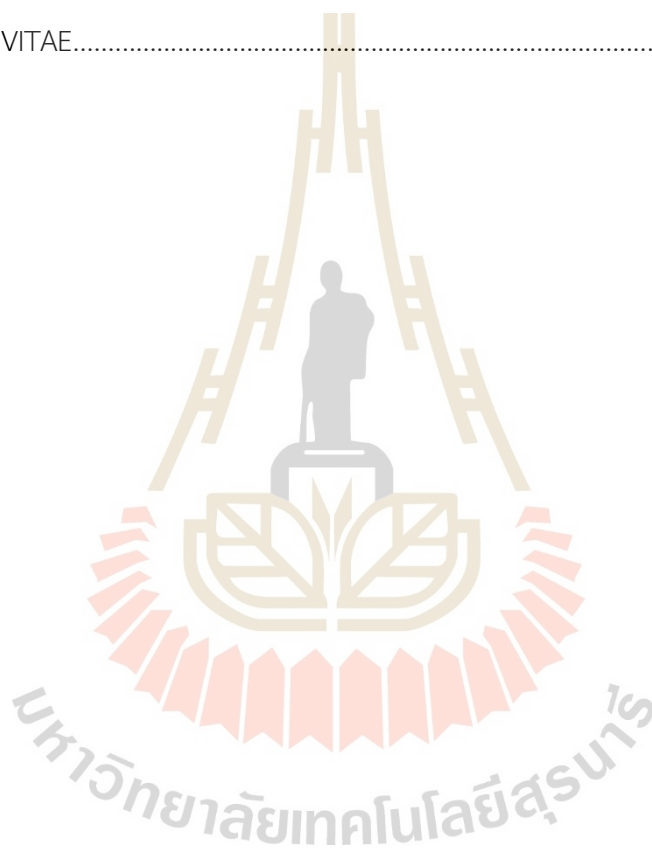
	Page
ABSTRACT IN THAI.....	I
ABSTRACT IN ENGLISH.....	II
ACKNOWLEDGEMENT.....	IV
CONTENTS.....	VI
LIST OF TABLES.....	IX
LIST OF FIGURES.....	X
LIST OF ABBREVIATIONS.....	XVI
<b>CHAPTER</b>	
<b>I INTRODUCTION.....</b>	<b>1</b>
<b>II BACKGROUND.....</b>	<b>4</b>
2.1 HISTORY OF GLASS.....	4
2.2 Glass on battery electrod.....	7
2.2.1 B <sub>2</sub> O <sub>3</sub> glass electrod.....	11
2.2.2 Effect of transition metal doping.....	12
2.3 Glass production.....	25
2.3.1 Melt-Quenching Technique.....	25
2.4 Characterization techniques.....	27
2.4.1 Synchrotron radiation.....	27
2.4.2 The X-ray photoelectron spectroscopy (XPS).....	35
2.4.3 X-ray absorption spectroscopy (XAS).....	43
2.4.4 X-ray diffraction (XRD).....	47
2.4.5 Scanning electron microscopy (SEM) and Energy Dispersive X-Ray Spectroscopy (EDX).....	52
2.4.6 The vibrating sample magnetometer (VSM).....	54
2.4.7 The cyclic voltammetry (CV).....	59

## CONTENTS (Continued)

		Page
	2.5 Background of research.....	63
<b>III</b>	<b>EXPERIMENTAL .....</b>	<b>68</b>
	3.1 Materials.....	68
	3.2 Glass preparation.....	68
	3.2.1 Characterization process.....	70
	3.2.2 Electrochemical process.....	70
	3.3 Instrumentation.....	71
<b>IV</b>	<b>RESULT AND DISCUSSION.....</b>	<b>79</b>
	4.1 Single-Doping.....	79
	4.1.1 Physical characteristics.....	79
	4.1.2 Phase identification.....	80
	4.1.3 Optical gap energy analysis.....	82
	4.1.4 XPS and XANES analyses.....	83
	4.1.5 Magnetic property.....	85
	4.1.6 Electrochemical properties.....	86
	4.2 Co-Doping.....	87
	4.2.1 Physical characteristics.....	87
	4.2.2 Phase identification.....	88
	4.2.3 Optical gap energy analysis.....	91
	4.2.4 XPS and XANES analyses.....	93
	4.2.5 Magnetic property.....	97
	4.2.6 Electrochemical properties.....	98
	4.3 Triple-Doping.....	100
	4.3.1 Physical characteristics.....	100
	4.3.2 Phase identification.....	101
	4.3.3 Optical gap energy analysis.....	103
	4.3.4 XPS and XANES analyses.....	104

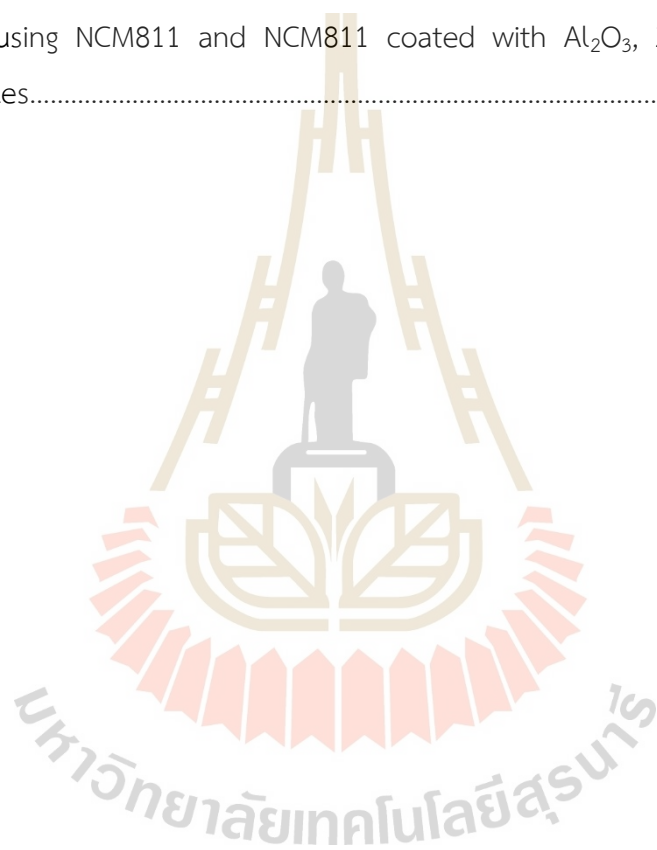
## CONTENTS (Continued)

	Page
4.3.5 Magnetic property.....	107
4.3.6 Electrochemical properties.....	107
<b>V CONCLUSION.....</b>	<b>109</b>
REFERENCES.....	112
CURRICULUM VITAE.....	119



## LIST OF TABLES

Table		Page
2.1	The electrochemical data of $\text{LiMBO}_3$ (M = Fe, Mn, Co, Zn).....	23
2.2	The initial charge and discharge capacities of the coin lithium-ion battery (LIB) using NCM811 and NCM811 coated with $\text{Al}_2\text{O}_3$ , $\text{ZrO}_2$ , and LBO samples.....	65



## LIST OF FIGURES

Figure	Page
2.1	Overview of the evolution of battery technology..... 5
2.2	John B. Goodenough..... 7
2.3	Charge and discharge curves for a cathode made of (a) $V_2O_5$ (b) $c-V_2O_5$ cathode with current densities ranging from 1.0 to 4.0 V, and (c) a comparison of the two cathodes rate performance..... 9
2.4	LIBs with amorphous and crystal Metfv10 cathodes: a) first discharge and second charge curves; and b) cycle performance..... 10
2.5	a) The standard charge - discharge trends of a $LiFeBO_3$ cell at current levels of 5 mA/g, 10 mA/g, 20 mA/g, and 50 mA/g and b) at 5 mA/g current density..... 13
2.6	(a) The initial ten charge/discharge profiles of the $RGO/V_2O_5-LiBO_2$ glass composite were obtained within a potential range of 1.5–4.0 V using a current density of 50 mA/g, (b) the rate capacity of the $RGO/V_2O_5 - LiBO_2$ glass composite at room temperature ranges from 1.5 V to 4.0 V for 50, 100, 200, and 400 mA/g, (c) Discharge capacity against number of cycles for an $RGO/V_2O_5-LiBO_2$ glass composite discharging at 50 and 100 mA/g..... 15
2.7	a) Four initial charge-discharge curves for amorphous nano-spheres in the 4.5–2.0 V, C/20 potential range; b) the initial ten C/D curves of the carbon/Nano h- $LiMnBO_3$ composite operating in the 4.5 V to 2.0 V, C/15 potential range; and c) the discharge capacity of the carbon/Nano h- $LiMnBO_3$ composite as a function of the number of cycles at a C/15 rate and a voltage range of 4.5–2.0 V..... 16
2.8	The LBV glass crystallized on the LLZ substrate at 750 C for 0.5 min, and the charge-discharge curves of the $LBV_jLLZ_jGaAg$ cell. Under 1 (a) or 50 (b) mA, (2.6 and 130 mA $cm^2$ , respectively), the active electrode was

## LIST OF FIGURES (Continued)

Figure		Page
	determined to be composed of LBV glass .....	17
2.9	Ex-situ V 2p2/XPS spectra of the LVSB10 electrode at (c) 4.2 V and (d)1.5 V for the first cycle, and charge/discharge curves of the LVSB <sub>10</sub> , LVSB <sub>20</sub> , LVSB <sub>30</sub> , and LVSB <sub>40</sub> glass samples after (a) 1st cycle and (b) 50th cycle.....	18
2.10	illustrates the electrochemical capabilities of LiZnBO <sub>3</sub> /C. (a) The performance of the cycle at a current density of 100 mA/g (b) The performances at different current densities (c) The long-term cycle performance at a current density of 500 mA/g.....	19
2.11	a) Initial galvanostatic voltage profiles of the sample at 0.2 °C and voltages between 1.5 and 4.2 volts, b) The performance of LVBO at a cycling rate of 0.2 °C, and c) The galvanostatic voltage profiles of LVBO over the initial six cycles are presented.....	21
2.12	Scatter plots of measured capacitance versus sampling frequencies of 0.3MnO <sub>2</sub> -0.7 (Li <sub>x</sub> BO <sub>2</sub> ) glasses.....	22
2.13	a schematic depiction of the various stages involved in the melt-quenching method of glassmaking.....	26
2.14	X-ray diffraction spectroscopy of xLi <sub>2</sub> O-B <sub>2</sub> O <sub>3</sub> -yCuO, where x = 0.1 and y = 0.005–0.05.....	27
2.15	Core components of the synchrotron.....	28
2.16	The spectrum range of the synchrotron radiation.....	30
2.17	Both linear and circular polarizations of synchrotron radiation exist.....	31
2.18	The core of the Synchrotron Light Institute for Medical Research.....	33
2.19	Within the atom resides the electrical state.....	36
2.20	Energy level diagrams illustrate the fundamental XPS equation, which encompasses the x-ray source energy (h), electron binding energy (BE), measured electron kinetic energy (KE <sub>measured</sub> ), and The work function of the spectrometer.....	38

## LIST OF FIGURES (Continued)

Figure		Page
2.21	The kinetic energy of the electrons emitted in XPS is determined by irradiating the sample with x-rays of low energy.....	39
2.22	XPS spectra of a) Mg source and b) Monochromatic source.....	41
2.23	A focused examination of the C1s area reveals distinct chemical shifts attributed to various bonding states involving oxygen.....	42
2.24	X-ray absorption process schematic.....	44
2.25	a) XANES and EXAFS spectra of the manganese K edge. Upper left: XANES and EXAFS regions of XAS spectrum of a PS II sample, b) A diagram showing the propagating and reflected photoelectron wave, which represents interference in EXAFS. The central (blue) atom absorbs and the surrounding atoms backscatter the photoelectron (red). The backscattered wave (blue dashed lines) is in phase with the outgoing wave (solid blue circular lines).....	46
2.26	A simplified model of the Bragg equation.....	50
2.27	Amorphous sucrose (a) and crystalline sucrose (b) in powder X-ray diffraction patterns.....	52
2.28	Illustrates the setup of SEM system together with the inclusion of EDS capabilities.....	54
2.29	A representation in schematic form of the VSM.....	55
2.30	Illustrates a magnet that has lost its magnetization when placed with in a magnetic field.....	57
2.31	Graphs the magnetic (M) and electric (B) hysteresis loops versus applied magnetic field (H).....	58
2.32	Basic Equivalent Circuit Models and Their Corresponding Impedance Plots.....	59
2.33	The relationship between potential and time during cyclic voltammetry, with the vertex potentials ( $E_{\text{vertex}}$ ), the formal potential of the species being researched ( $E^{\circ}$ ), and the scan rate ( $v$ ) highlight.....	61

## LIST OF FIGURES (Continued)

Figure		Page
2.34	The CV of a reversible species that diffuses easily, together with an indication of the anodic and cathodic maxima in current and potential, respectively.....	62
2.35	The initial charge - discharge curves of NCM811 and NCM811 with various coatings (A, uncoated; B, Al <sub>2</sub> O <sub>3</sub> ; C, ZrO <sub>2</sub> ; D, LBO) on both sides of the coin.....	64
2.36	(a)-(d) Cycling performance for bare and 0.5, 1.0, and 2 wt% of Li <sub>2</sub> O-2B <sub>2</sub> O <sub>3</sub> glass ceramic oxide coated NCM811 materials at room temperature; (e) Rate capability for bare and 0.5, 1.0, and 2.0 wt% of Li <sub>2</sub> O-2B <sub>2</sub> O <sub>3</sub> glass ceramic oxide coated NCM811 materials at different current rates, and (f) Specific capacity vs. current density diagram for bare and 0.5, 1.0, and 2.0 wt% of Li <sub>2</sub> O-2B <sub>2</sub> O <sub>3</sub> glass ceramic oxide coated NCM811 materials at different current rates.....	66
3.1	Depicts the procedure followed for preparing Lithium-borate glass samples.....	69
3.2	The process of incorporating a transition metal into a glass sample.....	69
3.3	SmartLab automated multipurpose XRD.....	72
3.4	Scanning Electron Microscope QUANTA 450.....	73
3.5	Tecnai G2 20 S-TWIN Transmission Electron Microscope.....	74
3.6	Quantum Design VersaLab VSM.....	75
3.7	Metrohm Autolab PGSTAT302N at SLRI.....	76
3.8	BL5.2 : SUT-NANOTEC-SLRI XAS Beamline.....	77
3.9	PHI 5000 Versaprobe-II Focus XPS at SLRI.....	78
4.1	Prepared xNi: LiBO <sub>3</sub> plate glasses where x = 0 (a), 0.15 (b), 0.20 (c) and 0.25 (d).....	79
4.2	XRD patterns of the xNi: LiBO <sub>3</sub> glass system are being investigated, where x represents the varying compositions of 0, 0.15, 0.20, and 0.25..	80
4.3	TEM image and electron diffraction of xNi:LiBO <sub>3</sub> glass system where	

## LIST OF FIGURES (Continued)

Figure	Page
a,d) $x = 0.15$ , b,e) $x = 0.20$ and c,f) $x = 0.25$ .....	81
4.4 EDS spectra of $x\text{Ni}:\text{LiBO}_3$ glass system where a) $x = 0.15$ , b) $x = 0.20$ and c) $x = 0.25$ .....	82
4.5 Absorbance spectra of the optical variety for the $x\text{Ni}:\text{LiBO}_3$ glass system for (a), (b), and (c) $x = 0.15$ , $0.20$ , and $0.25$ , respectively.....	83
4.6 XPS spectra for three different $x\text{Ni}:\text{LiBO}_3$ glass samples, namely (a) $x = 0.15$ , (b) $x = 0.20$ , and (c) $x = 0.25$ .....	84
4.7 XANES spectra for a) the nickel (Ni) K-edge and b) the first derivative of the Ni K-edge of a glass system consisting of $\text{LiBO}_3$ doped with varying concentrations of NiO ( $x = 0.15$ , $0.20$ , and $0.25$ ).....	85
4.8 The present study investigates the relationship between magnetization (M) and magnetic field (H) in the $x\text{Ni}:\text{LiBO}_3$ glass system.....	86
4.9 a) CV analysis on the $x\text{Ni}:\text{LiBO}_3$ glass system using a scan rate of $5\text{ mV/s}$ b) The $\text{LiBO}_3$ -based glass system with scan rates of $5\text{ mV/s}$ ; c) A graphical representation illustrates the relationship between specific capacitance and scan rates).....	87
4.10 Prepared $x\text{Ni}_y\text{Mn}:\text{LiBO}_3$ plate glasses where $y=1$ and $x = 1, 2, 3$ and $4$ .....	88
4.11 $x\text{Ni}_y\text{Co}:\text{LiBO}_3$ plate glasses where $y=1$ and $x = 1, 2, 3$ and $4$ .....	88
4.12 XRD patterns of lithium borate glass system that had been doped with nickel manganese and nickel cobalt.....	89
4.13 TEM image and electron diffraction of $x\text{Ni}_y\text{Mn}:\text{LiBO}_3$ glass system where $X= 1, 2, 3$ and $4$ and $y =1$ .....	90
4.14 EDS spectra of $x\text{Ni}_y\text{Co}:\text{LiBO}_3$ (with $x$ values of $1, 2, 3, 4$ , and $y =1$ ).....	90
4.15 Optical absorbance spectra of $x\text{Ni}_y\text{Mn}:\text{LiBO}_3$ (with $x$ values of $1, 2, 3, 4$ , and $y$ values of $1$ ).....	91
4.16 Optical absorbance spectra of $x\text{Ni}_y\text{Co}:\text{LiBO}_3$ (with $x$ values of $1, 2, 3, 4$ , and $y$ values of $1$ ).....	92

## LIST OF FIGURES (Continued)

Figure	Page
4.17 XPS spectra were obtained for a series of $\text{LiBO}_3$ glass samples containing $x\text{Ni}_y\text{Mn}$ , where $y$ is fixed at 1 and $x$ varies from 1 to 4.....	93
4.18 XANES spectra of a) Ni K-edge and the first derivative of Ni K-edge; b) Investigation of the Mn K-edge and its first derivative in the $\text{LiBO}_3$ doped with NiMn glass system.....	94
4.19 XPS spectra of a series of $\text{LiBO}_3$ glass samples containing $x\text{Ni}_y\text{Co}$ , where $y$ is fixed at 1 and $x$ varies from 1 to 4.....	95
4.20 $\text{LiBO}_3$ doped with NiCo glass system XANES spectra of a) Ni K-edge and first derivative of Ni K-edge, b) Co K-edge and first derivative of Co K-edge.....	96
4.21 The magnetization ( $M$ ) versus magnetic field ( $H$ ) of $x\text{Ni}_y\text{Mn}:\text{LiBO}_3$ glass system.....	97
4.22 The magnetization ( $M$ ) versus magnetic field ( $H$ ) of $x\text{Ni}_y\text{Co}:\text{LiBO}_3$ (where $x = 1, 2, 3, 4$ , and $y = 1$ ) glass system.....	98
4.23 a) The characterization of the $x\text{Ni}_y\text{Mn}:\text{LiBO}_3$ glass system was conducted using scan rates of 5 mV/s, b) A graphical representation of the relationship between scan rates and specific capacitance.....	99
4.24 a) The characterization of the $x\text{Ni}_y\text{Co}:\text{LiBO}_3$ glass system using scan rates of 5 mV/s, and b) A graphical representation to illustrate the relationship between scan rates and specific capacitance in the $\text{LiBO}_3$ glass system.....	100
4.25 Prepared $x\text{Ni}_y\text{Mn}_z\text{Co}:\text{LiBO}_3$ plate glasses where $y = 1, z = 1$ and $x = 1, 2, 3$ and 4.....	101
4.26 XRD patterns of $x\text{Ni}_y\text{Mn}_z\text{Co}:\text{LiBO}_3$ plate glasses where $y = 1, z = 1$ and $x = 1, 2, 3$ and 4.....	102
4.27 EDS spectra of $x\text{Ni}_y\text{Co}:\text{LiBO}_3$ (with $x$ values of 1, 2, 3, 4, and $y=1$ ).....	102
4.28 Optical absorbance spectra of $x\text{Ni}_y\text{Mn}_z\text{Co}:\text{LiBO}_3$ (with $x$ values of 1, 2, 3, 4, and $y, z$ values of 1).....	103

## LIST OF FIGURES (Continued)

Figure	Page
4.29 XPS spectra of NMC:LiBO <sub>3</sub> glass.....	104
4.30 XANES spectra of a) Ni K-edge, b) Mn K-edge, c) Co K-edge, d) first derivative of Ni K-edge, e) first derivative of Mn K-edge and f) first derivative of Co K-edge of LiBO <sub>3</sub> doped with NMC glass system.....	106
4.31 The magnetization (M) versus magnetic field (H) of xNiyMnzCo:LiBO <sub>3</sub> (where x = 1, 2, 3, and y and z = 1) glass system.....	107
4.31 a) CV analysis was performed on the LiBO <sub>3</sub> glass system using a scan rate of 5 mV/s, and b) The specific capacitance was shown as a function of scan rates for the LiBO <sub>3</sub> glass system.....	108

# CHAPTER I

## INTRODUCTION

The urgent need of establishing a stable and sustainable energy source to accommodate the growing demands of our rapidly advancing society is a significant challenge. Despite the fact that there is enough coal in the earth's crust to last for hundreds of years as a source of energy, the continued misuse of this finite resource could have disastrous effects on the climate. Moreover, in regard to the supply of crude oil, we have already passed the maximum production. Consequently, there will be a rise in demand for more clean, renewable energy sources worldwide (Heinberger et al., 2010; Xinxuan et al., 2020). Lithium-ion (Li-ion) batteries are among the most sophisticated and long-lasting energy storage technologies now on the market. Li-ion batteries are popular in consumer gadgets because of their high energy density and portability (Swiderska et al., 2016).

Increasing the quality of the cathode materials is one strategy for enhancing the performance of the LIB. This is due to the fact that the cathode material has a crucial influence in deciding how much energy LIBs are capable of storing at their highest capacity. Electrode materials for LIBs have typically been crystals until recently. The development of cathode materials is partly restricted since high-capacity crystalline solids are typically expensive materials. Crystalline solids with a large capacity are, however, notorious for being both expensive and difficult to produce. Therefore, the creation of crystalline cathode materials is fraught with a great deal of difficulty (Uchaker et al., 2014; Wang et al., 2018).

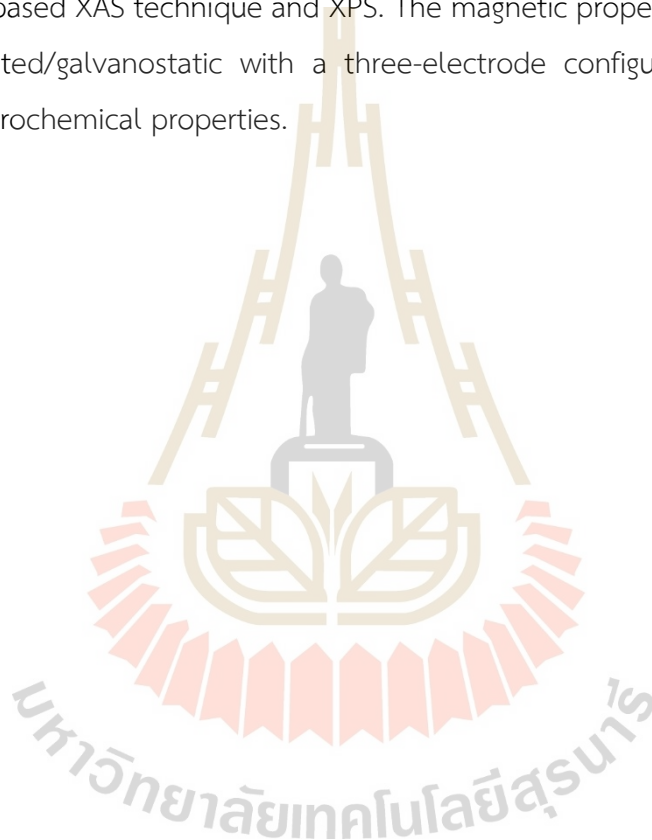
The performance of LIB can be enhanced by enhancing the cathode materials. This is due to the fact that the cathode material has a substantial impact on the maximum capacity of LIBs. Electrode materials for LIBs have typically been crystals until recently. However, high-capacity crystalline solids are typically costly materials, limiting the advancement of cathode materials. However, crystalline solids with large

capacities are notoriously costly and labor-intensive to produce. Therefore, there are various constraints on the development of crystalline cathode materials (Uchaker et al., 2014; Wang et al., 2018). The electrochemical performance of amorphous electrode materials may exceed that of their crystalline counterparts. Amorphous electrodes possess a structure characterized by short-range order, a significant surface area, and a free volume. This unique combination allows for lattice distortion to take place without inducing macroscopic phase transitions, hence enhancing kinetics. (Zhao et al., 2016).

Due to its diverse electronic and electrochemical properties, lithium borate-based glass has been widely examined as an electrode material for rechargeable batteries. For instance, borate is the lightest ionic group that results in the capacity and conductivity of Li-contained borates being very high (Zeng et al., 2020). Borates have higher theoretical capacities than the other types of inorganic salts (Yang et al., 2021). For polyanion-type cathode materials,  $\text{LiMBO}_3$  borates have higher specific capacities (200 mAh/g) than  $\text{LiFePO}_4$  phosphate, the most successful and famous one (170 mAh/g) (Yamada et al., 2010). However, the specific capacities are low when compared with other types of cathode materials. Different methods have been proposed to solve this problem. One of the interesting ways is doping some elements into lithium borate glass, such as,  $\text{FeC}_2\text{O}_4 \cdot 2\text{H}_2\text{O}$  (Dong et al., 2008),  $\text{V}_2\text{O}_5$  (Afyon et al., 2014), and  $\text{MnO}_2$  (Butnoi et al., 2019). One possible candidate is transition metal oxides such as cobalt oxides, nickel oxides, and manganese oxides. They have been widely used as based materials for cathode materials in lithium-ion batteries. Lithium nickel manganese cobalt oxide cathode material ( $\text{Li}_x\text{Ni}_y\text{Mn}_z\text{Co}_{1-y-z}\text{O}_2$ ,  $0 < x, y, z < 1$ , abbreviated NMC) showed a high specific capacity of over 160 mAh/g under a working voltage of 3.8 V (Hang et al., 2016). Therefore, the remodeling of Ni-rich  $\text{LiNi}_x\text{Mn}_y\text{Co}_z\text{O}_2$  (NMC) ( $x > y, z$ ) into an amorphous material cathode by using  $\text{Li}_2\text{O}-\text{B}_2\text{O}_3$  glasses as base glass formers may cause novel cathode materials for LIBs. However, the deep information of lithium borate-based glasses doped with Ni-rich  $\text{LiNi}_x\text{Mn}_y\text{Co}_z\text{O}_2$  (NMC) ( $x > y, z$ ) materials has few and unclearly studied.

This study focused on systematic investigations of the physical, local structural, magnetic, and electrochemical properties of the lithium borate-based glass doped with

transition metals (doped with only nickel oxide: single-doping; doped with two transition metals: nickel-cobalt and nickel- manganese: co-doping; doped with nickel, cobalt, and manganese: triple-doping). XRD was employed to characterize the morphological material of the glass samples. Composition analysis was executed by SEM and XPS. Moreover, to deeply understand the structure-function of the lithium borate-based glass doped with transition metal, local structure information, coordination number, and mean value of oxidation states were explored by synchrotron-based XAS technique and XPS. The magnetic properties analyzed by VSM and potentiostatic/galvanostatic with a three-electrode configuration were used to analyze electrochemical properties.



## CHAPTER II

### BACKGROUND

This chapter provides a concise overview of the existing literature, with a particular focus on the themes relevant to the present study. The information of Glass battery, such as history and properties that was explained in the first part of this chapter. Moreover, part of the techniques in this research were descoped in the second part. This chapter concludes with a description background of research.

#### 2.1 HISTORY OF GLASS

Currently, there is an indisputable consensus that electrochemical power sources, such as lithium-ion batteries (LIBs), play a crucial role in ensuring the efficiency and functionality of portable electronic devices, electric cars, and electric utility storage systems. In contrast, the liquid electrolyte solutions now employed in commercial LIBs possess the characteristic of being both flammable and volatile when exposed to elevated temperatures. Therefore, these batteries are considered to present a potential risk of chemical leakage or ignition in the event of physical damage, such as a collision or a short circuit. Moreover, given the existing designs, there is little room for enhancing energy density. The primary limitation of conventional LIBs lies in their inability to meet the increasing requirements for energy density. Enhancing the power of an electric vehicle (EV) while also adhering to crucial constraints such as weight, space, and cost poses a formidable challenge (Xiao et al., 2019). Traditional batteries provide electrical power through chemical reactions that occur between two electrodes. The anode, which is negatively charged, facilitates the outward flow of electrons from the battery. Conversely, the cathode, which is positively charged, allows electrons to enter the battery. The electrodes of a conventional lithium-ion battery consist of materials with inherent structures capable of storing and releasing electrical

charged lithium ions.

Graphite is frequently utilized as the material for the anode, while the cathode is commonly composed of a metal oxide. The electrode materials are applied as coatings onto metal foils, which serve as collectors for the produced current. Copper is frequently utilized as the metallic foil for the anode, whilst aluminum is commonly employed for the cathode. In lithium-ion batteries, the electrodes commonly engage in interactions facilitated by liquid or gel electrolytes. All-solid-state batteries utilize solid electrolytes composed of materials such as ceramics. Solid electrolytes have a higher level of compactness in comparison to their liquid or gel counterparts. This implies that all-solid-state batteries have the capacity to generate a greater amount of energy relative to conventional batteries while occupying an equivalent weight or volume. Furthermore, it is worth noting that all-solid-state lithium batteries exhibit a significantly higher level of safety compared to conventional lithium batteries. The constraints mentioned earlier may be solved by the next generation of lithium batteries that are recognized as solid-state batteries (SSBs).

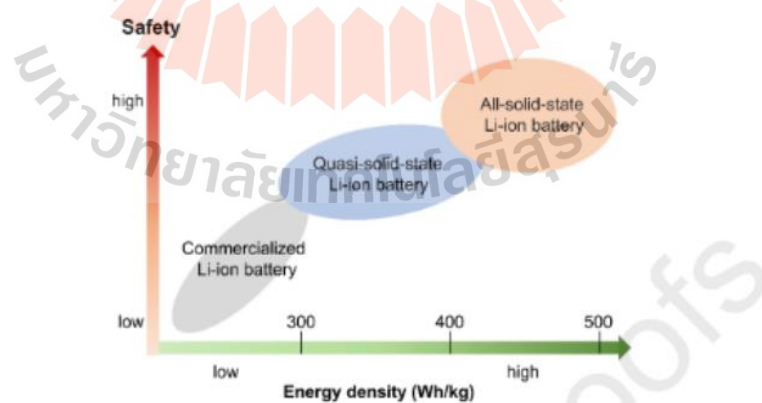


Figure 2.1 Overview of the evolution of battery technology (Wang et al., 2022).

Solid-state batteries are a type of lithium-ion battery that employs solid electrolytes. The growing popularity of SSBs can be attributed to their exceptional safety features and superior energy density, as depicted in Figure 2.1. Solid-state batteries exhibit a better energy density as compared to Li-ion batteries, which rely on a liquid electrolyte solution. Given the absence of any potential risks pertaining to explosions or fires, the inclusion of safety-related components becomes unnecessary, resulting in a surplus of available space. A SSB employs solid electrodes and electrolytes as opposed to a liquid electrolyte solution or polymer gel. Significantly, SSBs have yielded numerous primary advantages, encompassing enhanced safety measures, the elimination of apprehensions regarding toxic organic solvent leakage, decreased flammability risks, non-volatility properties, mechanical and thermal stability, simplified processing procedures, minimal self-discharge rates, heightened achievable power densities, and improved cyclability. Solid-state batteries can often be categorized into various classifications. The glass battery has emerged as a prominent solid-state battery in contemporary discourse. (Fan et al., 2018).

The glass battery is a specific kind of solid-state battery. It makes use of lithium or sodium metal electrodes and a glass electrolyte. The battery was created by John B. Goodenough (Figure 2.2), a 97-year-old materials scientist, solid-state physicist, and professor of mechanical engineering and materials science at the University of Texas at Austin (who is also well-known for creating the lithium-ion battery). Batteries consist of three fundamental constituents, namely an anode, a cathode, and an electrolyte. Most batteries have a liquid separator (electrolyte), but glass batteries are entirely solid, making them less dangerous and posing a lower risk of catching fire. The energy density of these "glass batteries," which utilize a glass powder-based electrolyte, is found to be twice as high as that of traditional lithium-ion batteries. Although it has great and versatile features, this battery technology still faces many challenges to develop and improve its performance. For example, there are not enough suitable solid-state electrolytes (SSEs), and there is also a large interfacial resistance with insufficient interfacial ion/electron transport kinetics. One of the alternatives for improving SSBs' performance is improving cathode materials. This is because the total

achievable capacity of SSBs is determined by the cathode materials (W. Xia et al., 2019).



Figuer 2.2 John B. Goodenough (Ortiz et al., 2022).

## 2.2 Glass on battery electrode

In the realm of rechargeable batteries, crystalline materials have undergone significant advancements as preferred cathode materials for lithium-ion batteries (LIBs) during the past several decades. However, these crystalline cathode materials have various factors that affect the storage capacity, including the available symmetry, phase transitions, crystal growth orientation, and structural stability. Normally, high-capacity crystalline materials are costly materials, so the development of cathode materials is

quite limited. Finding new materials appears to be an interesting solution to this problem. Compared to their crystalline counterparts, amorphous electrode materials may have better electrochemical performance than their crystalline counterparts. Amorphous electrodes possess a structure that exhibits short-range order, a substantial surface area, and available space, enabling lattice distortion to transpire without inducing noticeable macroscopic phase transitions that enhance kinetics. (Wei, Zhixuan et al., 2018). There are several studies that confirm amorphous electrodes have better cyclic performance and higher capacity than crystalline electrodes.

In 2014, Shikun Liu and colleagues conducted a comparative analysis of the characteristics shown by amorphous and crystalline  $V_2O_5$  cathodes in the context of sodium-ion batteries. The  $V_2O_5$  samples experienced a drying process at a temperature of 120 °C for a duration of 10 hours within a vacuum chamber. This resulted in the formation of amorphous  $V_2O_5$  (referred to as a- $V_2O_5$ ) cathodes. Subsequently, the cathodes were subjected to annealing at a temperature of 350 °C for a duration of 4 hours in an air environment, leading to the formation of crystalline  $V_2O_5$  (referred to as c- $V_2O_5$ ) cathodes. The larger reversible capacities of the a- $V_2O_5$  cathode (217.1 and 186.9 mA h/g at 80 and 160 mA/g, respectively) compared to the c- $V_2O_5$  cathode (186.6 and 158.3 mAh/g) at low current densities are clearly evident in Figure 2.3. In contrast, the cathode composed of c- $V_2O_5$  exhibits superior specific capacities compared to the cathode composed of a- $V_2O_5$  under conditions of high current densities. The electrochemical findings presented in this study demonstrate that amorphous materials possess notable characteristics that make them a compelling choice for utilization as cathode materials, particularly under conditions of low current densities (Shikun et al., 2016).

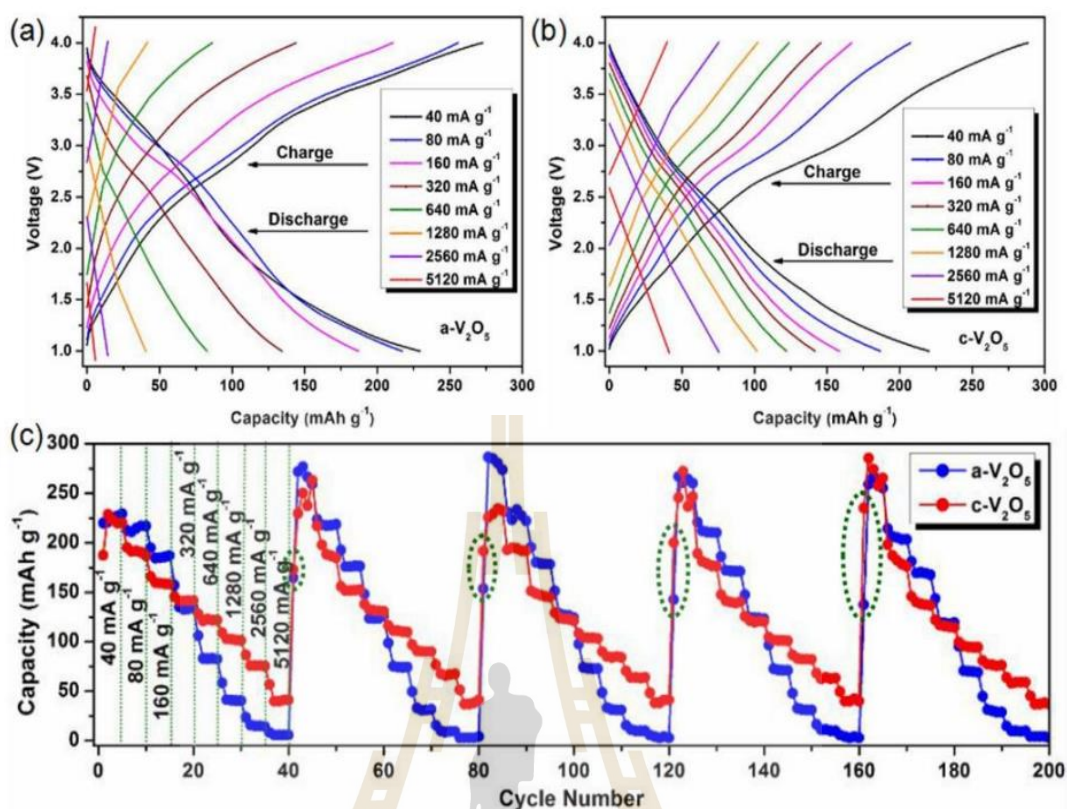


**Figure 2.3** Charge and discharge curves for a cathode made of (a)  $\text{V}_2\text{O}_5$  (b)  $c\text{-V}_2\text{O}_5$  cathode with current densities ranging from 1.0 to 4.0 V, and (c) a comparison of the two cathodes rate performance. (Shikun et al., 2016).

Moreover, in 2018, Heng Wang and his group reported on the properties of amorphous and crystalline cathode materials for lithium ion batteries. Comparison of amorphous and crystalline MetfV10 cathode electrochemical performance is shown in Figure 2.4. According to their respective galvanostatic discharge and charge curves, the amorphous and crystalline MetfV10 cathodes have first-discharge capacities of 156 and 122  $\text{mAh/g}$ . Moreover, Figure 2.4b shows the cycle dependence of the discharge capacities for the two cathodes. It can be clearly seen that the amorphous cathode maintains a capacity greater than the crystalline cathode (approximately 100  $\text{mAh/g}$  after 20 cycles). The disordered structure of the amorphous cathode may help Li ions more easily intercalate into the materials, resulting in a decrease in resistance. These

results show that amorphous materials are one good candidate to replace or develop cathode materials (W., Heng et al., 2018).

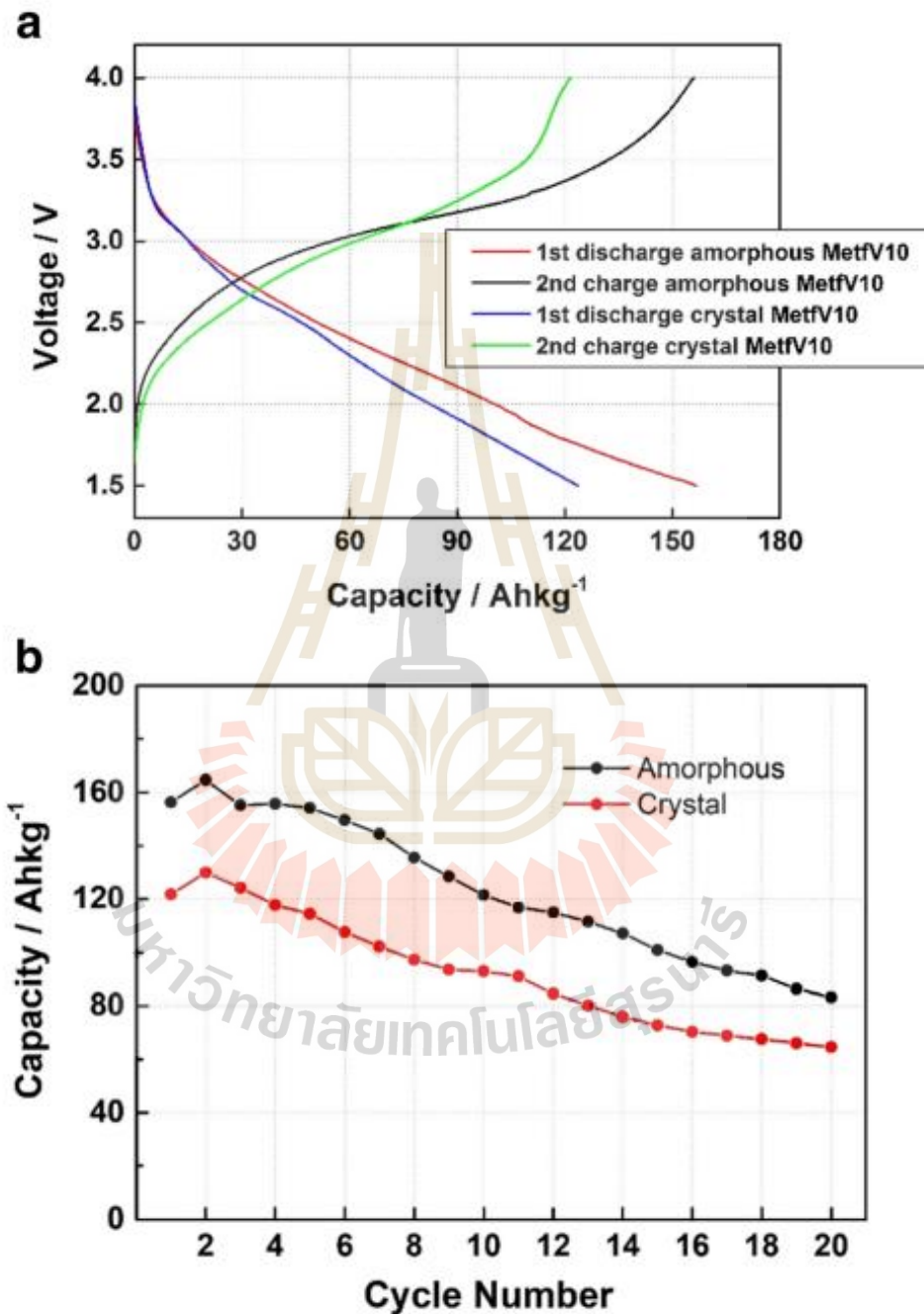


Figure 2.4 LIBs with amorphous and crystal MetfV10 cathodes: a) first discharge and second charge curves; and b) cycle performance (Heng et al., 2018).

### 2.2.1 B<sub>2</sub>O<sub>3</sub> glass electrode

The utilization of glasses including transition metal ions as cathode materials in batteries holds substantial promise for amorphous electrodes. The oxidation-reduction equilibrium and the valence states of metal ions have a significant impact on the structure and properties of materials, including their crystallization behavior and electrical conductivity. These factors contribute to the formation of shapes that are easily achieved. In general, oxide glass materials are based on P<sub>2</sub>O<sub>5</sub>, B<sub>2</sub>O<sub>3</sub>, and SiO<sub>2</sub> glass formers (Lai et al., 2019). One of the lithium ionic conductors that has already undergone research and demonstrated excellent ionic conductivity is lithium boron oxide (Li<sub>2</sub>O-2B<sub>2</sub>O<sub>3</sub>, or LBO) glass. In borates, the BO<sub>3</sub> triangle planar and the BO<sub>4</sub> tetrahedron serve as the basic structural units. These two units can be combined to form different polysorbate B<sub>x</sub>O<sub>y</sub> ions by sharing an O corner, edge, or plane. In addition to the fundamental BO<sub>3</sub> and BO<sub>4</sub> units, other well-known ones include [BO<sub>2</sub>]<sub>1</sub>, B<sub>2</sub>O<sub>4</sub>, B<sub>2</sub>O<sub>5</sub>, B<sub>3</sub>O<sub>6</sub>, B<sub>3</sub>O<sub>7</sub>, and B<sub>4</sub>O<sub>10</sub> units, among others. Theoretically, an electrode material's molecular weight has an inverse correlation with its theoretical capacity, according to Faraday's law. The molecular weights of borates are typically significantly smaller compared to those of phosphates, silicates, and sulfates for all recognized inorganic salt-type electrode materials because the element boron is much lighter than P, Si, and S. Because of this, borates have much higher capacities than the other materials, and they could be used in the future to make cathodes for rechargeable batteries with a high energy density. When compared to the other groups that are responsible for glass formation, borate has a higher theoretical prowess (200 mAh/g). Borate has higher specific capacities (170 mAh/g) when compared to LiFePO<sub>4</sub> phosphate, which is the material that is used the most frequently and has the most success. On the other hand, it is undeniably harder to make borate because the reactants are not very stable. Additionally, different types of borate ions can be created by using a straightforward BO<sub>3</sub> planar triangle and a BO<sub>4</sub> tetrahedron, which can make the preparation of pure phases challenging. Borates, despite having high theoretical specific capacities, have low specific capacities when compared to other types of cathode materials, indicating that borates are not widely used in cathode materials. Because of this, lithium-borate glasses are frequently combined with other elements in order to boost the

electrochemical properties of the glasses. Transition metals are considered to be very intriguing contenders when it comes to the inclusion of elements in lithium-borate glasses. This is mostly due to their ability to showcase a diverse array of components and structures, which in turn elucidates a broad spectrum of electrochemical capabilities. As a result of these advancements, numerous innovative electrodes have been identified for the purpose of enhancing the performance of lithium-ion batteries.

### 2.2.2 Effect of transition metal doping

Recently, lithium-borate glass materials have received much attention as an energy storage resource (Afyon et al., 2014). Metal oxides possessing crystalline structural shapes are capable of exhibiting high capacities when utilized as electrode materials. Nevertheless, the utilization of crystalline electrode materials is not without its challenges, including concerns related to electrode swelling and the infiltration of ions into the crystalline lattice. Due to these rationales, researchers endeavor to substitute crystalline electrode materials with amorphous glass structures. The flexibility of the glass structure is influenced by the variations in bonding angles that connect network-forming polyhedral. For instance, the Si-O-Si bond angle, which can range from  $125^\circ$  to  $165^\circ$ , and the P-O-P bond angle in phosphate glass, which can range from  $123^\circ$  to  $180^\circ$ , play a significant role in determining the overall flexibility of the glass structure. The bond angle within the boroxol ring of the borate structure might undergo significant alterations in the case of borate glass. It has been shown that these materials possess a notably elevated capacity for glass formation (Stoch et al., 1999). There are few applications for glassy borates as electrodes, in contrast to borate-type electrolytes. However, a number of research studies have shown that the performance of the electrode can be improved by doping the borate glass with transition metal. For instance: Dong and all others reported on the electrochemical performance of  $\text{Li}_2\text{O}-\text{B}_2\text{O}_3$  with Fe in 2008. The preliminary results show that  $\text{LiFeBO}_3$  exhibits good electrochemical properties. Electrochemical tests show that  $\text{LiFeBO}_3$  exhibits better electrochemical properties. Figure 2.5a shows the typical charge and discharge curves of an initial discharge capacity of 125.8 mAh/g that can be obtained at a discharge current density of 5 mA/g. The specific capacity can still be held even as the discharge

current density increases. Moreover, the good coulombic efficiency (close to 100%) in Figure 2.5. suggests that the  $\text{LiBO}_3$  dope with Fe can be used as a reversible insertion material (Dong et al., 2008).

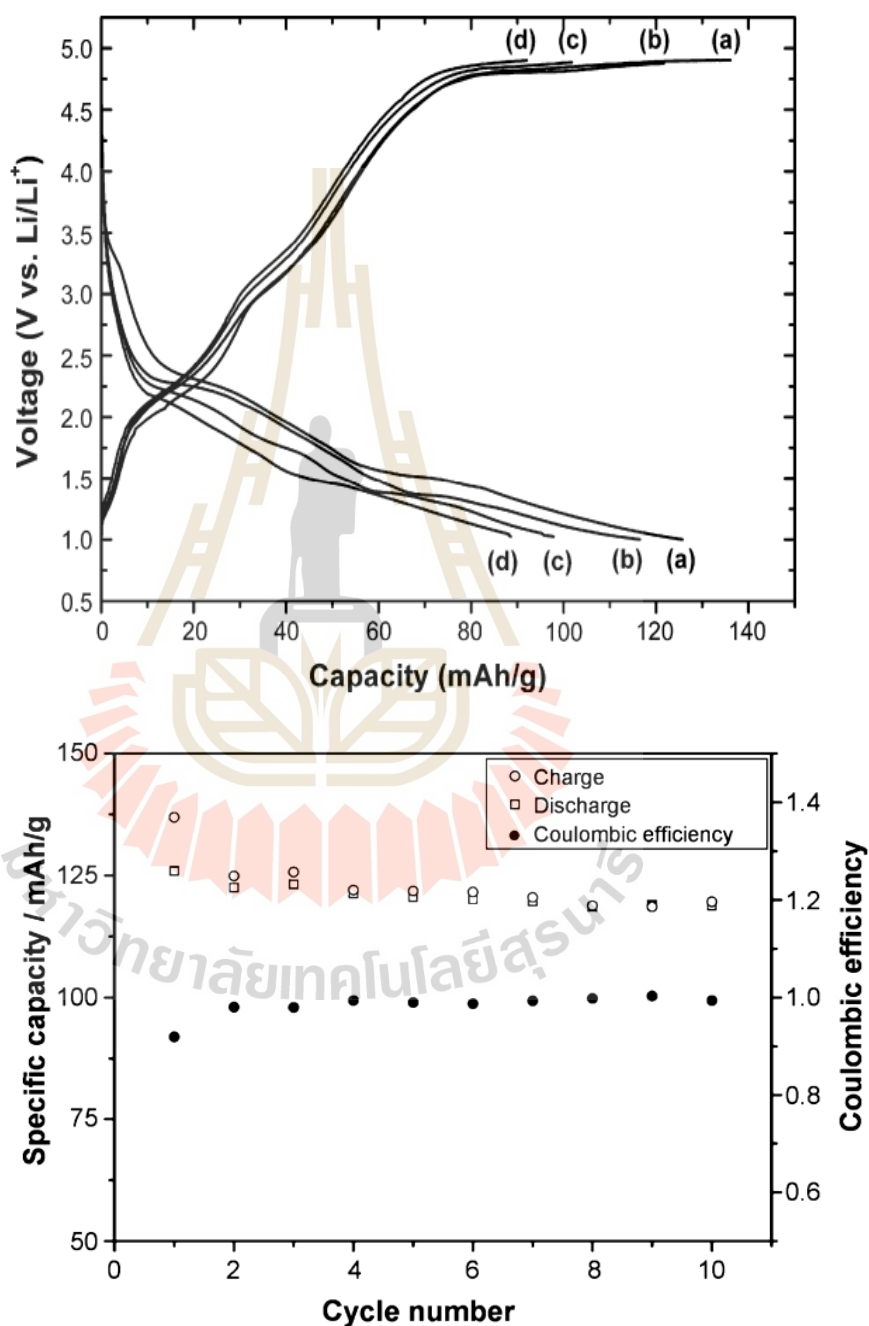


**Figure 2.5** a) The standard charge-discharge trends of a  $\text{LiFeBO}_3$  cell at current levels of 5 mA/g, 10 mA/g, 20 mA/g, and 50 mA/g and b) at 5 mA/g current density. (Dong et al., 2008).

Moreover, A study conducted by Semih Afyon and colleagues in 2014 examined the composite electrodes consisting of  $V_2O_5$ - $LiBO_2$  glass combined with reduced graphite oxide (RGO). The glass composition consisting of  $V_2O_5$ - $LiBO_2$  with reduced graphene oxide (RGO), as seen in Figure 2.6, exhibited notable specific capacities, reaching values as high as 300 mAh/g during the initial 100 cycles. These cycles were conducted within the voltage range of 1.5 V to 4.0 V at a rate of 50 mA/g. At an enhanced rate of 400 mA/g, the composite electrode exhibits a noteworthy discharge capacity of 299 mAh/g during the 35th cycle. In comparison to vanadate-borate glasses, the undoped reduced graphene oxide (RGO) has certain characteristics. The  $V_2O_5$ - $LiBO_2$  glass with RGO exhibits enhanced charge and discharge capacities and improved cycling stability. The findings of vanadate-borate glasses indicate that the incorporation of transition metals into lithium-borate glass can enhance the specific capacities and cycling stability of the glass cathode material (Semih et al., 2014).

Subsequently, Semih proceeded to provide further details regarding the cathode composite material,  $nanoh-LiMnBO_3$ , employing the ultrasonic nebulized spray pyrolysis process. The carbon/Nano  $LiMnBO_3$  composite exhibited a rather consistent cycling performance, with an average decrease in discharge capacity of 0.9% per cycle over the initial 50 cycles. Furthermore, when operated at a C/15 rate throughout the voltage range of 4.5–2.0 V, it achieved a discharge capacity of approximately 140 mAh/g. The inclusion of metal doping, which enhances the structural integrity during charged states, along with the implementation of advanced protective coatings, which limit reactions between the electrolyte and the delithiated phases, are likely the key factors enabling the achievement of higher charge and discharge capacities while preserving a greater degree of cycling stability (Semih et al., 2014).

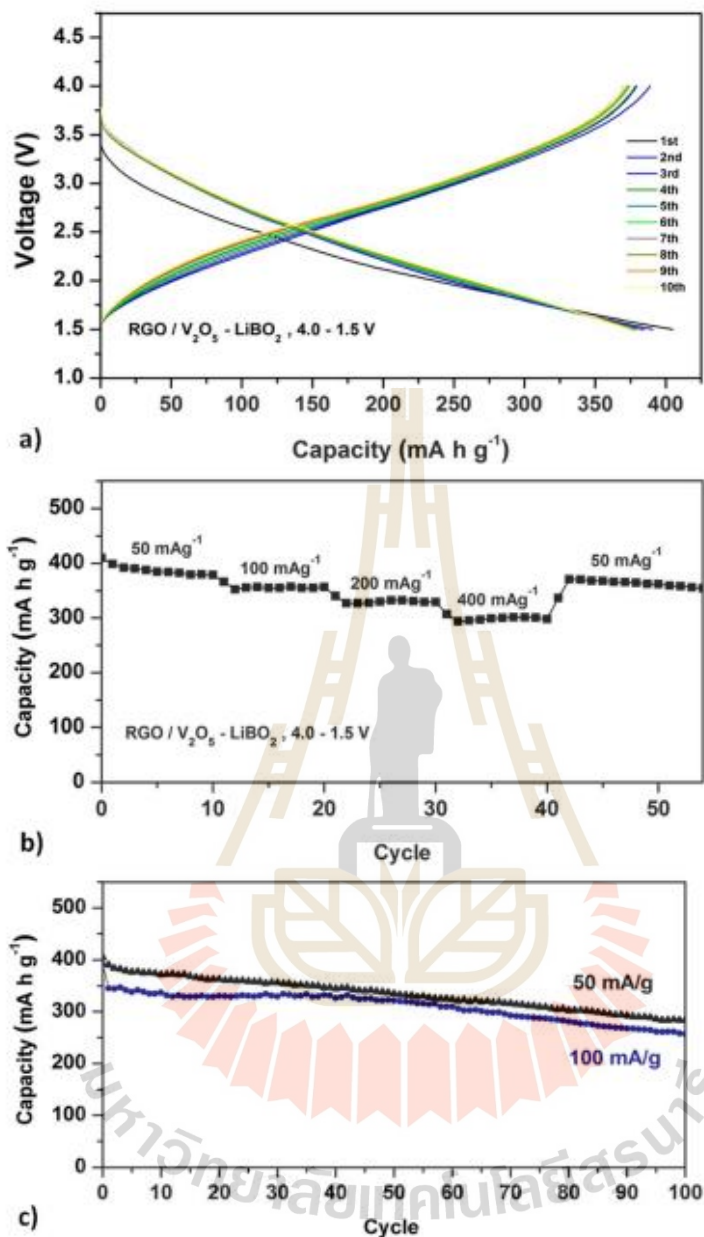


**Figure 2.6** (a) The initial ten charge/discharge profiles of the RGO/V<sub>2</sub>O<sub>5</sub>-LiBO<sub>2</sub> glass composite were obtained within a potential range of 1.5–4.0 V using a current density of 50 mA/g, (b) the rate capacity of the RGO/V<sub>2</sub>O<sub>5</sub> - LiBO<sub>2</sub> glass composite at room temperature ranges from 1.5 V to 4.0 V for 50, 100, 200, and 400 mA/g, (c) Discharge capacity against number of cycles for an RGO/V<sub>2</sub>O<sub>5</sub>-LiBO<sub>2</sub> glass composite discharging at 50 and 100 mA/g.

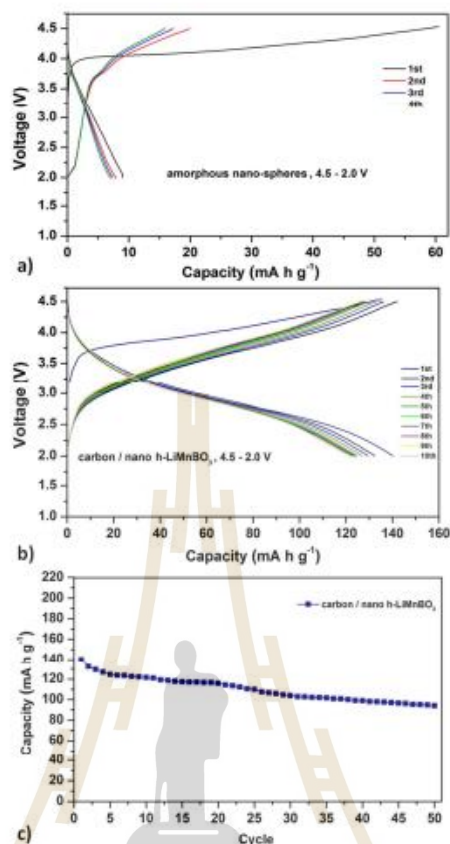


**Figure 2.7** a) Four initial charge-discharge curves for amorphous nano-spheres in the 4.5–2.0 V, C/20 potential range; b) the initial ten C/D curves of the carbon/Nano h-LiMnBO<sub>3</sub> composite operating in the 4.5 V to 2.0 V, C/15 potential range; and c) the discharge capacity of the carbon/Nano h-LiMnBO<sub>3</sub> composite as a function of the number of cycles at a C/15 rate and a voltage range of 4.5–2.0 V. (Semih et al., 2014).

A study by Il'ina and others looked into the electrochemical performance of a glassy mixture made up of 30Li<sub>2</sub>O-47.5V<sub>2</sub>O<sub>5</sub>-22.5B<sub>2</sub>O<sub>3</sub> (called LBV) that had been crystallized on a Li<sub>7</sub>La<sub>3</sub>Zr<sub>2</sub>O<sub>12</sub> (LLZ) base. The duration of the holding periods varied between 0.5 and 5 minutes, while the temperatures spanned from 650 to 850 degrees Celsius. The formation of vanadate in conjunction with lithium can occur throughout a wide range of temperatures, but the formation of vanadate in conjunction with boron is limited to temperatures exceeding 750°C. The scanning electron microscopy (SEM) image reveals that the LBV glass generated at a temperature of 750 degrees Celsius

exhibits an ideal interface and intimate contact between the electrode and electrolyte. The combination of LBV and LLZ under consideration demonstrates superior performance in terms of polarization resistance and interface conductivity. There is a prevailing belief among individuals that the integration of LBV glass with alternative solid-state electrolytes has the potential to yield a highly functional and dependable interface for lithium-ion batteries (LIBs). (Ilina et al., 2018).

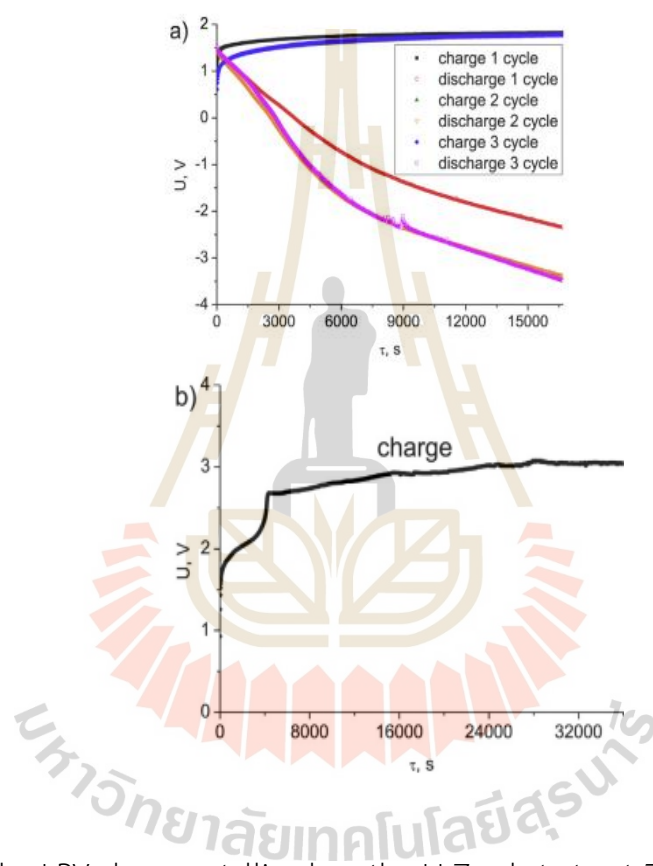


**Figure 2.8** The LBV glass crystallized on the LLZ substrate at 750 C for 0.5 min, and the charge-discharge curves of the LBV<sub>j</sub>LLZ<sub>j</sub>GaAg cell. Under 1 (a) or 50 (b) mA, (2.6 and 130 mA cm<sup>2</sup>, respectively), the active electrode (I) was determined to be composed of LBV glass (Ilina et al., 2018).

2019 is the year that En-Lai Zhao and the research group investigate the electrochemical performance of glass made of Li<sub>2</sub>O-V<sub>2</sub>O<sub>5</sub>-SiO<sub>2</sub>-B<sub>2</sub>O<sub>3</sub> as a cathode material for lithium ion batteries. Using a simple melt-quenching technique, a series of 20Li<sub>2</sub>O-30V<sub>2</sub>O<sub>5</sub>-(50-x)SiO<sub>2</sub>-xB<sub>2</sub>O<sub>3</sub> (mol%) (x = 10, 20, 30, and 40) glasses were produced.

The amorphous nature of as-quenched glass powders and the even distribution of V, Si, B, and O elements were revealed by XRD, DSC, FTIR, TEM, and EDS analyses. In terms of electronic conductivity, the glass with the highest V4 fraction was the 20Li<sub>2</sub>O-30V<sub>2</sub>O<sub>5</sub>-40SiO<sub>2</sub>, and 10B<sub>2</sub>O<sub>3</sub> (LVSB<sub>10</sub>) sample. Although the LVSB<sub>10</sub> sample had a significantly higher initial discharge capacity and cycling capacity than the rest of the samples, its capacity quickly degraded. Because of this, the LVSB<sub>10</sub> sample was destroyed by ball milling in order to reduce the particle size. It was discovered that the particle size could be decreased without altering the amorphous nature of the particles. Finally, quaternary glass materials like Li<sub>2</sub>O-V<sub>2</sub>O<sub>5</sub>-SiO<sub>2</sub>-B<sub>2</sub>O<sub>3</sub> show promise as future cathode materials (Zhao et al., 2019).

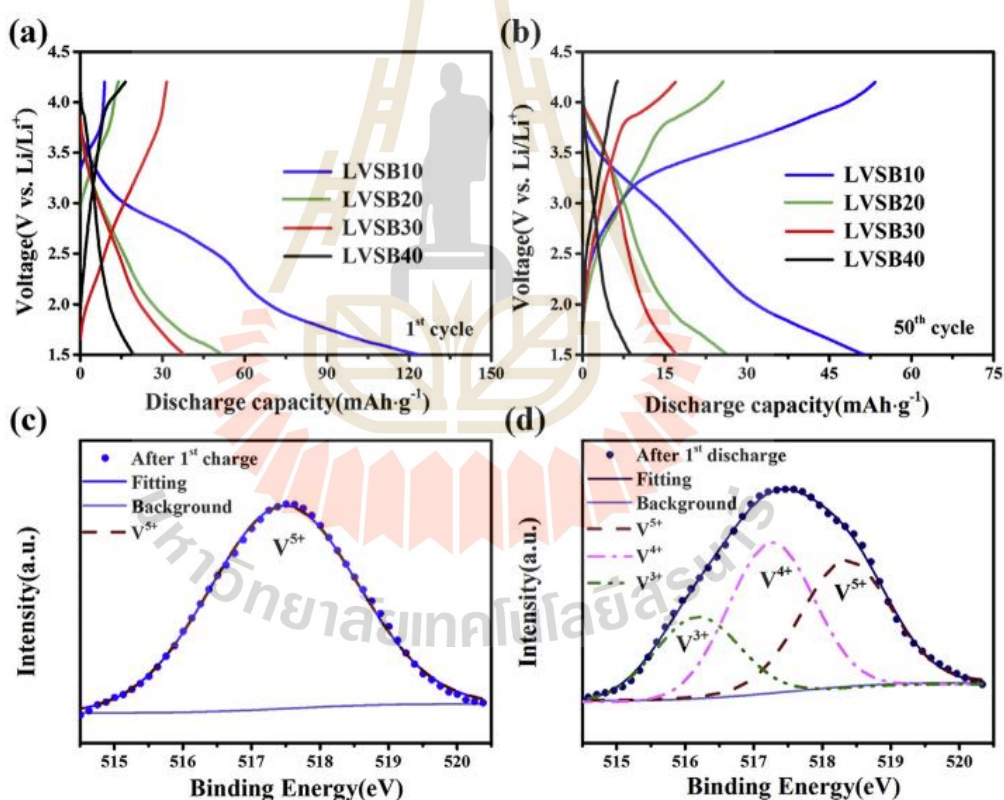


**Figure 2.9** Ex-situ V 2p<sub>2</sub>/XPS spectra of the LVSB<sub>10</sub> electrode at (c) 4.2 V and (d) 1.5 V for the first cycle, and charge/discharge curves of the LVSB<sub>10</sub>, LVSB<sub>20</sub>, LVSB<sub>30</sub>, and LVSB<sub>40</sub> glass samples after (a) 1st cycle and (b) 50th cycle. (Zhao et al., 2019).

The mesh-like  $\text{LiZnBO}_3/\text{C}$  composite was investigated as an anode material for lithium-ion batteries by Li et al (Li et al., 2016). The initial capacity of the material is 860 mAh/g, and it exhibits a capacity retention of 559 mAh/g after undergoing 600 cycles at a current density of 500 mA/g, as shown in Figure 2.10. The ex-situ XRD technique is employed to confirm the presence of a mixed intercalation-conversion-alloy lithium storage process during the initial cycle. The complete cell, consisting of  $\text{LiZnBO}_3/\text{C}$  and  $\text{LiCO}_2$ , exhibits a capacity of 658 mAh/g when subjected to a current density of 100 mA/g. Furthermore, it retains a capacity of 603 mAh/g even after undergoing 400 cycles. After undergoing 600 cycles, the capacity of the material can still persist at 559 mAh/g, which corresponds to a capacity retention of 94.74% relative to the capacity seen in the second cycle. Typically, electrode activation takes place during the early cycle phase. The notable enhancement in capacity observed after 250 cycles in Figure 2.10c can be due to a combination of surface- and diffusion-controlled electrode kinetics, potentially resulting from the development of gel-like polymer films during cycling.

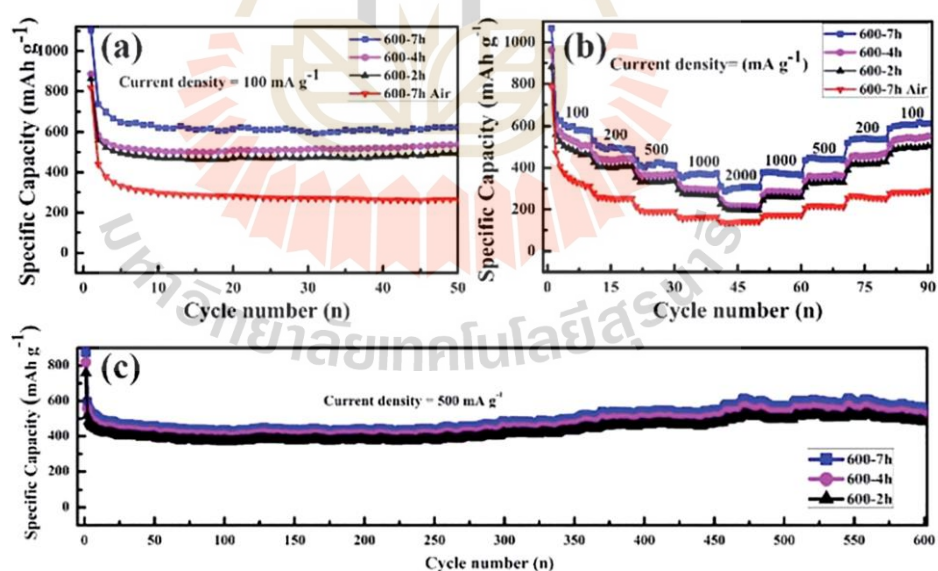


**Figure 2.10** Illustrates the electrochemical capabilities of  $\text{LiZnBO}_3/\text{C}$ . (a) The performance of the cycle at a current density of 100 mA/g (b) The performances at different current densities (c) The long-term cycle performance at a current density of

500 mA/g In the year 2016, the Royal Society of Chemistry published a document (Li et al., 2016).

In their 2018 publication, Cheng et al. discuss the crystallization of  $\text{Li}_{0.9}\text{V}_{2.07}\text{BO}_5$  (LVBO) in the orthorhombic space group  $\text{Pb}_{am}$ , where both Li and V atoms occupy the same sites. The LVBO nanorods/C composite demonstrates favorable electrochemical activity. The cathode used in LIBs exhibits a first discharge capacity of 125 mAh/g at a rate of 0.2 C, within the voltage range of 1.5 to 4.2 V. This capacity is significantly more than that observed in the majority of published  $\text{LiMBO}_3$  materials. At a temperature of 2 degrees Celsius, the initial capacity of the first sample is around 88 milliampere-hours per gram (mAh/g), and after 100 cycles, the remaining capacity is 56 mAh/g, as shown in Figure 2.11 (Cheng et al., 2018). The CV curve exhibits a lack of distinct oxidation and reduction peaks, aligning closely with the galvanostatic voltage profile. The rapid deterioration in capacity is attributed to the structural modification of lithium vanadium boron phosphate (LVBO) throughout the cycle process. The LVBO sample has a much greater electronic conductivity of  $1.05 \times 10^{-5}$  S/cm compared to lithium phosphate. From a comprehensive standpoint, the electrochemical performance of LVBO exhibits a lack of promising results. However, if the structure of the system undergoes appropriate restrictions, its cyclic stability can be significantly strengthened. It is widely recognized that electrode materials incorporating the element V typically demonstrate favorable rate capabilities (Liu et al., 2017).

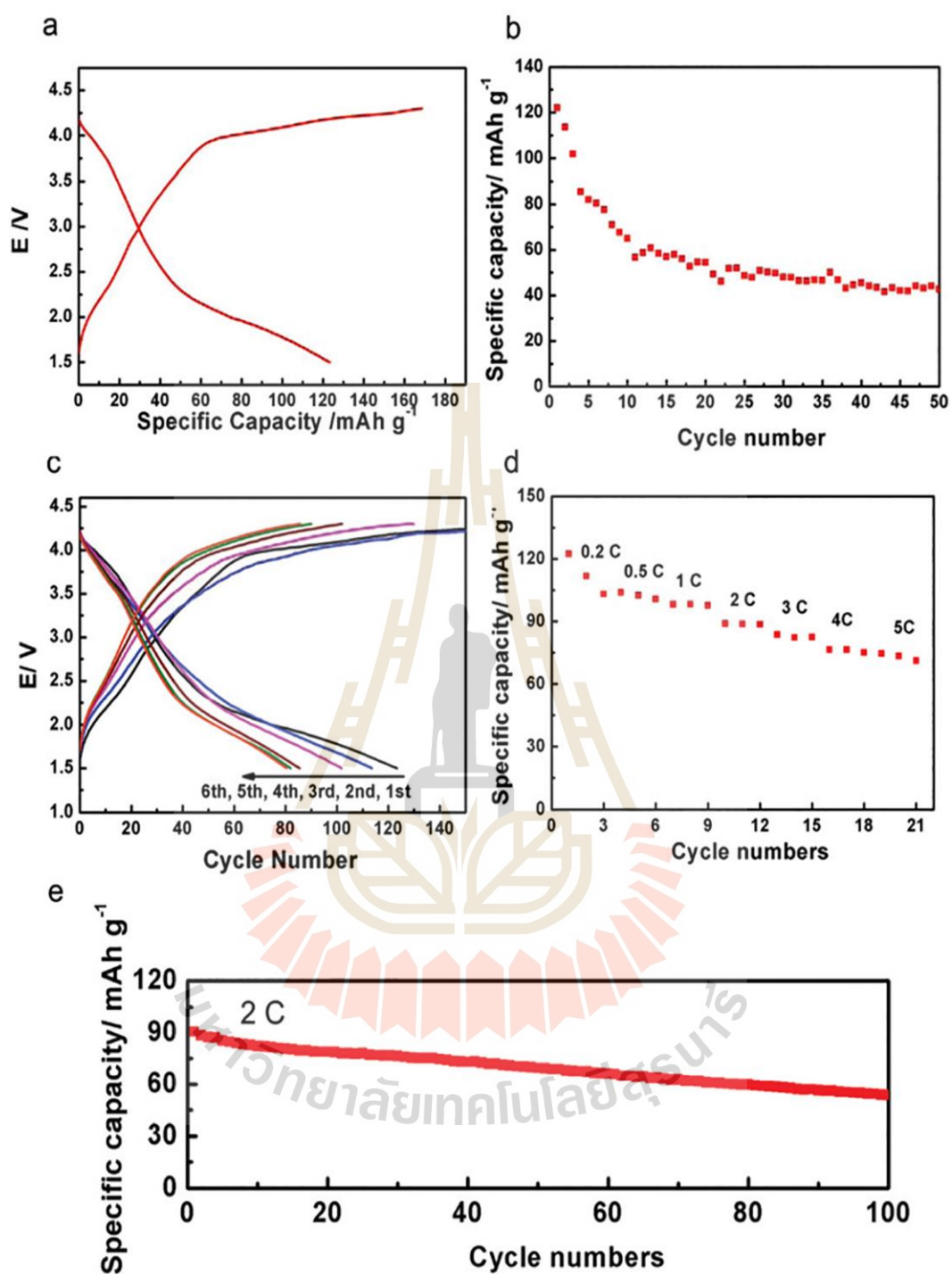


Figure 2.11 a) Initial galvanostatic voltage profiles of the sample at 0.2 C and voltages between 1.5 and 4.2 volts, b) The performance of LVBO at a cycling rate of 0.2 C, and c) The galvanostatic voltage profiles of LVBO over the initial six cycles are presented (Cheng et al., 2018).

Furthermore, Butnoi and colleagues used a melt-quenching technique to study and synthesize the 0.3 MnO<sub>2</sub> and 0.7 Li<sub>x</sub>BO<sub>2</sub> glasses system. The VSM technique was utilized in order to investigate the magnetic characteristics of the glass sample. Initial specific capacitance values of 23, 27, 30, and 52 F/g are displayed by the composite cathode, displaying excellent specific capacitance. These findings suggest that the best magnetic and electrochemical properties occur when Mn<sup>2+</sup> and Mn<sup>3+</sup> ions coexist with the optimal Li content. They believe that these observations will contribute to the development of a glass electrode that can be used in the future for lithium battery applications (Butnoi et al., 2019). In addition to the aforementioned works, there exist several further studies conducted on LiMBO<sub>3</sub> compounds, where M represents Fe, Mn, Co, or Zn. The corresponding electrochemical data for these studies may be found in Table 2.1.

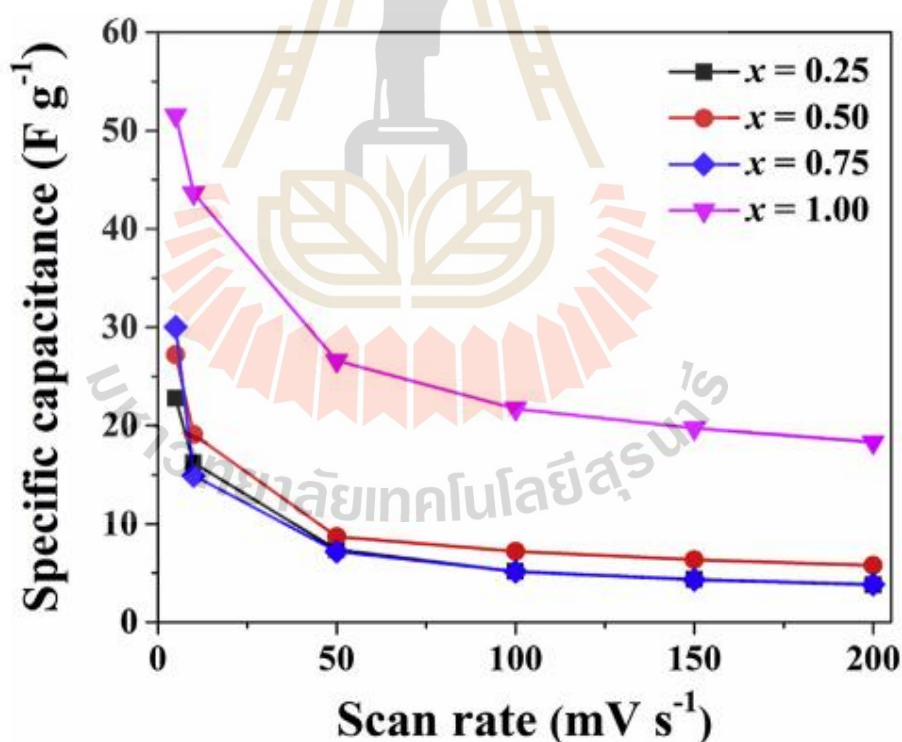


Figure 2.12 Scatter plots of measured capacitance versus sampling frequencies of 0.3MnO<sub>2</sub>-0.7(Li<sub>x</sub>BO<sub>2</sub>) glasses (Butnoi et al., 2019).

**Table 2.1** The electrochemical data of  $\text{LiMBO}_3$  (M = Fe, Mn, Co, Zn).

Material and morphology	Synthetic method	Electrochemical data	Reference
h- $\text{LiMnBO}_3/\text{C}$ microparticles	In-situ carbothermal solid state synthesis	86.5% of the 1st discharge capacity (90.7 mAh/g) after 40 cycles at 0.05 C	Li et al., 2013
m- $\text{LiMnBO}_3/\text{C}$ lumps	In-situ carbothermal solid state synthesis	80.8% of the initial discharge capacity (107 mAh/g) after 40 cycles at 0.05 C	Chi et al., 2016
h- $\text{LiMnBO}_3$ nanospheres	Ultrasonic nebulized spray pyrolysis	The 1st discharge capacity of 140 mAh/g at C/15, and 110 mAh/g at the 25th cycle	Afyon et al., 2014
RGO/h- $\text{LiMnBO}_3$ nanorods	Sol-gel method	110 mAh/g after 10 cycles at C/20 rate	Afyon et al., 2013
C- $\text{LiFeBO}_3$ particles	Solid-state reaction	158.3 mAh/g at 5 mA/g and 122.9 mAh/g at 50 mA/g	Dong et al., 2008
$\text{LiFeBO}_3$ agglomerates	Solution combustion synthesis	175 mAh/g after 5 cycles at C/20 (298 K) 170 mAh/g after 30 cycles	Barpanda et al., 2013

**Table 2.1** (Continued) The electrochemical data of  $\text{LiMBO}_3$  (M = Fe, Mn, Co, Zn).

Material and morphology	Synthetic method	Electrochemical data	Reference
Mesoporous $\text{LiFeBO}_3/\text{C}$ hollow spheres	Soft template method	77% of initial capacity (190 mAh/g) after 100 cycles at 0.05 C	Dong et al., 2013
$\text{Li}(\text{Mn}_{1-x}\text{Co}_x)\text{BO}_3$	Solid-state synthesis	Initial capacity of 48~54 mAh/g at C/20	Chi et al., 2020
Mesh-like $\text{LiZnBO}_3/\text{C}$	Facile polymer pyrolysis method	559 mAh/g after 600 cycles with a capacity retention of 94.47% of the 1st capacity (860 mAh/g) at 500 mA/g (anode)	Shi et al., 2020
$\text{LiMn}_{0.5}\text{Fe}_{0.4}\text{Mg}_{0.1}\text{BO}_3$	Nanocasting technique	201 mAh/g at C/50, and 120 mAh/g at 1 C	Fang et al., 2018
Monoclinic $\text{Li}(\text{Mn}_x\text{Fe}_{1-x})\text{BO}_3/\text{C}$ ( $0 \leq x \leq 1$ )	Solid-state synthesis	1st capacity: ~160 mAh/g ( $x = 0$ ), ~140 mAh/g ( $x = 0.3$ )	Yamada et al., 2011
Multi-layer core-shell structural $\text{LiFeBO}_3/\text{C}$	Spray-drying and Carbothermal method	Initial discharge capacity of 196.5 mAh/g, and ~136.1 mAh/g after 30 cycles at 10 mA/g	Zhang et al., 2014

## 2.3 Glass production

At present, there are various methods available for the synthesis of glasses, including melt-quenching, sol-gel, chemical vapor deposition, sputtering, glow-discharge, and several more. The melt quenching process is extensively employed due to its simplicity, ease of implementation, and applicability for the production of many glass types on a small-scale (laboratory) level. In light of the aforementioned context, the subsequent discourse will provide an elucidation of the aforementioned methodologies.

### 2.3.1 Melt-Quenching Technique

Melt-quenching is used to create almost all glasses today. The raw material mixture, or batch, is heated to between 1100 and 1600 degrees Celsius and melted for a set amount of time. The elimination of residual thermal stresses in cast glass is achieved through the process of annealing, wherein the glass melt is heated to a temperature close to the glass transition temperature specific to the kind of glass. The glasses acquired through this particular method are commonly referred to as "as-prepared glasses." The preparation of as-prepared glass samples required for various characterization procedures involves the utilization of sawing, grinding, and polishing techniques. Figure 2.13 is a simplified diagram of the melt-quenching method used to prepare glass. Chemical calculations, weighing, and mixing are the next steps after selecting the right raw materials. The use of a platinum or silica glass rod for occasional stirring helps keep the glass melt homogeneous. Glass melting crucibles can be fabricated from a variety of materials, including fused silica ( $\text{SiO}_2$ ), alumina ( $\text{Al}_2\text{O}_3$ ), pure platinum (Pt), oxide dispersed strengthened (ODS) platinum, platinum-gold (Pt-5% Au), platinum-rhodium (Pt-10% Rh), or platinum-iridium (Pt-10% Ir). To avoid contamination, however, the use of pure platinum (Pt) or ODS platinum crucibles is recommended. Appropriate caps can be used to slow the rate of loss due to evaporation. On the other hand, a hermetically sealed silica ampoule, obtained via fusing with the aid of an appropriate oxyhydrogen flame, is recommended for melting chalcogenide glasses (Karmakar et al., 2016).

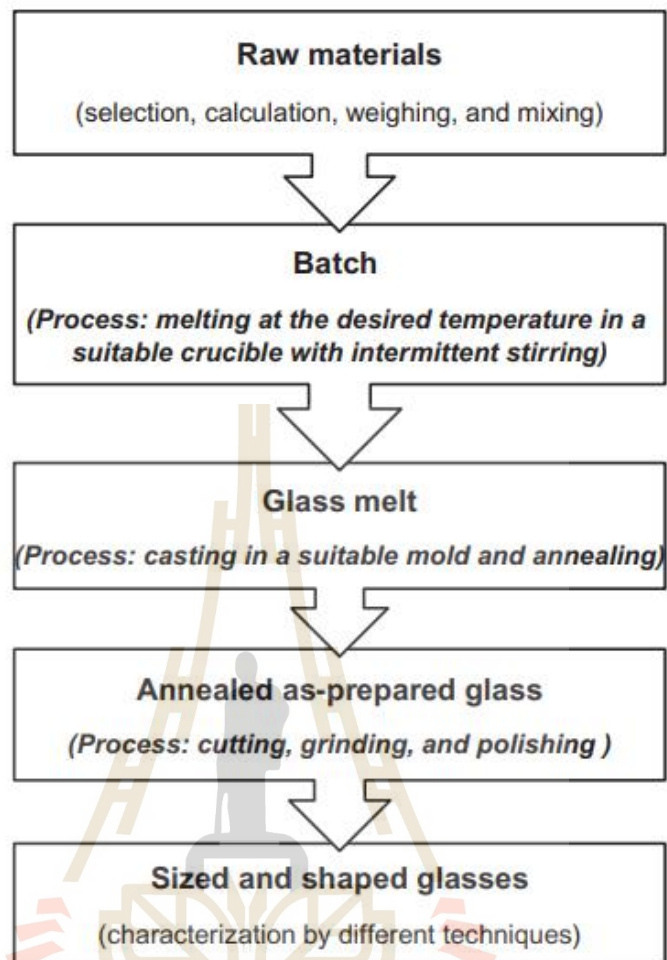


**Figure 2.13** A schematic depiction of the various stages involved in the melt quenching method of glassmaking. (Karmakar et al., 2016).

Melt-Quenching Technique has been studied extensively for the production of lithium borate glass. As a result, this section provides only a sampling of research that has proven fruitful. Initially,  $\text{Li}_2\text{O}$ ,  $\text{H}_3\text{BO}_3$ , and  $\text{CuO}$  of reagent grade were purchased from Aldrich and used to create a glass with the composition  $x\text{Li}_2\text{O}-\text{B}_2\text{O}_3-y\text{CuO}$ , where  $x = 0.1$  and  $y = 0.005-0.05$  ( $x = \text{Li}_2\text{O mol\%/B}_2\text{O}_3 \text{ mol\%}$ ). The constituents of the batch were meticulously amalgamated prior to undergoing the process of liquefaction within a crucible composed of platinum, which was sustained at a temperature range of 1000–1050 degrees Celsius for a duration of one hour. The utilization of brass plates for the purpose of quenching the molten substance led to the production of a glass

with a distinct light blue hue. Rigaku X-ray diffraction spectroscopy at room temperature using copper-K radiation of 1.54 revealed no crystalline peaks in the samples (ss with the composition  $x\text{Li}_2\text{O}-\text{B}_2\text{O}_3-y\text{CuO}$ , where  $x = 0.1$  and  $y = 0.005-0.05$  ( $x = \text{Li}_2\text{O mol\%/B}_2\text{O}_3 \text{ mol\%}$ ). The ingredients for the batch were thoroughly combined before being melted in a platinum crucible for an hour at 1000–1050 degrees Celsius. Brass plates were used to quench the melt, resulting in a light blue glass. Rigaku X-ray diffraction spectroscopy at room temperature using copper-K radiation of 1.54 revealed no crystalline peaks in the samples (Figure 2.14) (Noh et al., 2017).

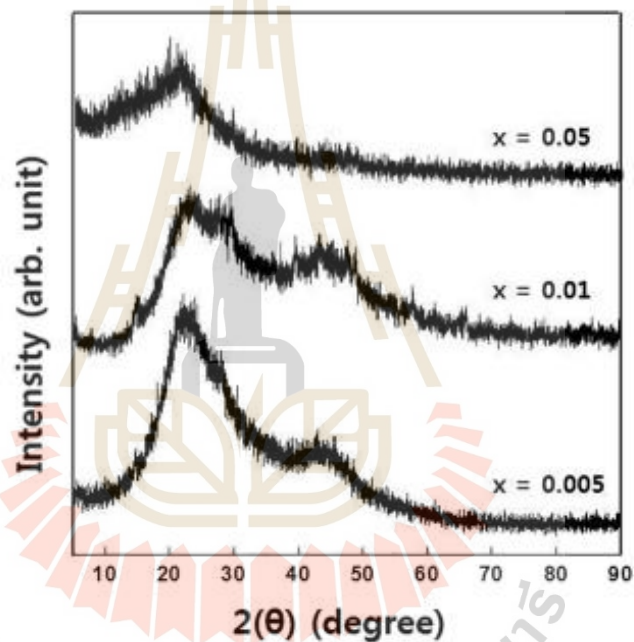


**Figure 2.14** X-ray diffraction spectroscopy of  $x\text{Li}_2\text{O}-\text{B}_2\text{O}_3-y\text{CuO}$ , where  $x = 0.1$  and  $y = 0.005-0.05$  (Noh et al., 2017).

## 2.4 Characterization techniques

### 2.4.1 Synchrotron radiation

#### 2.4.1.1 Synchrotron

An electron or ion can be accelerated to nearly light speed in a device called a synchrotron, which is a large machine. In the process of being redirected by magnetic fields, these electrons or ions emit a form of extremely powerful electromagnetic

radiation known as synchrotron radiation or synchrotron light. In Figure 2.15, we can see the synchrotron's main components. First, electrons from the electron gun (1) are sent to the linear accelerator (linac) to be accelerated (2). When electrons are accelerated using radio waves, powerful electric and magnetic fields are produced. Once an electron enters the linac, its strong electrical potential is quickly reversed.

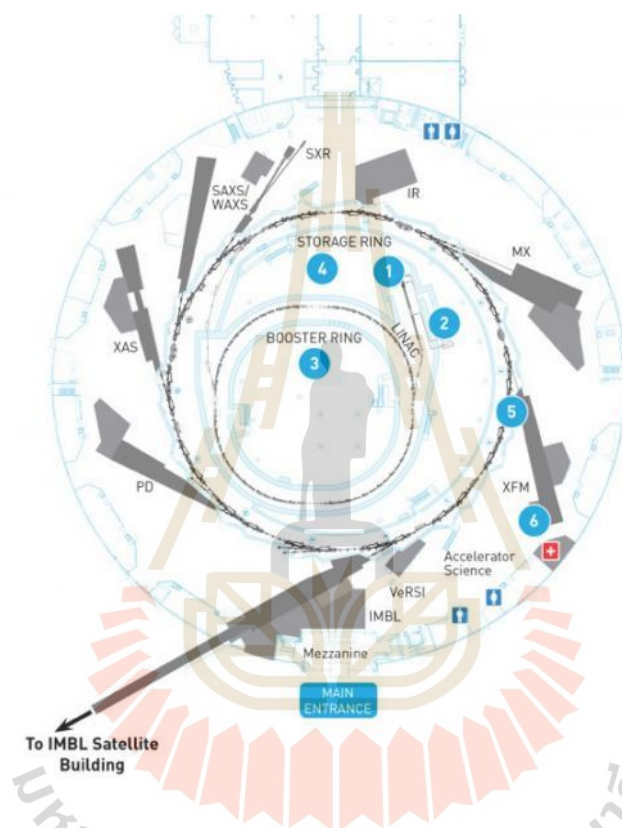


Figure 2.15 Core components of the synchrotron.

Due to the dynamic changes in the electrical fields, the charged particles in close proximity experienced an initial acceleration, resulting in their attainment of the speed of light. Subsequently, the particles are directed into a booster ring (3) in order to augment their energy levels to multiple giga-electron volts. This is achieved by subjecting the particles to magnetic fields that are precisely calibrated to match their velocity. Subsequently, the objects are transferred to an external storage ring, which is of a circular configuration (4). In a location characterized by the absence of material substance, the energy of the entities in question exhibited a continuous and unceasing

flow. The emission of synchrotron light occurs tangentially to the trajectory of electrons as they experience deflection within the storage ring due to the presence of a magnetic field. The introduction of the released radiation was necessary to facilitate its utilization in the many tests conducted through the beamlines (5). Synchrotron radiation exhibits a wide range of wavelengths, encompassing four distinct types: infrared, visible light, ultraviolet, and x-rays. The emitted radiation has an exceptional luminosity that surpasses that of conventional light sources by several orders of magnitude. A wide range of materials, including metals, semiconductors, polymers, and protein molecules, can be examined at the atomic and molecular level in scientific contexts.

#### 2.4.1.2 The uniqueness properties of a synchrotron radiation.

The utilization of synchrotron radiation has demonstrated greater efficacy compared to alternative sources of X-ray radiation due to its possession of certain distinctive features. The discernible characteristics of synchrotron light can be categorized as follows:

**Wide continuous spectrum and adjustability :** The emission of synchrotron radiation from a bending magnet has a continuous spectrum and possesses the capability to be adjusted across a broad range of energy levels. Figure 2.16 shows the complete spectral range that synchrotron radiation covers. This comprehensive compilation encompasses the entirety of the electromagnetic spectrum, spanning from the infrared region to the hard X-ray range. Synchrotron radiation can be conceptualized as an emission resembling "white light" due to its encompassment of the entire range of colors. Furthermore, the energy spectrum of synchrotron radiation can be customized to suit the specific requirements of a given material.

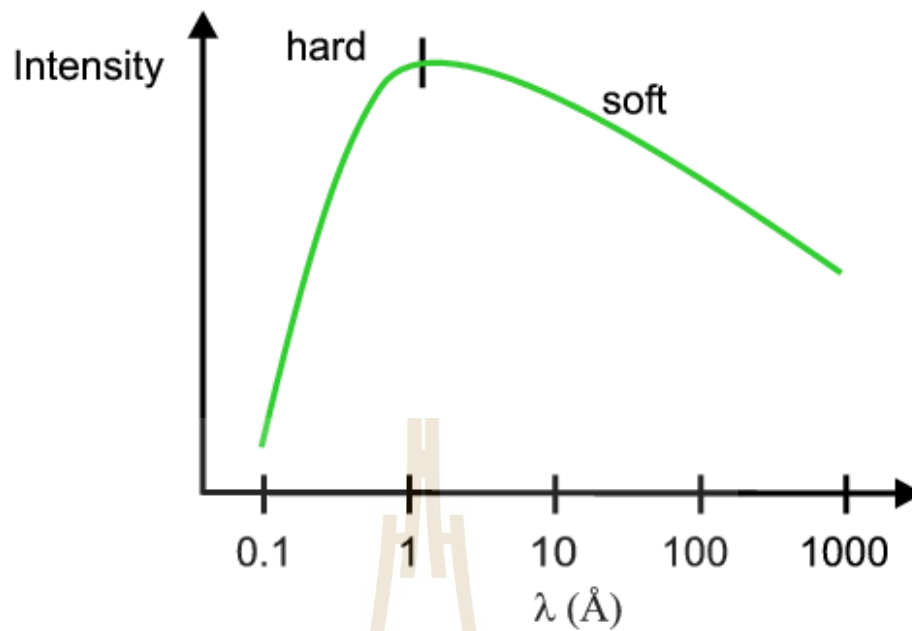
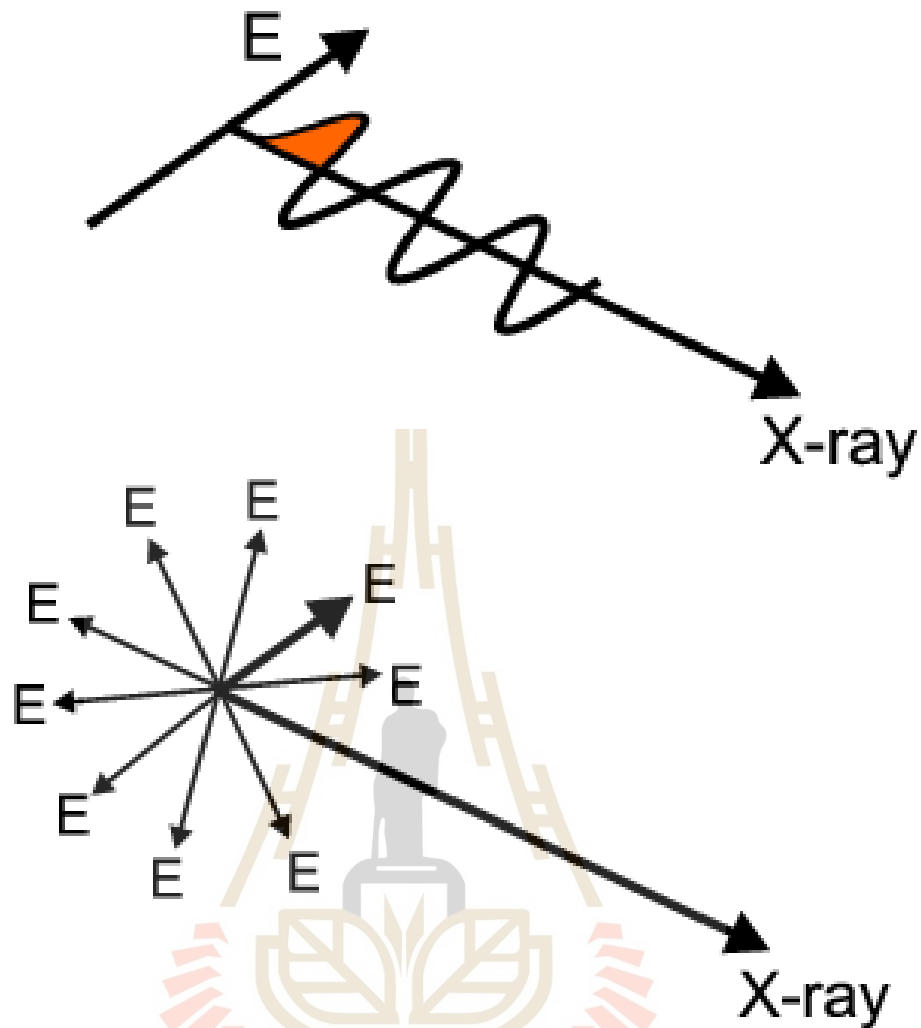


Figure 2.16 The spectrum range of the synchrotron radiation.

**Polarization:** The synchrotron radiation released from a bending magnet exhibits a linearly polarized field, namely a horizontal polarization. In contrast, the synchrotron radiation observed both above and below the orbit has a circularly polarized field. The polarization of synchrotron sources exhibits a horizontal orientation, as depicted in the accompanying diagram. Conversely, the X-ray radiation emanating from laboratory sources exhibits omnidirectional vibrational characteristics. This particular trait possesses several advantages, among which is its applicability in the examination of magnetic materials.



**Figure 2.17** Both linear and circular polarizations of synchrotron radiation exist.

**Very high intensity (flux) and high brilliance:** The photon flux intensity generated by synchrotron radiation exhibits a significant magnitude. The flux is generally contingent upon the beam current, denoting the quantity of electrons that traverse the ring within a specific temporal interval. Synchrotron radiation exhibits a notably elevated beam current, surpassing that of a normal X-ray source. By utilizing synchrotron radiation, which exhibits a notably elevated flux and brightness, it becomes feasible to acquire data of exceptionally high resolution and assess samples that are exceedingly minute and diluted.

**Pulsed character:** Specialized experiments can use the pulsed nature of synchrotron radiation, as it is emitted in discrete bursts of time rather than being

continuous. This characteristic becomes advantageous in certain research endeavors.

### **2.3.1.2 Synchrotron light research institute (SLRI)**

The establishment of the Synchrotron Light Research Institute occurred twenty-two years ago. The Thai government, in collaboration with a consortium of esteemed scholars and educators, has reached a consensus to acquire a pre-owned synchrotron facility from Japan. This gadget was owned by SORTEC Corp., a conglomerate consisting of various Japanese firms. Initially, its development was intended for utilization in an X-ray lithography technique employed for the fabrication of integrated circuits. The utilization of synchrotron light in manufacturing was previously prevalent, but its feasibility diminished as production methodologies underwent evolution. Subsequently, Japan formulated a plan to distribute the equipment to a nation that would express gratitude for the gesture. Several other nations expressed interest in utilizing the synchrotron technology; however, the Japanese government finally selected Thailand. Chiang Mai University, Suranaree University of Technology, and the National Research Council all had significant roles in the matter. The Synchrotron Light Research Institute is a publicly funded organization that has established itself as a leading authority in the field of high-tech lighting up to the present time. The Institute plays a crucial role in Thailand's scientific infrastructure, providing its services to the local community as well as to individuals in the ASEAN area and beyond. The system maintains a 95% uptime rate and provides service to users for a total of more than 4000 hours annually.

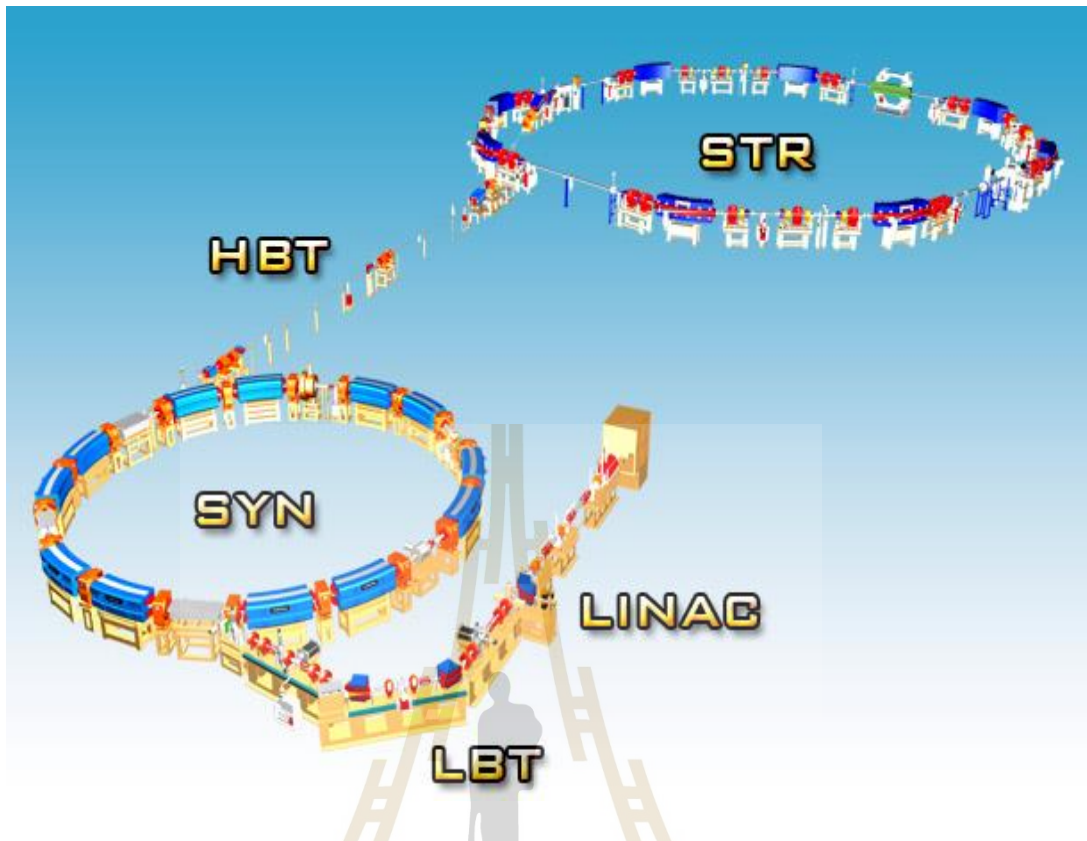


**Figure 2.18** The core of the Synchrotron Light Institute for Medical Research.

Figure 2.17 depicts the crucial component of the SLRI. The linear accelerator (LINAC), known for its capability to accelerate particles up to 40 MeV, served as the initial site for electron acceleration. Prior to entering the booster synchrotron, the electrons underwent traversal through the low-energy beam transport line, commonly referred to as the LBT (SYN). Radio frequency waves with a frequency of 118 MHz are employed to facilitate the re-acceleration of electrons, leading to the generation of electrons possessing energy of up to 1.2 GeV upon traversal through the booster. Subsequently, the high-energy beam transport line effectively guides the aforementioned electrons into their designated location within the storage ring, commonly referred to as the STR (HBT).

The bending magnets of a storage ring emit synchrotron light, which photon beamlines use to transport to the experimental stations. Certain forms of detrimental electromagnetic radiation can only be mitigated with the implementation of ultrahigh vacuum conditions within the photon beamlines. Several optical filters are currently

employed along the beamlines for the purpose of concentrating, scattering, and collimating the light. The experimental facilities, wherein the samples under investigation are housed, receive illumination of superior quality from a light beam. The utilization of synchrotron light in experimental methodologies has consistently demonstrated its efficacy in advancing research across diverse material domains. Synchrotron radiation techniques are unparalleled in their ability to provide scientists with comprehensive insights into the elemental compositions, as well as atomic and molecular structures, of materials under investigation. The following is a concise overview of the beamlines and the methodologies they utilize. Beamline I is a research facility dedicated to the study of materials through the application of time-resolved X-ray absorption spectroscopy. This beamline was generously provided by Bonn University in Germany. Its primary focus is on investigating the chemical and structural properties of materials in real-time. The second beamline, referred to as Beamline II, is dedicated to the examination of nanoparticle size and the utilization of tiny and broad-angle X-ray scattering techniques for the purpose of investigating the nanostructure properties of materials. The utilization of photoemission electron spectroscopy at Beamline III for the investigation of surface, interfacial, and thin-film materials. The investigation of surfaces, interfaces, and thin films through the use of photoemission electron microscopy at Beamline IV has been the subject of scholarly inquiry. The utilization of infrared spectroscopy has found significant applications in the fields of biomedicine, biology, and environmental science. Specifically, the implementation of Beamline V has been crucial in these domains. Beamline VI is a collaborative project between Suranaree University of Technology, the National Nanotechnology Center, and the Synchrotron Light Research Institute. It serves as a facility for doing chemical and structural investigations on various materials. Line 7: The generation of microstructures with high aspect ratios by the utilization of deep X-ray lithography. The utilization of micro-X-ray fluorescence spectroscopy and imaging techniques is employed for the purpose of studying and mapping the elemental composition. This particular application is conducted at beamline 8. The primary area of interest for Beamline IX is the application of the hard X-ray technique in the field of protein crystallography. X-ray absorption spectroscopy is a widely employed

technique in the fields of material chemistry and physics, particularly at Beamline X.

### **2.4.2 The X-ray photoelectron spectroscopy (XPS)**

XPS is an analytical technique with surface sensitivity wherein the surface of a material is subjected to x-ray bombardment and the kinetic energy of the released electrons is measured. The approach possesses two primary attributes that contribute to its efficacy as an analytical tool: surface sensitivity and the ability to disclose chemical state information pertaining to the elements present in the sample. XPS has been extensively employed for the examination of surface chemistry in a wide range of substances, encompassing plastics, textiles, dirt, and semiconductors. However, it is worth noting that hydrogen and helium have not been subjected to investigation using this technique. Surfaces facilitate the interaction between different materials and are present in all materials. Surfaces have a major impact on numerous aspects, including wettability, adhesion, corrosion, charge transfer, and catalysis, making their understanding and study crucial. The photoelectric effect, which was first observed by Heinrich Hertz in 1887, forms the basis of XPS. The researcher observed that the exposure of surfaces to light resulted in the liberation of electrons. The Nobel Prize in Physics was conferred upon Albert Einstein in 1921 in recognition of his formulation of the concept he had introduced in 1905. The observation of photoemission in response to x-ray irradiation was initially made by Robinson and Rawlinson in 1914. Subsequently, in 1951, Steinhardt and Serfass developed photoemission as an analytical tool. Kai Siegbahn, a researcher affiliated with the University of Uppsala in Sweden, made substantial contributions to the progress of x-ray photoelectron spectroscopy throughout the 1950s and 1960s. His work had a crucial influence in the advancement and current state of this technology. In 1981, he was awarded the Nobel Prize for his notable achievements in the field of high-resolution electron spectroscopy, which is popularly known as electron spectroscopy for chemical analysis (ESCA).

#### **2.4.2.1 Principle of XPS**

##### **2.4.2.1.1 Generating photoelectrons**

XPS is a surface examination technique that enables the measurement of a sample's properties within a depth range of approximately 2 to 5 nm. XPS is a

technique that can provide insights into surface chemistry, specifically pertaining to chemical bonds and electronic states. The measurement is derived from the photoelectric phenomenon. In order to do this, a specimen was subjected to mild x-ray radiation, resulting in the stimulation of electrons within the specimen's core level, causing them to transition to vacant states. The X-ray photoelectron spectroscopy (XPS) technique was employed to examine and quantify the kinetic energy of the excited electrons. A typical XPS spectrum exhibits the quantification of released electrons at various energy levels, including kinetic and binding energies. The elemental composition of a given substance can be determined by assessing the binding energy of its electrons relative to a standardized reference. The magnitude of the binding energy is directly proportional to the quantity of electrons present within the atomic nuclei of the substance. The electron arrangement of atoms serves as a reliable predictor of their binding energies.

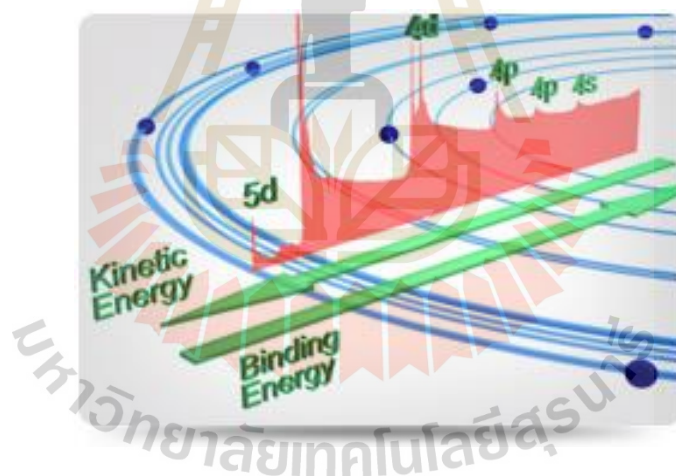


**Figure 2.19** Within the atom resides the electrical state.

XPS peaks shown in Figure 2.18 show the electronic states connected to different atomic orbitals, such as 1s, 2s, 2p, 3s, and so on. XPS peak data has discernible Gaussian-Lorentzian curves. The magnitude of the full width at half maximum (FWHM), which is crucial in detecting the chemical bonds present in samples, is influenced by several parameters, such as the resolution of the detector and the size of the X-ray beam. The inclusion of an electron from an adjacent atom in the overall count of

released electrons is attributed to its measurement. All electrons liberated from an atom, including those emanating from adjacent atoms within a given specimen, will be subjected to measurement. The presence of nearby electrons would result in a discernible alteration in the full width at half maximum (FWHM) of the observed phenomenon. Consequently, the data pertaining to the Full Width at Half Maximum (FWHM) might be employed to ascertain the correlation between atoms, either those in proximity or the chemical bonds that link them. Equation (2.1) offers a theoretical framework elucidating the underlying principles governing the kinetic energy of photoelectrons liberated using X-ray photoelectron spectroscopy (XPS) technology.

$$E = E_k + E_B + \emptyset \quad (2.1)$$

In this context, the symbol  $E$  represents the energy associated with a photon,  $E_k$  denotes the kinetic energy of the electron that is emitted,  $E_B$  represents the binding energy of the electron within the material, and  $\emptyset$  is used to denote the work function of the material. The work function refers to the minimum energy threshold required for an electron to be liberated from a substance and then remain stationary within a vacuum. The binding energies of core electrons can exhibit a wide range, spanning from tens of electron volts (eV) to kiloelectron volts (keV), but the work functions commonly observed are typically on the order of electron volts (eV). Because of the need to excite multiple orbitals in most elements, soft X-rays (200–2000 eV) are typically employed. The emission of a photoelectron occurs when the entirety of the x-ray energy is transmitted to an electron located at the nucleus. The statement asserts that the energy of an x-ray, denoted as  $h\nu$ , can be expressed as the sum of the binding energy (BE) of the electron, representing its degree of attachment to the atom or orbital, the kinetic energy of the emitted electron, and the constant value of the spectrometer work function ( $\text{spec}$ ). The concept of electron binding energy pertains to the degree of tightness with which an electron is associated with an atom or orbital. The graphical depiction of this principle is depicted in Figure 2.19. It is important to keep in mind that the  $\text{spec}$  is included since the photoelectron binding energy is evaluated with respect to the Fermi level of the sample (and not the vacuum level).

Each element and orbital from which a photoelectron was emitted is recorded along with the corresponding peak energy. The term "O 1s" pertains to the electrons occupying the 1s orbital of an oxygen atom. The X-ray photoelectron spectroscopy (XPS) technique is predicated upon the emission of electrons from the sample, wherein the binding energies of these emitted electrons are lower than the energy of the x-ray source. The binding energy of an electron stays invariant when it is emitted from a material, irrespective of the x-ray source. The binding energy of photoelectrons remains invariant irrespective of the x-ray source employed in an experimental setting.

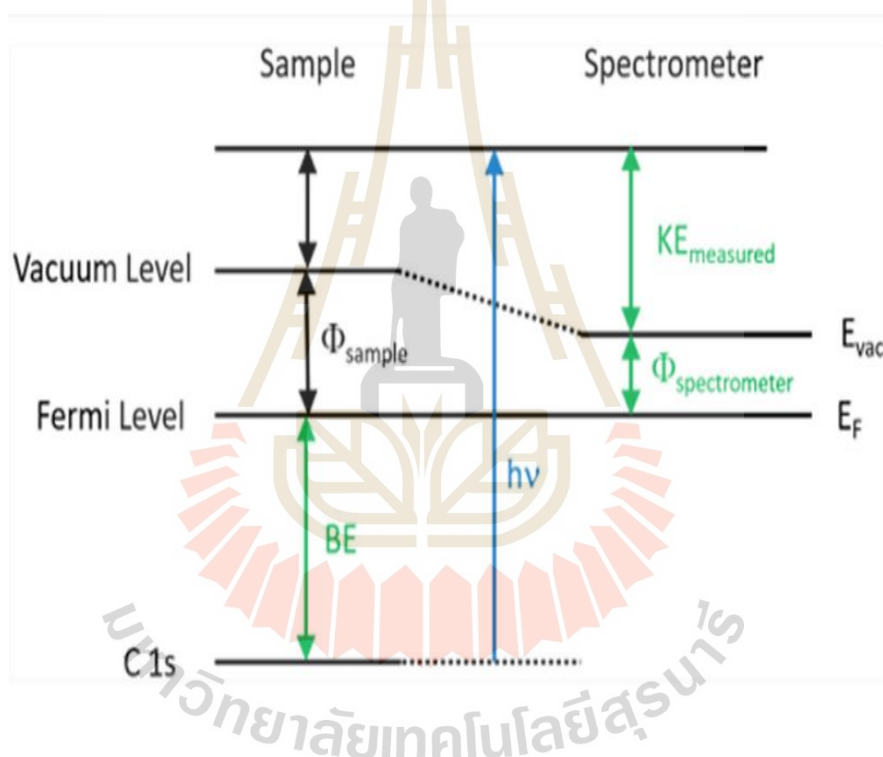


**Figure 2.20** Energy level diagrams illustrate the fundamental XPS equation, which encompasses  $h\nu$ , BE, measured electron  $K_{\text{measured}}$ , and the work function of the spectrometer.

#### 2.4.2.1.2 Auger electrons

When using XPS, low-energy x-rays (6 keV) are used to hit the sample and measure the kinetic energy of the electrons that are released. This is shown in Figure 2.21(a). The removal of one electron from the core of an XPS results in the formation

of a vacancy, sometimes referred to as a "hole," at the center. When an electron originating from a valence orbital with lower energy occupies the vacancy in this excited ionization state, it will undergo a process of relaxation. The relaxing process has the potential to liberate energy through two distinct mechanisms: x-ray fluorescence and Auger electron emission.

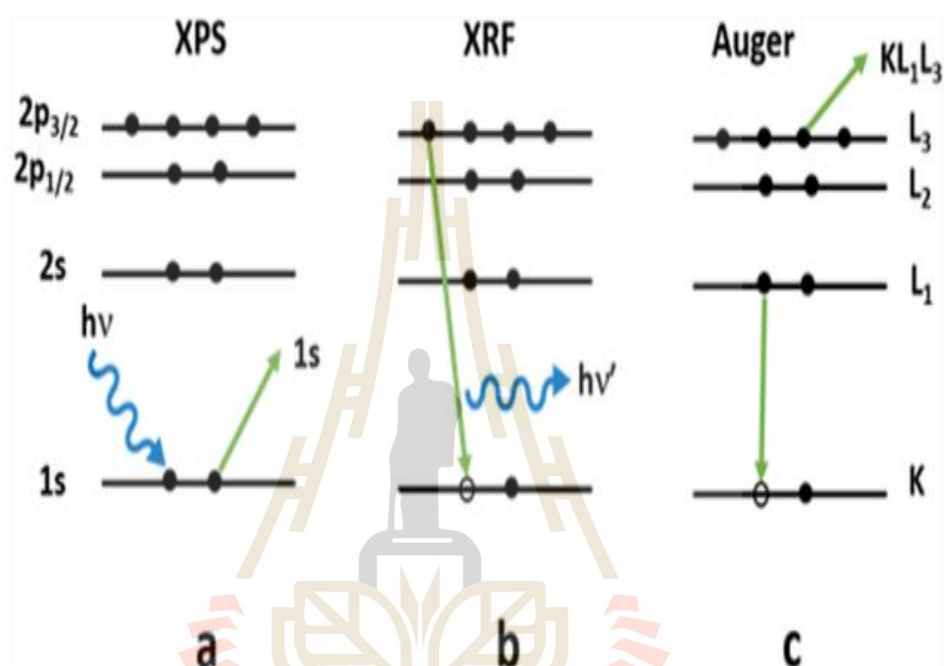


**Figure 2.21** The kinetic energy of the electrons emitted in XPS is determined by irradiating the sample with x-rays of low energy.

Given that X-ray fluorescence is not detected in the electron spectrum, as depicted in Figure 2.20(b), further discussion on this topic will be omitted. Auger electrons, which are produced through the mechanism depicted in Figure 2.20(c), have historically been utilized for quality control purposes in X-ray photoelectron spectroscopy (XPS). Traditionally, the nomenclature of Auger peaks has employed the K, L, and M labels for atomic orbitals. As an illustration, the letters KLL denote the K-orbital source of the first ejected electron, the L-orbital source of the electron that occupied the core hole, and the L-orbital source of the ultimate Auger electron. Each of these contributions collectively leads to the prominent oxygen Auger peak. As depicted in Figure 2.20(c), subscripts can be employed to denote the specific L, M, or

N orbital under consideration. The expression for the kinetic energy of the Auger electron that is emitted during the KLL transition, which is one of the three transitions associated with the Auger process, is given by Equation (2.2).

$$KE_{\text{Auger}} = BE(K) - BE(L1) - BE(L3) \quad (2.2)$$

There exists a close relationship between the binding energies of particular orbitals within the atom from whence an Auger electron originates and the kinetic energy of the Auger electron. The Auger electron's equilibrium binding energies ensure that its kinetic energy remains unchanged regardless of the x-ray excitation energy. Consequently, the anticipated binding energy of the Auger electrons will vary based on the specific x-ray source employed for their excitation. It is helpful to know that the binding energy of photoelectrons stays the same with the x-ray source, but the binding energy of Auger electrons changes. This is because Auger lines and photoelectron lines overlap in frequency. Modifying the x-ray source frequently allows for the resolution of these overlaps, as illustrated in Figure 2.21. The fact that we can achieve the resolution clearly demonstrates this. Magnesium x-rays stimulate silver, revealing an Auger peak with the highest magnitude and a binding energy of 902 eV. Nevertheless, when silver is excited by Al x-rays, a spatial displacement of the peak occurs, resulting in the observation of a binding energy of 1135 eV. Since the beginning of time, quality assurance in XPS has utilized Auger electron detection, as shown in Figure 2.22(c).

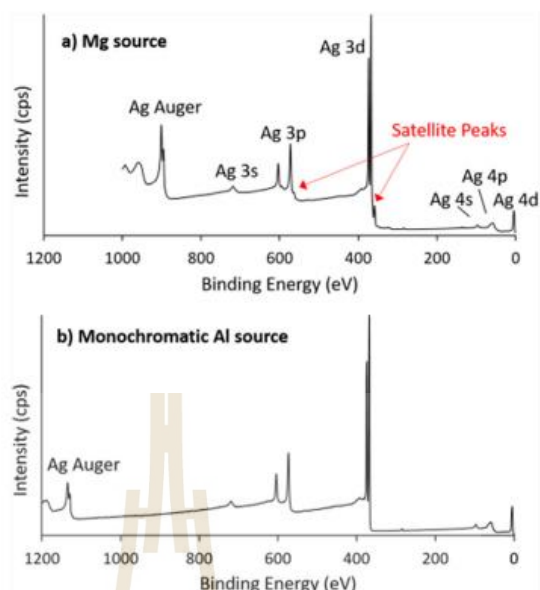


Figure 2.22 XPS spectra of a)Mg source and b)Monochromatic source.

#### 2.4.2.2 Chemical shift

X-ray photoelectron spectroscopy (XPS) survey scans offer the capacity to detect the presence of metal elements and determine their respective quantities. Nevertheless, it is important to acknowledge that this approach holds significance beyond these essential features, as it demonstrates further applications. The data presented in Figure 2.22 illustrates the presence of many peaks with varying binding energies upon close examination of some orbitals. This phenomenon is the result of several chemical changes. Chemical shifts occur when atoms undergo changes in their chemical surroundings due to interactions with various elements or different oxidation states. Data processing software employs Gaussian-Lorentzian peak fitting to streamline the spectra, thereby facilitating the reanalysis of the data. Therefore, we can identify the distinguishable chemical environments by analyzing the binding energies associated with these peaks. This methodology allows for a higher level of accuracy in data representation.

### 2.4.2.3. Sample charging

The task of handling insulating samples presents difficulties due to the typical unavailability of direct electrical contact with the analyzer. The phenomenon of sample charging arises due to the absence of electron replenishment at the surface. The phenomenon of differential charging, characterized by non-uniform charge distribution on the surface of a sample, can lead to broadening or splitting of peaks. This phenomenon occurs due to the alteration in photoelectron energies resulting from the process of charging, hence leading to substantial shifts in the positions of the peaks. The continuous movement of electrons originating from the anode serves to alleviate the consequences associated with the charging of spectrometers utilizing an X-ray source.

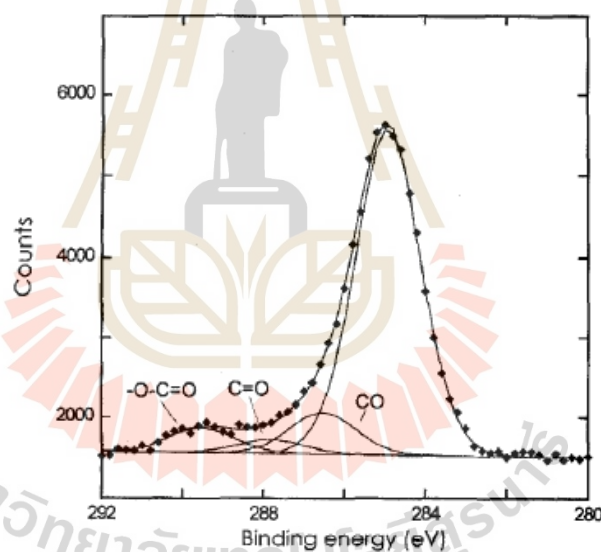


**Figure 2.23** A focused examination of the C1s area reveals distinct chemical shifts attributed to various bonding states involving oxygen.

### 2.4.3 X-ray absorption spectroscopy (XAS)

The inception of XAS dates back over a century, and its progress has been substantial throughout the intervening years. However, because it grew out of a relatively unexplored area of scientific inquiry and was only studied by a small group of dedicated scholars, this methodology was at first seen as a fascinating curiosity that

had no practical use and lacked a complete and strong theoretical framework that could explain and predict experimental observations made on gaseous, liquid, and solid (both crystalline and amorphous) substances. Fourier analysis was used by Sayers, Stern, and Lytle in 1971 to flip the experimental data they got from photoelectron wave-vector space, turning it into a radial distribution function. The initial determination of quantitative values was conducted for bond distance, coordination number, temperature, and disorder features. The field has made significant advancements at an exponential rate over the course of 44 years following the publication of that fundamental work. XAS and its associated methodologies are currently regarded as essential tools for advanced research in a wide range of disciplines, including materials science, solid-state physics and chemistry, catalysis, chemistry, biology, medicine, earth science, environmental studies, cultural heritage preservation, and nanoscience, among others. This introduction chapter provides a comprehensive summary of the key advancements that have contributed to the extensive utilization of XAS and its associated techniques for scientific characterization.

#### 2.4.3.1 Principle of XAS

The core principles underlying XAS can be succinctly elucidated within a concise statement. When a sample is exposed to an X-ray photon of sufficient energy, it has the potential to ignite a core electron within the material. The energy levels of the core electrons remain largely unaltered by the chemical environment in which they reside due to their occupation of confined states. The selectivity of XAS can be attributed to this particular component. The phrase "absorption edge" denotes the specific energy threshold at which a sudden and significant alteration occurs in the absorption coefficient. This particular aspect is indicative of the binding energy associated with the core level. The absorption edges, often referred to as sudden rises in absorption, correlate to the energy required for the ejection of a core electron into the lowest unoccupied molecular orbital (LUMO) or into the continuum, resulting in the creation of a photoelectron. The absorption discontinuity associated with the photoelectron originating from a 1s core level is commonly known as the K-edge. Conversely, the term "L-edge" is employed to denote the ionization event resulting

from the excitation or removal of a 2s or 2p electron. According to the data shown in Figure 2.23, the electron in an excited state possesses the capability to transition to either unoccupied bound levels or continuous unbound levels.

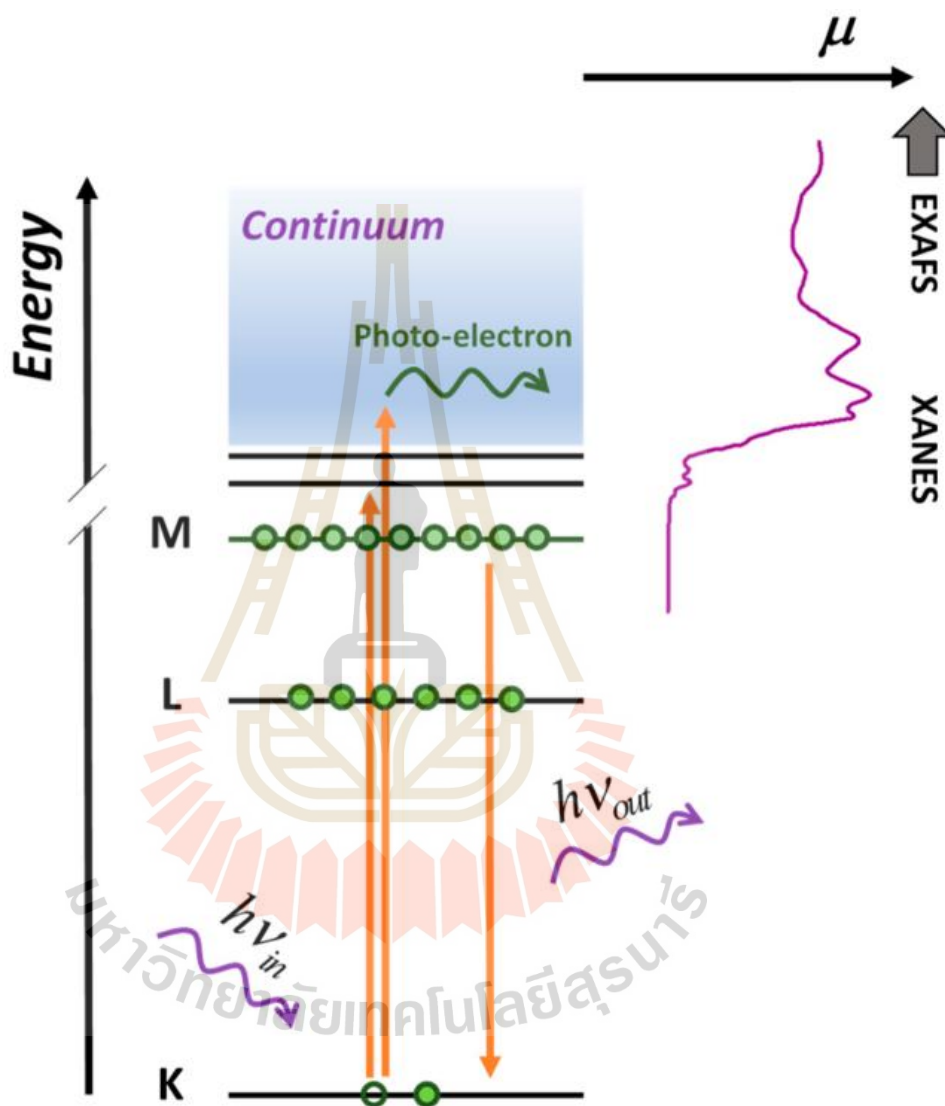


Figure 2.24 X-ray absorption process schematic.

The atoms in its vicinity can then scatter it back, a process known as back-diffusion. The interatomic distance determines whether the emitted electron and the back-scattered waves have a destructive or constructive interaction for a given photon energy. The result of this effect is a fluctuation in the X-ray absorption coefficient that

can be measured hundreds of electron volts (eV) above the absorption edge. This allows one to determine the local structure (number, nature, and distance of surrounding atoms) in the area immediately surrounding the photo absorber; this is known as the "Extended X-ray Absorption Fine Structure" (EXAFS). Specifically, the absorption coefficient strongly modulates at energies near the boundary. In this case, the electronic transitions to bound unoccupied states and/or multiple scattering events are responsible for the X-ray absorption near edge structure (XANES). Significant data on the surrounding coordination environment can be gleaned from XANES (type of coordination and its distortions). In conclusion, the oxidation state is reflected in the fine energy at which the absorption edge falls, which is directly proportional to the electron density on the photo absorber. Therefore, XAS provides a reliable, objective measure of atomic oxidation states in compounds.

**X-ray absorption near edge structure (XANES)** : XANES spectra reveal the oxidation state and coordination environment of metal atoms with great specificity (Figure 2.24). In general, higher oxidation states have higher K-edge absorption edge energies. The position of the incrementing changes as a result of 1s core hole shielding effects on the effective number of positive charges (or, in a simplified view, the oxidation state) (Shulman et al., 1976). As an example, in a single-electron atom, the electron feels the full charge of the positive nucleus. On the other hand, in a highly charged atom, the outer electrons are repelled by the negatively charged electrons and attracted to the positively charged nucleus. It takes more energy to excite an electron from an orbital when the metal's oxidation state is higher because a higher oxidation state results in a more positively charged atom. When a negative charge is applied to a metal, however, the X-ray energy spectrum changes to a lower level.

Transitions from 1s to np, where np is the lowest occupied p orbital of the absorbing atom, are the primary contributors to the K-edge spectrum. This transition, with  $l = 1$  (where  $l$  is the quantum number of the orbital momentum), is permitted by quantum mechanics and is typically strong. Pre-edge features resulting from 1s to (n-1)d transitions provide additional insight for transition metals with partially occupied d orbitals. These have a low intensity ( $l = 2$ , so they are formally forbidden or dipole-

forbidden), but they are detectable because they occur at energies just below the main absorption edge. When the ligand environment is broken from octahedral symmetry, the intensity of the pre-edge peak rises.

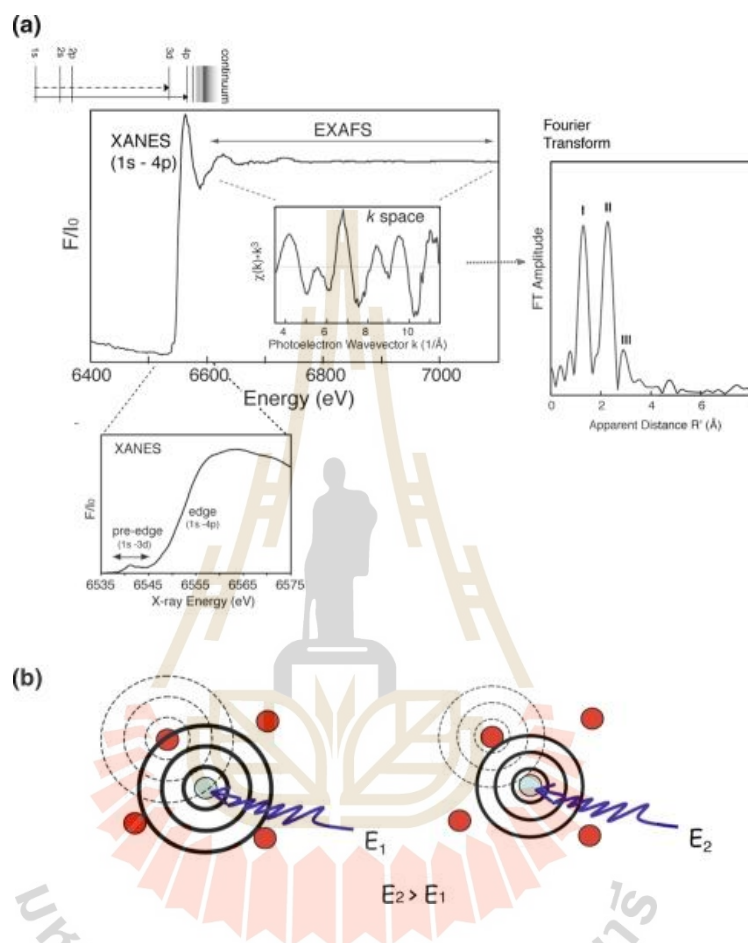


**Figure 2.25** a) XANES and EXAFS spectra of the manganese K edge. Upper left: XANES and EXAFS regions of the X-ray absorption spectrum of a PS II sample, b) A diagram showing the propagating and reflected photoelectron wave, which represents interference in EXAFS. The central (blue) atom absorbs and the surrounding atoms backscatter the photoelectron (red). The backscattered wave (blue dashed lines) is in phase with the outgoing wave (solid blue circular lines).

**Extended fine structure (EXAFS)** : The analysis of EXAFS enables the acquisition of comprehensive data regarding the partial pair distribution functions of the atoms around the absorber. This includes information on distances, mean square

deviations in distance, coordination numbers, and the species involved in coordination. EXAFS can be applied to any type of condensed matter, as its theory and interpretation do not rely on any assumptions of configurational symmetry or periodicity. EXAFS can be used on diluted systems because the fundamental physical process of XAS, the photo-excitation of a deep-core electron, is element specific. Thus, EXAFS plays an important role in a wide range of scientific fields, including the study of life, the environment, chemistry, materials science, cultural heritage, and more. In a nutshell, EXAFS is a vital skill for any synchrotron radiation lab.

In XAS spectrum, the difference between XANES and EXAFS can be thought of as a difference in regime. One of the limitations of this definition is that there is no single, overarching principle that distinguishes the two systems in question, even though they appear to share the same conceptual principles. Most people place XANES at an energy level where the potential is 50 eV above the edge, while they place EXAFS at an energy level where the potential is between 50 and 1000 eV above the edge.

#### **2.4.4 X-ray diffraction (XRD)**

Due to the growing importance of radiotherapy throughout the war years, much research was conducted on the quantification of radiation dosage during this time. X-ray spectra were of greater interest to the scientific community. By creating interference patterns when x-rays impinged on and were diffracted by a crystal in 1912, the x-ray diffraction experiment proved beyond a reasonable doubt that x-rays are electromagnetic waves. Max von Laue, winner of the Nobel Prize in Physics, provided a concise summary of the evidence based on both the electromagnetic radiation model and the clustered, particle-like explanation. The father-and-son Bragg duo identified x-rays as electromagnetic (EM) waves after using them as a crystallographic tool. X-rays, they found, can interfere with lattices and provide information about crystal structure that visible light cannot because of their atomic-scale wavelength. The first images from which the atomic structures of solids could be inferred were made using this technique (Kitaigorodsky et al., 1957), which was established in the early 20th century. The Braggs were able to accurately describe even the most basic

structures, such as those of rock salt (NaCl) (Burger et al., 1961). An analysis of the x-ray intensities reflected by crystals also provided support for Niels Bohr's atomic model and the idea of chemical bonding (Sheldrick et al., 1998). In addition to publishing a popular textbook on x-rays and crystal structure, the Braggs also trained many people and established a vast network of collaboration. However, because to the difficulty of inferring from x-ray data to the structure of matter, progressing from simple to more complicated structures was time-consuming. The structure of sterols was discovered in the 1930s by Desmond Bernal and others, among them Dorothy Crowfoot (later Hodgkin) (Gamilton et al., 1972), and in the decades that followed, the structures of other biologically relevant compounds, such as penicillin and vitamin B12, were also determined (Borisov et al., 1981). Since its inception, X-ray analysis has required extensive effort and original thought (Vainshtein et al., 1981).

Since 1964, when X-ray technologies were first used for structure determination, there has been no straightforward approach for converting experimental data into a structural model. It takes a scientist's comprehensive chemical understanding, creativity, and intuition to tackle complex problems. Multiple mathematical treatments, each tailored to the unique characteristics of the experimental data, are also required. In addition, the intricacy of the structure increases the amount of experimental data that must be collected and analyzed. For simple compounds, the calculations could be done by hand using paper and pencil. These days, it's nearly impossible to make a structure determination without the aid of an electronic computer. However, the scientist's data management skills remain vital, as it is not always easy to simply input experimental data and obtain the resulting numerical structure.

In the 1930s, x-ray analysis was applied in various areas of life science, including virology, due to the creation of crystalline forms of plant viruses. Similar subunits are packed together frequently in a small virus, as was discovered by Crick and Watson using such analysis in 1956. At the same time, they and Maurice Wilkins were working to determine the structure of DNA, an achievement for which they were awarded the 1962 Nobel Prize (Brusentsev et al., 1963). The contributions to DNA research made by Rosalind Franklin, who passed away in 1958, are now being recognized and honored.

#### 2.4.4.1 Principle of XRD

The phenomenon of constructive interference resulting from the interaction between monochromatic X-rays and a crystalline sample serves as the fundamental principle behind X-ray diffraction. The X-rays under consideration are generated by the utilization of a cathode ray tube. These X-rays are next subjected to filtration processes to ensure their monochromaticity, followed by collimation to enhance their focalization. Finally, the focused X-rays are directed towards the sample of interest. When a monochromatic x-ray beam interacts with a crystal. Through vibration, the atomic electrons in the crystal are set into motion. and they're accelerated at the same frequency as the incident ray. Subsequently, the electrons that have undergone acceleration proceed to emit radiation in a uniform manner, exhibiting the identical frequency as the initial x-rays. A problem will only arise if the wavelength of the incident radiation is considerably greater than the dimensions of the crystal. As a result, the X-rays that are released exhibit a state of coherence, with their waveforms aligned in phase. However, this is impossible because the wavelength of X-rays is almost identical to the atomic dimensions. The radiation of electrons is out of sync with itself. A diffraction pattern (i.e., maxima and minima) is created when these radiations interfere with one another in either a constructive or destructive way.

Bragg proposed a solution to the problem of X-ray diffraction from a crystal by viewing it as the reflection of X-rays from the atomic planes of the crystal in accordance with the laws of reflection. A crystal with Miller indices  $[hkl]$  can be thought of as a collection of parallel atomic planes, with a distance of  $d$  between each pair. Imagine a beam of monochromatic X-rays with a given wavelength incident on the plane at an angle such that the incident rays are perpendicular to the paper's surface. Let P and Q on the crystal planes be the origin and reflection points for two parallel incident rays, AP and BQ, which then continue along PA' and QB'. If the distance between APA and BQB is an integral multiple of, constructive interference and a maximum will be observed.

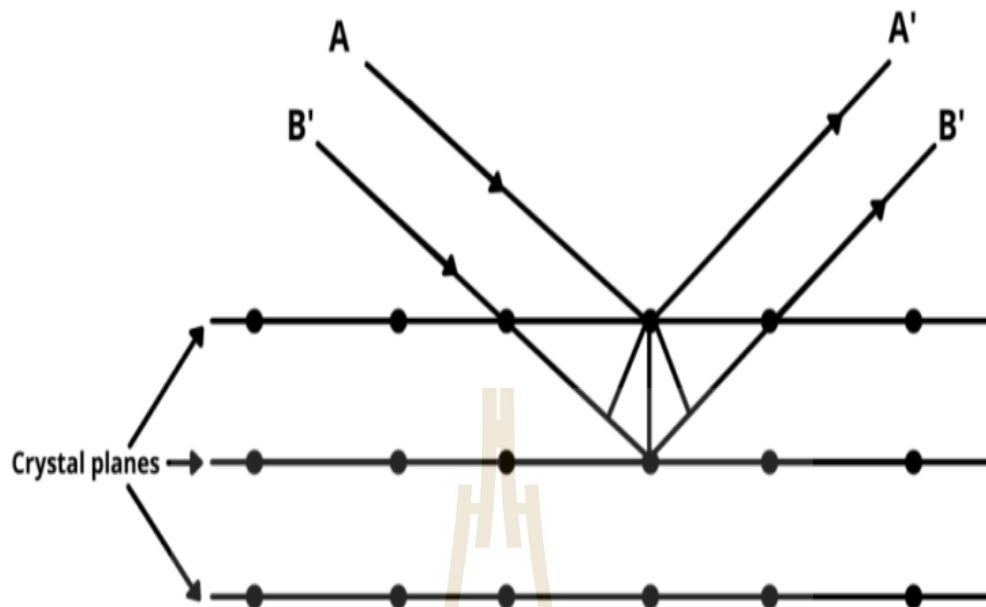


Figure 2.26 A simplified model of the Bragg equation.

Crystals are ordered arrangements of atoms, and X-rays can be thought of as electromagnetic radiation waves. When X-rays hit a crystal, the atoms scatter them, mostly because the rays interact with the atoms' electrons. Elastic scattering is the name given to this process, in which the electron plays the role of the "scatter." When scatters are arranged regularly, the resulting spherical waves also behave predictably. In most directions, these waves cancel each other out through destructive interference, but in a few, as determined by Bragg's law:

$$2d\sin\theta = n\lambda \quad (2.3)$$

For this expression, the wavelength is denoted by lambda, the distance separating atomic planes by  $d$ , and the angle of incidence of the X-ray beams by theta, where  $n$  is an integer (1, 2, 3,...  $n$ ). Because it "reflects" off an adjacent atomic plane, an X-ray beam travels in a more circuitous (but still parallel) path. It is necessary for

the incident X-ray beams to have a path length difference of exactly  $\lambda$ , for constructive interference to occur and a strengthened diffracted beam to be produced.

#### 2.4.4.2 Phase identification of XRD

The building blocks of a crystal are repeated patterns that are ordered in three dimensions. However, atoms in amorphous materials are scattered randomly throughout three dimensions, so they lack periodicity. This scenario calls for attention to X-ray scattering by atoms. X-rays exhibit a phenomenon of selective scattering in specific directions upon interaction with the lattice planes, owing to the periodic arrangement of atoms constituting the lattice structure. Extremely bright peaks will result from this (the width of the peaks depends on other variables). In the state of amorphousness, X-rays exhibit scattering phenomena in multiple directions, resulting in the generation of a wide and irregular peak ( $2\theta$ ) as opposed to localized peaks with high intensity. The presence of a significant quantity of amorphous phase will lead to the manifestation of peaks that correspond to the respective phase. Nevertheless, the sharpness of these peaks will be diminished as a result of the inherent characteristics of XRD patterns. This is because XRD patterns represent the combined contributions from all constituent phases. When the experiment is performed at a low angle, there is a possibility of observing a higher proportion of the amorphous phase in the diffraction pattern. In the event that both the crystalline and amorphous phases manifest peaks, it is anticipated that the crystalline phase will demonstrate a discernible and clearly defined peak associated with its favored orientation, whereas the amorphous phase will showcase a less pronounced and more diffuse peak indicative of its predominant peak. As a result, the amorphous phase will manifest its most notable peak on a single occasion. If the second peak is observable, it can be detected if its intensity is adequately high; however, the distinction between the two peaks will be minimal, as depicted in Figure 2.28.

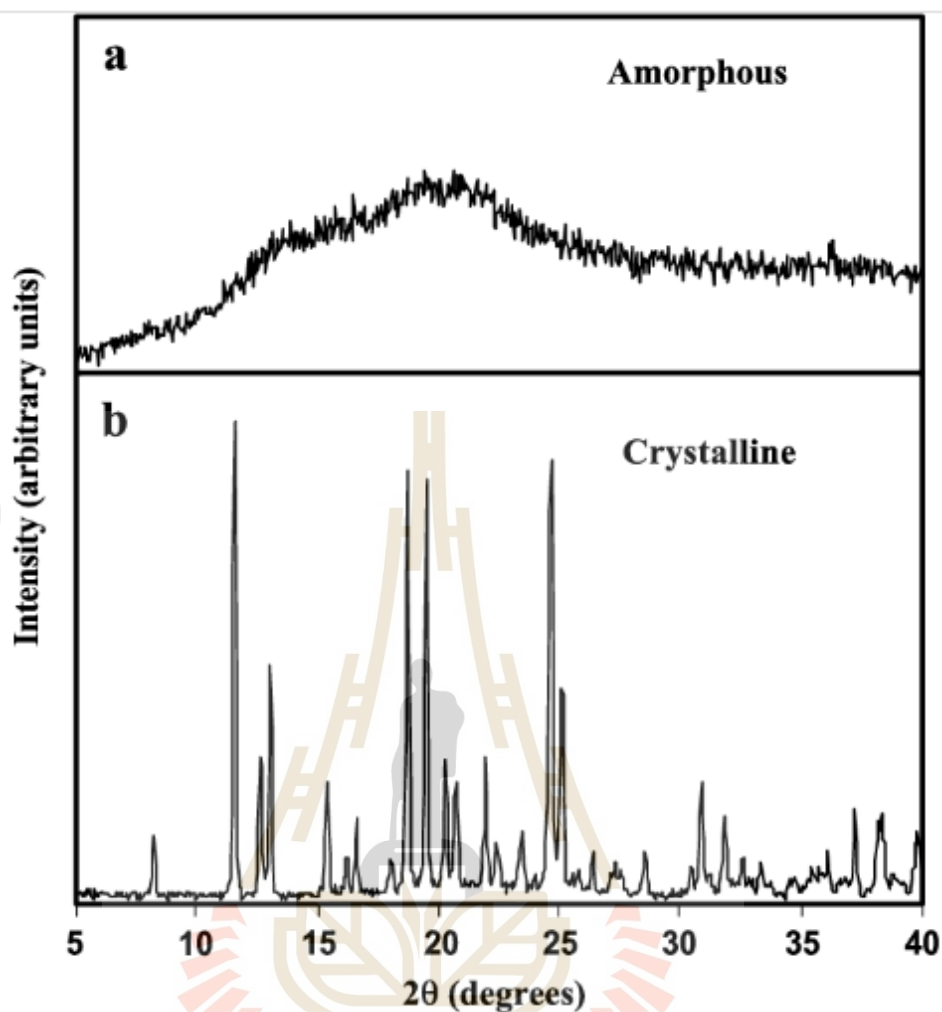


Figure 2.27 Amorphous sucrose (a) and crystalline sucrose (b) in powder X-ray diffraction patterns.

#### 2.4.5 Scanning Electron Microscopy-Energy Dispersive X-Ray (SEM/EDX)

##### 2.4.5.1 Principle of SEM/EDX

SEM-EDS is an abbreviation for scanning electron microscopy and energy-dispersive X-ray spectroscopy (EDX or EDS). In some cases, the resolution of SEM can be as low as 1 nm. Scanning electron microscopy provides a highly resolved image of the sample surface, allowing for the determination of its morphology and even topography. Although there are a wide variety of SEM machines, additional detectors, and techniques available to meet a variety of needs, they all function according to the same fundamental principle. SEM involves methodically wiping the sample surface

with an electron beam. Accelerated electrons are released from an electron source and guided to the sample via a series of electromagnetic lenses and apertures. As the electrons veer off course, they interact with the surface of the sample and generate unique signals. The sample's microscopic surface structures can be examined with SEM in far greater detail than with a standard light microscope. The resolution of a scanning electron microscope can be as low as 1 nm, which is much lower than that of a light microscope. Thus, SEM provides a more accurate portrayal of the sample topography on its surface.

SEM uses a focused beam of electrons to create a high-resolution, high-magnification image of a sample material. The sample's molecular makeup is altered by the action of this beam. SEM uses a series of measured electron energies produced by these interactions to construct a three-dimensional image. An x-ray is created by the impact of the electron beam on the sample. The x-rays are collected by EDX instrument, which then processes the data. There is a unique pattern of x-ray lines for each element. Energy dispersive x-ray spectroscopy is used to determine the element and analyze the material's composition. The EDX analysis produces a spectrum as a result. EDX spectrum is a frequency distribution of x-ray energies. Peaks in an EDX spectrum typically represent distinct energy states (when the most x-rays were received). These peaks tend to be specific to a single element. Greater intensities of spectral peaks correspond to greater abundances of the corresponding element. Specialized software is used to deconvolve overlapping peaks in mixtures.

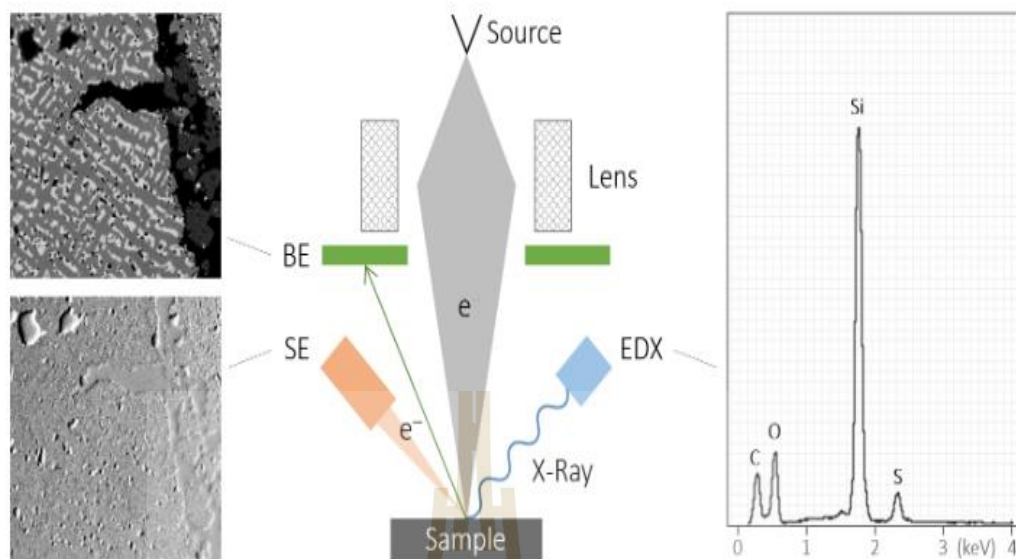


**Figure 2.28** Illustrates the setup of SEM system together with the inclusion of EDS capabilities.

## 2.4.6 The vibrating sample magnetometer (VSM)

### 2.4.6.1 Principle of VSM

The vibrating sample magnetometer (VSM) is a flexible method for measuring the magnetic moment of a sample subjected to a uniform magnetic field and vibration. This technique can detect changes as small as  $10^5$  to  $10^6$  emu. The magnetic field of the sample is perturbed as a result of the vibrating component, and this, in turn, induces an electric field in a coil according to Faraday's Law of Induction. Placing the sample in a uniform magnetic field ( $H$ ) will cause the sample to become magnetized (denoted by the letter "M"). The sample is held at the desired angle within sensing coils that are strategically placed in a VSM. As for the mechanically vibrating component of the sample, it is made to go through sinusoidal motion. The hysteresis loop exemplifies how the magnetization of a ferromagnetic material is "history dependent." After the material has been magnetized to its maximum level, the magnetic field can be reduced to zero and the magnetization will be retained in the vast majority of the material (it remembers its history). The electromagnet is turned on in advance of the testing, and if the sample has any magnetic properties, those

properties will strengthen in response to the increasing magnetic field. Once the vibration begins, a magnetic field  $H$  is created around the sample, and the magnetization of the sample can be studied as it varies in time with the vibration. Since the magnetization of a sample is proportional to the voltage induced in the sensing coils by variations in magnetic flux, using the converted signal values, the software creates a hysteresis loop, a graph of magnetization  $M$  versus the magnetic field  $H$  strength.

The primary benefit is the reliability and accuracy of VSMs. Once detection arrangements for the coils have been developed, measurements can be taken from a variety of angles. Once the detection coils are set up properly, the benefit of sample vibration perpendicular to the applied field will become apparent. In other words, you can examine the sample from a variety of perspectives. The coils are placed so that they penetrate deeply into the applied field, as shown in Figure 2.29, mitigating the effects of sample position variation and external field variation. The demagnetizing effects of the sample make it unsuitable for determining the magnetization loop or the hysteresis curve. Another issue is that it is not possible to regulate the temperature dependence of the VSM used in the third-year laboratory.

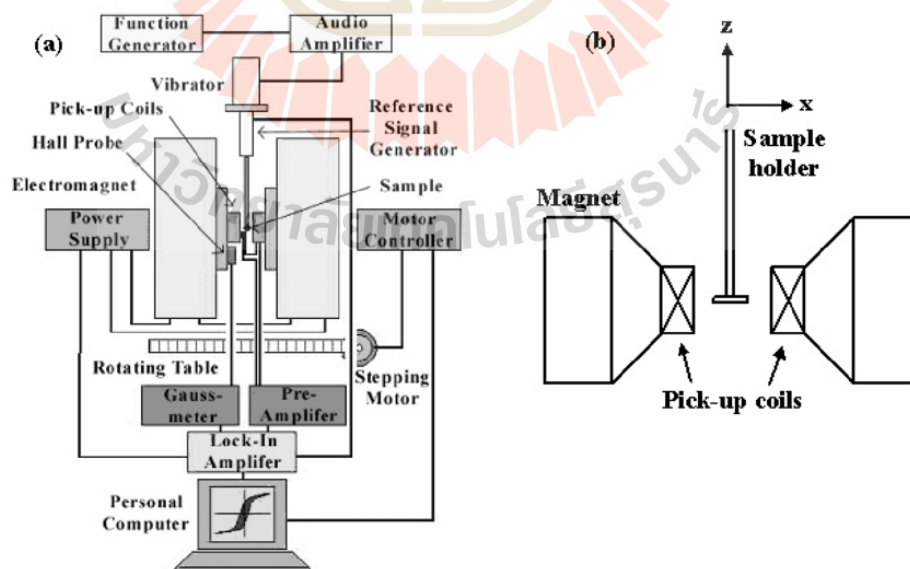


Figure 2.29 A representation in schematic form of the VSM.

### 2.4.6.2 Hysteresis Loop

The B-H hysteresis loop tracer consists primarily of two coils, one of which contains the sample to be analyzed, while the other serves as a control. Once a sample is placed in the pickup coils, a voltage is generated across the difference amplifier that is proportional to the rate of change in the vector field. Following its journey through an integrator, a voltage that is proportional to the intrinsic induction is transmitted to the Y-amp of the oscilloscope. Oscilloscope hysteresis loops are produced when this voltage is added to an X-voltage representing the magnetizing field generated by the solenoid in the absence of the sample. Calibrating an oscilloscope involves establishing a trace by balancing and adjusting the phase. They are carried out to guarantee the linearity of the magnetizing field and the correspondence of all vectors to the applied field. The magnetic properties can then be evaluated by conducting measurements.

Heating the sample with the coils allows for the observation of temperature effects on the response of the material to a magnetic field. However, this could cause the system to overheat, which could lead to a breakdown. When compared to a VSM, the visualization provided by a BH-looper can be more informative about the behavior of a given material. The display only provides qualitative, rather than quantitative, information about the magnetic properties of a material because the values plotted on the scope are only proportional to the absolute values. Overall accuracy is poor when compared to a VSM. It is possible to tell whether a material is soft or hard magnetically by observing its hysteresis loop on an oscilloscope. It is for this reason that a magnetic tape factory uses it to regulate the levels of ferromagnetic oxides in the tapes.

The magnetomotive force is denoted by the vector field  $B$ . Magnetization, denoted by the symbol "M," is the magnetic moment of a solid expressed in terms of its volume. The intensity of a magnetic field is measured in units called H fields. The equation establishes a connection between these three values.

$$B = \mu_0 ( H + M ) \quad (2.4)$$

with the permittivity of empty space set at 0. The hysteresis loops for a magnetic material are used in Figure 2.28 to illustrate the disparity between these values. For specific values of  $H$ , it is shown that the  $B$  field increases at a constant rate while the magnetization eventually saturates. Magnetization is created by electrons' spin and orbital angular momentum within the solid. To create  $H$ , electrical currents are used to create energy outside of the material. By combining  $H$  and  $M$ , which represent the gap between the quantities and include the permittivity of empty space, we obtain the  $B$  field, as shown in the preceding equation.

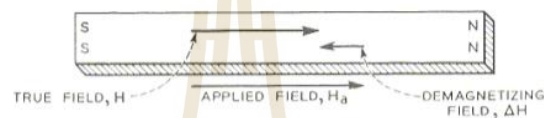


**Figure 2.30** Illustrates a magnet that has lost its magnetization when placed within a magnetic field.

Figure 2.29 is a representation of a bar magnet in a magnetic field and serves to highlight the distinctions between the three parameters. The diagram is quite old, so the labels are also outdated. In this case, the "true" field refers to the magnetization  $M$ , and the "applied" field is the vector field  $B$ . Although the arrows show the strength and direction of each parameter, they are not literal. Figure 2.29 demonstrates how much more powerful the magnetization is compared to the demagnetizing field.

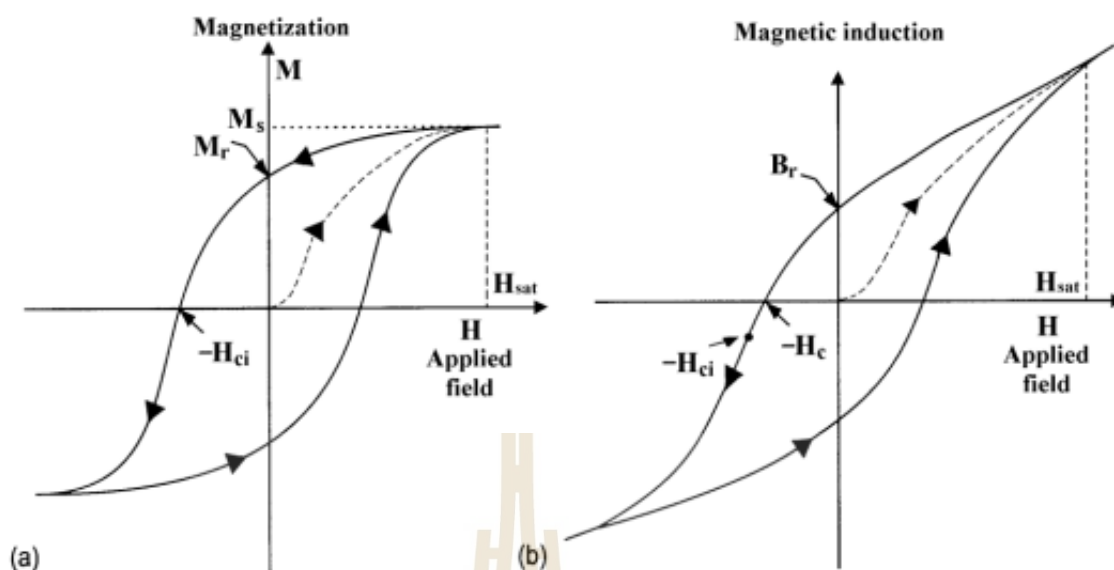


**Figure 2.31** Graphs the magnetic (M) and electric (B) hysteresis loops versus applied magnetic field (H).

It is possible to gain an understanding of the material other magnetic properties by referring to figure 2.30 and examining the two sketches that represent B and M against H. The left-hand curve can be used to demonstrate magnetization saturation and residual magnetization after an applied field has been removed. The  $B_r$  of residual induction and the maximum value of the applied field are both displayed in the right-hand diagram. The properties of the material are sensitive to the values of the three parameters M, B, and H.

## 2.4.7 The cyclic voltammetry (CV)

### 2.4.7.1 Principle of The cyclic voltammetry

Cyclic voltammetry serves as the fundamental basis for electrochemical analysis. In this particular case, the measurement of the current is conducted through the execution of a "sample" of the electric field, wherein the potential is systematically varied between two specified values, oscillating from positive to negative and vice versa. The electrochemical characteristics of a substance can be comprehended by analyzing the data obtained through CV. The electrode capacitive characteristics can

be anticipated by examining the redox peaks, which represent the reduction and oxidation processes, in a cyclic voltammogram (Figure 2.30). Hence, the oxidation and reduction potentials of the substance can be ascertained.

CV is given a ramp signal to process. To begin the forward scan, a positive ramp (one with a positive slope) is applied; after the first half cycle, the voltage is inverted; and finally, a negative ramp is applied to reverse the cyclic voltammogram sign for the second half cycle. With the assistance of redox reactions, the system works toward reaching a state of equilibrium, during which it aims to return to the starting point from which it originated. It repeats in cycles, and those cycles reveal the history of the system's transformations. The behavior of the system (reversible, irreversible, or quasi-reversible) and the qualities of the material (capacitive nature, etc.) can all be inferred from a careful examination of the CV curve.

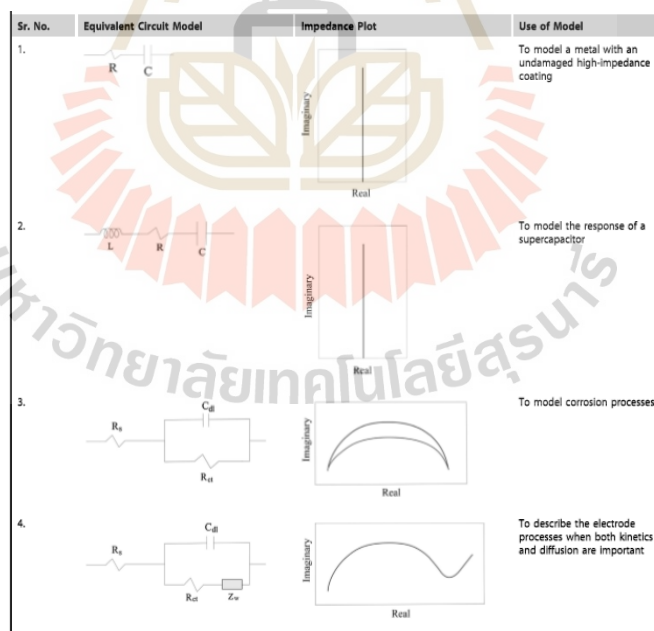


Figure 2.32 Basic Equivalent Circuit Models and Their Corresponding Impedance Plots.

The CV experiment can be performed with a single cycle or with numerous cycles of varying voltage. The scan rate is defined as the slope of the ramp signal in volts per unit time. This scan rate can vary from a few hundredths of a millivolt per second to tens of thousands of volts per second. To better understand the electrochemistry cell, the scan rate can be adjusted. Therefore, the test sample's voltammetry behavior is highly dependent on the scan rate. It is reasonable to anticipate that the oxidation and reduction peak currents and peak potentials will vary with the scan rate. A good rate capability and improved pseudocapacitive behavior of the electrode material are both indicated by an increase in the peak current (faradaic current) with an increase in the scan rate. The presence of the electroactive species at the surface of the electrode (the working electrode) causes a greater number of redox reactions as the scan rate increases. However, if the scan rate is too slow, the products of the reduction or oxidation can take part in a chemical process whose products may not be electroactive, and the peak (either the forward or reverse scan peak) would be missed. It is possible to determine this peak current in the CV by utilizing the Randlese-Sevcik equation:

$$I_p = 2.69 \times 10^5 n^3 AC\sqrt{vD} \quad (2.5)$$

where  $I_p$  denotes the peak current,  $n$  refers to the number of electrons in the redox reaction,  $A$  indicates the area of the working electrode,  $C$  signifies the concentration of the electroactive species at the electrode,  $v$  represents the scan rate, and  $D$  denotes the diffusion coefficient of the electroactive species. Each of these factors is critical in establishing the peak current in CV.

Capacitance is measured at varying sweep speeds to provide a comprehensive picture of its behavior in the CV. In addition, the following formula can be used to estimate the material precise capacitance:

$$C_s = \frac{\int Idv}{vm\Delta V} \quad (2.6)$$

where  $\Delta V$  is the potential window (V),  $m$  is the mass of electroactive material (g),  $v$  is the scan rate (mV/s), and  $\int IdV$  is the area under the curve in the plot of  $I$  versus  $V$ .

A cyclic voltammogram involves regulating the voltage and monitoring the current. The potential for either growth or decay is linear. The scan rate  $v$  is the rate of change of the potential over time. Mathematically speaking, this corresponds to the slope of the linear potential (see equation 2.7).

$$V = \frac{\partial E}{\partial t} \quad (2.7)$$

Potentials at the outset are often inactive, meaning no electrochemical reaction is taking place. In most cases, the linear sweep of the potential will cross the formal potential of the species under study (Figure 2.32). After a certain threshold is crossed, the slope of the linear potential flips, such that a negative potential becomes a positive one and vice versa. The vertex potential is the name given to this potential. When the potential returns to its initial value, the cycle is complete.

This procedure may be repeated as often as desired. The purpose of performing several cycles is to gauge the robustness of a system. In most modern software, the potential sweeps between the two vertex potentials and begins at a potential between these two, with the opportunity to specify a start potential in between.

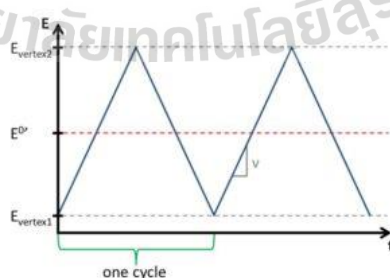


**Figure 2.33** The relationship between potential and time during cyclic voltammetry, with the vertex potentials ( $E_{\text{vertex}}$ ), the formal potential of the species being researched ( $E_0'$ ), and the scan rate ( $v$ ) highlight.

### 2.4.7.1 The shape of a cyclic voltammogram

An example CV for a solution with a single freely diffusing reversible species is shown in Figure 2.33. The peak data is read in the same way. The peak information includes the cathodic peak currents  $i_{p,c}$  and potential  $E_{p,c}$ , as well as the anodic peak current  $i_{p,a}$ . The arrangement of a curriculum vitae can provide a wealth of qualitative data. Either by analyzing the peaks themselves or by monitoring how they evolve over the course of a series of observations, more crucial information can be gleaned. Please be aware that it is more challenging to establish a baseline for the back scan because the current at the beginning of the back scan incorporates the diffusion-limited current of the forward scan. In this section of the guidelines, you'll find details on how to account for this circumstance. If the peak current is being monitored solely for quantitative analysis purposes, then the baseline offset is irrelevant.

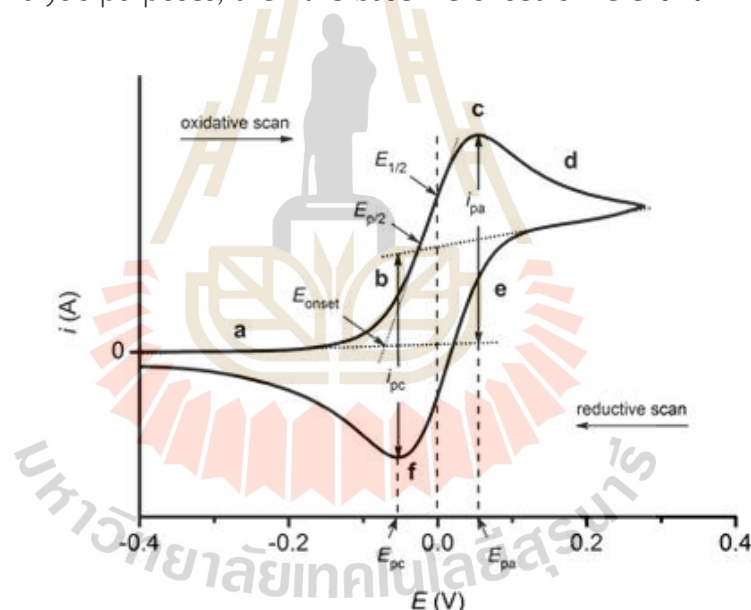


**Figure 2.34** The CV of a reversible species that diffuses easily, together with an indication of the anodic and cathodic maxima in current and potential, respectively.

## 2.3 Background of research

In the LIB industry, the first commercial lithium ion battery is  $\text{LiCoO}_2$ . It has good structural stability and high electrical conductivity. Nevertheless, the development of the  $\text{LiCoO}_2$  cathode was restricted by the toxicity and cost of cobalt.

Thus, using other transition metals like nickel or manganese to replace cobalt can solve these problems. Currently, Ni-rich  $\text{LiNi}_x\text{Mn}_y\text{Co}_z\text{O}_2$  (NMC) ( $x > y, z$ ) materials have become a popular cathode family due to their high theoretical capacity of around 275.5 mAh/g, low cost, and environmentally friendly nature. Nonetheless, there are several drawbacks for high-nickel NCM-based. For example, the large quantities of  $\text{Ni}^{2+}$  in NCM-based material may occupy the  $\text{Li}^+$  position and form a cation  $\text{Li}^+/\text{Ni}^{2+}$  mix, which results in the specific capacity of material being reduced. The higher nickel content produces worse thermal stability, causing safety issues (Zhang et al., 2019). Although the partial presence of Co can hinder the diffusion of  $\text{Ni}^{2+}$  into the Li layer by  $\text{Co}^{3+}$ , that makes the structure more stable. Moreover, Co can also enhance electric conductivity and promote high-rate capability. While a small quantity of Mn doping can enhance thermal stability. Since Mn ions suppress the irreversible side reactions between the electrolyte and the electrode surface, thus stabilizing the surface structure (Tsai et al., 2021). But it seems that these solutions are not enough for the development of high-nickel NCM material. Therefore, the remodeling of Ni-rich  $\text{LiNi}_x\text{Mn}_y\text{Co}_z\text{O}_2$  (NMC) ( $x > y, z$ ) into an amorphous material cathode by using  $\text{Li}_2\text{O}-\text{B}_2\text{O}_3$  glasses as base glass formers may cause novel cathode material for LIBs. Although there is no definitive research on the  $\text{Li}_2\text{O}-\text{B}_2\text{O}_3$  glasses doped with Ni-rich NMC material, but at least there is research showing that Ni-rich NMC material mixed with  $\text{Li}_2\text{O}-\text{B}_2\text{O}_3$  shows higher performance.

Recently, there have been interesting reports of modification in the efficiency of Ni-rich NMC cathode materials by coating with lithium-borates glasses ( $\text{Li}_2\text{O}-\text{B}_2\text{O}_3$ ). Jiujun Zhang and his group reported the results of improving the performance of  $\text{LiNi}_{0.8}\text{Co}_{0.1}\text{Mn}_{0.1}\text{O}_2$  (NCM811) Lithium Ion Batteries by surface-coating with a certain amount of material, which includes  $\text{Li}_2\text{O}-2\text{B}_2\text{O}_3$  glass. shown in Figure 2.35 and table 2.

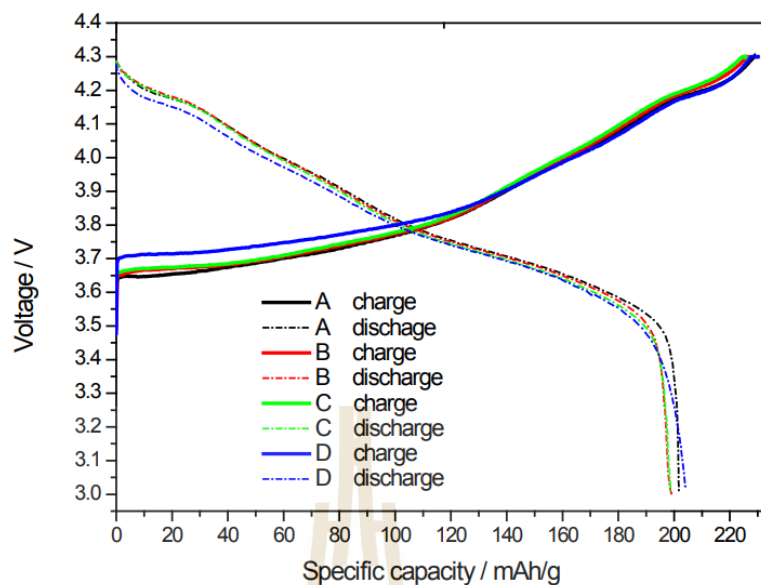


**Figure 2.35** The initial charge-discharge curves of NCM811 and NCM811 with various coatings (A, uncoated; B,  $\text{Al}_2\text{O}_3$ ; C,  $\text{ZrO}_2$ ; D, LBO) on both sides of the coin (Zhang et al., 2019).

It can be seen that NCM811 coated with  $\text{Li}_2\text{O}-2\text{B}_2\text{O}_3$  shows higher performance than uncoated,  $\text{Al}_2\text{O}_3$ -coated, and  $\text{ZrO}_2$ -coated. The first charge specific capacity of NCM811 coated with  $\text{Li}_2\text{O}-2\text{B}_2\text{O}_3$  is 230.0 mAh/g, the first discharge specific capacity is 204.3 mAh/g, and the first charge-discharge efficiency is 88.83%, respectively. These results are higher than those of both coated by  $\text{Al}_2\text{O}_3$  and  $\text{ZrO}_2$  (The first charge specific capacity, the first discharge specific capacity, and Coulomb efficiency Coulomb efficiency is 226.3 mAh/g, 199.2 mAh/g, 88.02%. mAh/g for  $\text{Al}_2\text{O}_3$  and 225.7 mAh/g, 198.7 mAh/g and 88.04% for  $\text{ZrO}_2$ , respectively (Zhang et al., 2019).

**Table 2.2** The initial charge and discharge capacities of the coin lithium-ion battery (LIB) using NCM811 and NCM811 coated with  $\text{Al}_2\text{O}_3$ ,  $\text{ZrO}_2$ , and LBO samples.

samples	Specific capacity	Specific capacity	Coulomb
	of first charge	of first discharge	efficiency
	mAh/g	mAh/g	%
A(bare)	229.2	201.7	88.00
B( $\text{Al}_2\text{O}_3$ )	226.3	199.2	88.02
C( $\text{ZrO}_2$ )	225.7	198.7	88.04
D(LBO)	230.0	204.3	88.83

Hyeong Seop Kang and colleagues have studied the electrochemical performance of the  $\text{Li}_2\text{O}-2\text{B}_2\text{O}_3$  coating on the  $\text{LiNi}_0.8\text{Co}_0.1\text{Mn}_0.1\text{O}_2$  cathode for Li-ion batteries. NCM811 was coated with  $\text{Li}_2\text{O}-2\text{B}_2\text{O}_3$  at different wt%, which caused the  $\text{Li}_2\text{O}-2\text{B}_2\text{O}_3$  glasses to have an unequal thickness. Figure 6 represents the cycling performance, rate capability, and the specific capacity vs. current density diagram of NCM811 coated with  $\text{Li}_2\text{O}-2\text{B}_2\text{O}_3$  at different wt%. It was clearly seen that the 1.0 wt%  $\text{Li}_2\text{O}-2\text{B}_2\text{O}_3@$ NCM811 has higher cyclic stability, specific capacity, and electrochemical performance when compared to other thicknesses. From the results, it can be confirmed that  $\text{Li}_2\text{O}-2\text{B}_2\text{O}_3$  glasses have the ability to optimize the electrochemical performance of Ni-rich NMC cathode (Hyeong et al., 2020).

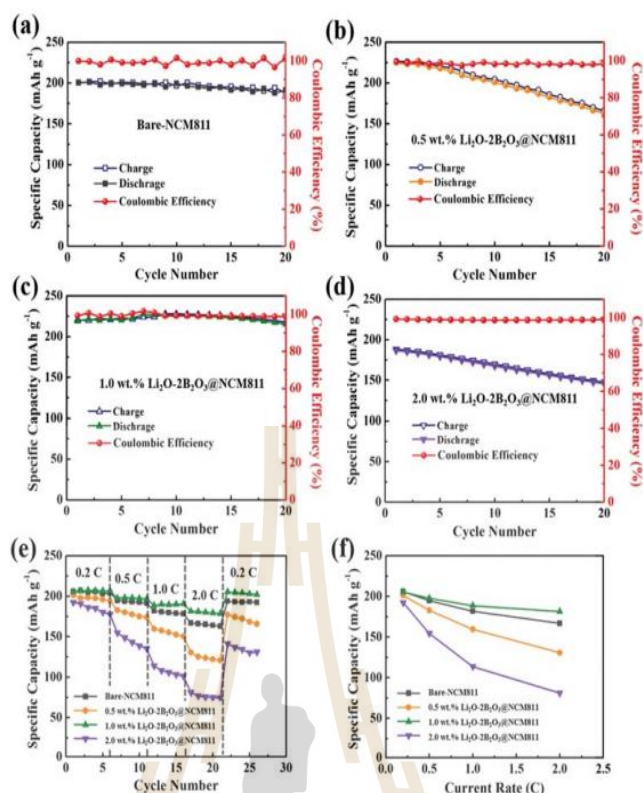
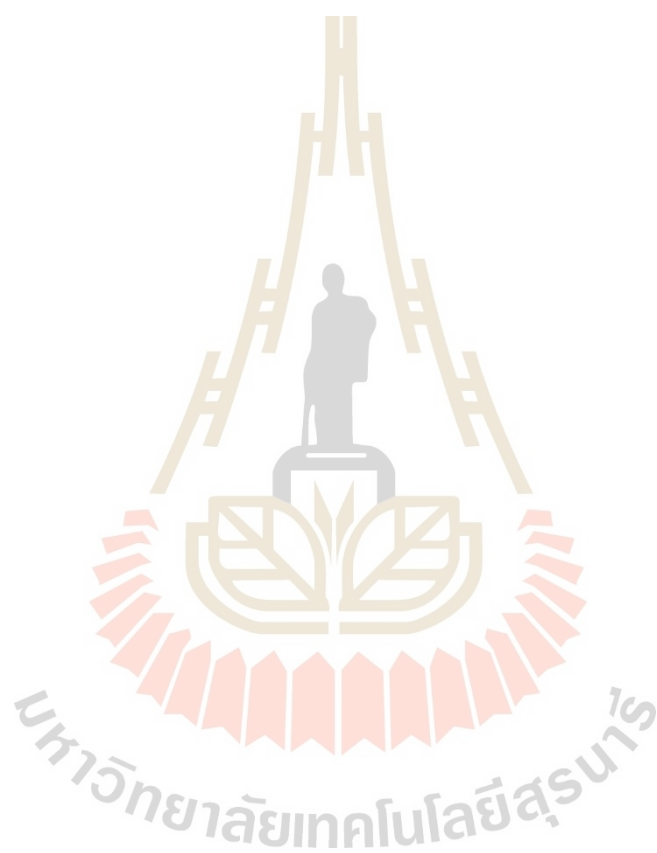


**Figure 2.36** (a)-(d) Cycling performance for bare and 0.5, 1.0, and 2 wt% of  $\text{Li}_2\text{O}-2\text{B}_2\text{O}_3$  glass ceramic oxide coated NCM811 materials at room temperature; (e) Rate capability for bare and 0.5, 1.0, and 2.0 wt% of  $\text{Li}_2\text{O}-2\text{B}_2\text{O}_3$  glass ceramic oxide coated NCM811 materials at different current rates; and (f) Specific capacity vs. current density diagram for bare and 0.5, 1.0, and 2.0 wt% of  $\text{Li}_2\text{O}-2\text{B}_2\text{O}_3$  glass ceramic oxide coated NCM811 materials at different current rates. (Hyeong et al., 2020).

This article highlights the noteworthy findings that the utilization of  $\text{Li}_2\text{O}-2\text{B}_2\text{O}_3$  can lead to substantial enhancements in both charge-discharge-specific capacity and Coulomb efficiency. By doing comparable studies, it is feasible to utilize nickel-rich lithium nickel manganese cobalt oxide (Ni-rich NMC) as a means to enhance the efficiency of lithium peroxide-borate ( $\text{Li}_2\text{O}-2\text{B}_2\text{O}_3$ ) systems. Nevertheless, there has been a lack of comprehensive research on the intricate details of lithium borate-based glasses that are doped with Ni-rich  $\text{Ni}_x\text{Mn}_y\text{Co}_z$  (NMC) materials, where  $x$  is greater than  $y$  and  $z$ . Given the absence of existing literature on the detailed characteristics of lithium-borate-based glass cathode materials incorporating Ni-rich NMC, this study aims

to investigate lithium-borate-based glass that is doped with nickel oxide and co-doped with nickel and other elements, such as manganese and cobalt. The objective is to gather a more thorough understanding of these materials.



## CHAPTER III

### EXPERIMENTAL

#### 3.1 Materials

In this work, various chemicals are employed in the fabrication of lithium-borate glass. This encompasses the processes of glass melting and crucible cleaning. There is a diverse array of materials that are used in the following manner:

- Boric acid ( $\text{H}_3\text{BO}_3$ )
- Lithium carbonate ( $\text{Li}_2\text{CO}_3$ )
- Nickel oxide ( $\text{NiO}$ ) purity 99%.
- Manganese dioxide ( $\text{MnO}_2$ ) purity 99%.
- Cobalt (II) oxide ( $\text{CoO}$ ) purity 99%.
- DI water
- Ethanol 99.99%
- Hydrofluoric acid (HF) 49%

#### 3.2 Glass preparation

Lithium-borate glasses doped with transition metal were prepared from high purity of starting materials of Lithium carbonate ( $\text{Li}_2\text{CO}_3$ ), Boric acid ( $\text{H}_3\text{BO}_3$ ), manganese dioxide ( $\text{MnO}_2$ ), Cobalt (II) oxide and Nickel oxide ( $\text{NiO}$ ). In this work, the glass was fabricated by the conventional melt quenching technique consisting of two-process.

Firstly, the lithium borate ( $\text{Li}_2\text{O}-\text{B}_2\text{O}_3$ ) preparation, the powders of  $\text{Li}_2\text{CO}_3$  and  $\text{H}_3\text{BO}_3$  weighted and combined in stoichiometric proportions in an agate mortar. Then, the mixtures were melted at  $1100^\circ\text{C}$  for 1 h in an electrical furnace. At room temperature, the molten liquid was swiftly poured out on a stainless-steel plate and pressed with another plate (RT).

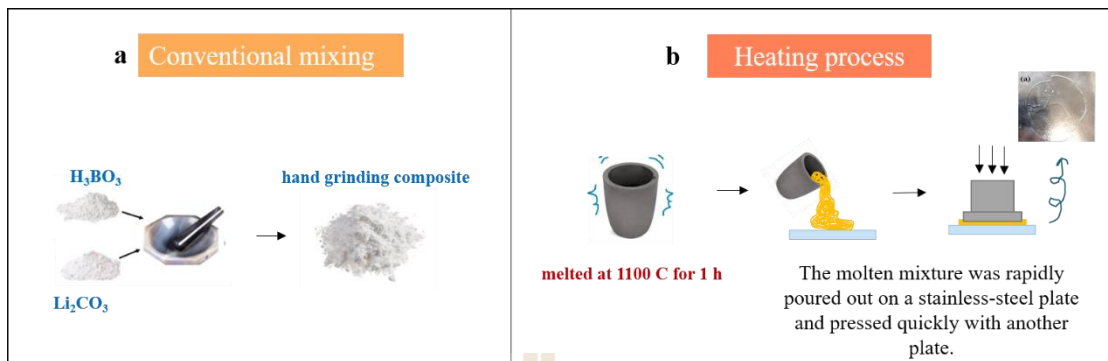


Figure 3.1 depicts the procedure followed for preparing Lithium-borate glass samples.

Second, The  $Li_2O-B_2O_3$  glasses were pulverized to obtain a fine powder, which was subsequently combined with transition metal elements. For single-dope  $xNiO - 0.8Li_2O - B_2O_3$  where  $x = 0.00, 0.15, 0.20, \text{ and } 0.25$ , for Co-dope  $xNiO - (0.2-x)MnO_2 - 0.8(Li_2BO_2)$  and  $xNiO - (0.2-x)CoO - 0.8(Li_2BO_2)$  where  $x = 0.1, 0.06, 0.05, 0.04$  and Triple-dope  $xNiO - yCoO - zMnO_2 - 0.8(Li_2BO_2)$  where ratio between  $x, y, z$  are 1:1:1, 2:1:1, 3:1:1 and 4:1:1, respectively. The homogenized powders of transition metal and  $LiBO_3$  fine glass were subsequently subjected to a melting process at a temperature of  $1150^\circ C$  for a duration of 1 hour. Following this, the resulting melts were rapidly cooled to room temperature. Ultimately, the acquisition of the transparent spectacles. was accomplished.

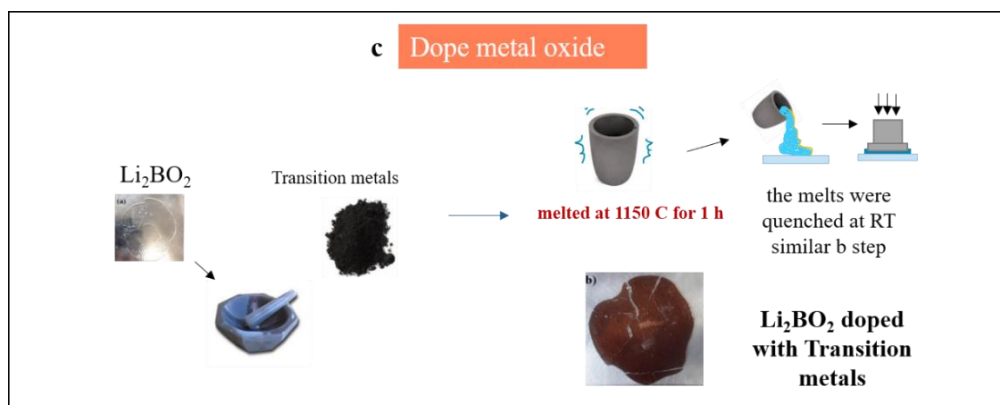


Figure 3.2 shows the process of incorporating a transition metal into a glass sample.

### 3.2.1 Characterization process

XRD was employed to characterize the glass samples, utilizing a Rigaku Smart Lab instrument equipped with a copper source (Cu K $\alpha$  = 1.542). The morphologies of the glass system were examined through the utilization of SEM and EDS employing the FEI quanta 450 instrument. These techniques were employed to verify the amorphous nature of the glass system. The local structure and the valence state information were collected in transmission mode by the XAS spectra including XANES and EXAFS spectra. Synchrotron based XAS technique, XANES and EXAFS were measured at the SUT-NANOTEC-SLRI XAS beamline (BL5.2) under the Synchrotron Light Research Institute (Public Organization), Thailand. The X-ray photoelectron spectroscopy (XPS) technique was used to derive the surface chemical composition of the obtained glasses. This technique is very surface sensitive for sample. XPS experiment was carried out at Beamline 5.3 of SLRI using a PHI 5000 with Probe II XPS system and the K-alpha X-rays of aluminum (Al K-alpha radiation) source.

### 3.2.2 Optical and magnetic properties

The absorbed signal was determined using UV-Vis spectroscopy, specifically employing the Perkin Elmer-Lambda 950 spectrophotometer. Davis and Mott (year) present the expression for the absorption coefficient,  $\alpha(\nu)$ , in terms of photon energy ( $h\nu$ ), for both direct and indirect optical transitions. The expression for  $\alpha(\nu)$  can be written as  $\alpha - E_{gopt}$ .  $E_{gopt}$  of the case of allowed direct transition, the exponent  $n$  is equal for  $an/2$ , while for allowed indirect transition, the exponent  $n$  is equal to 2. Here,  $E_{gopt}$  represents the Optical band gap energy. The objective is to graph the quantities  $(\alpha h\nu)^{1/2}$  and  $(\alpha h\nu)^2$  as a function of photon energy ( $h\nu$ ). The Quantum Design Versa lab instrument offers a vibrating sample magnetometer (VSM) feature, which allows for the measurement of magnetic properties. This VSM option has a specified applied magnetic field range of  $\pm 10$  kOe.

### 3.2.3 Electrochemical process

In order to prepare the glass electrodes, an agate mortar was used to mix an active material of (80 wt%) glass samples, (10 wt%) carbon black, and (10 wt%) polyvinylidene fluoride (PVDF) for the working electrode. The homogenies powder was

then mixed with N-methyl pyrrolidone solution (NMP) and ball milled for 24 hours. After that, The sample was deposited onto a nickel foam substrate measuring 1 × 1 cm and afterwards subjected to a drying process at a temperature of 70°C for a duration of 24 hours. The desiccated working electrodes were utilized for the quantification of electrochemical characteristics. The electrochemical performances were assessed by employing a potentiostat/galvanostatic (Metrohm Autolab) and employing cyclic voltammetry (CV) techniques. The specific capacitance ( $C_{cv}$ , F/g) was calculated from the results obtained from the CV curves plotted by using the following equations (Yan et al., 2012).

$$C_{cv} = \frac{1}{vm\Delta V} \int IdV \quad (3.1)$$

In this context,  $v$  represents the scan rates in millivolts per second (mV/s),  $I$  denotes the discharge current in amperes (A),  $m$  signifies the mass of the active material in grams (g), and  $\Delta V$  represents the operating voltage in volts (V).

### 3.3 Instrumentation

#### 3.3.1 Automated multipurpose XRD at SLRI

In this work, we have used X-ray diffraction from Rigaku Smart Lab. This X-ray diffraction system is made up of a Photon Max high-flux 9 kW rotating anode X-ray source and a HyPix-3000 high-energy resolution 2D multidimensional semiconductor detector that can measure in 0D, 1D, and 2D modes. This means that all applications can be handled by a single detector, and it is no longer necessary to prepare and switch detectors for each application. Using the HyPix-3000 detector, it can get 2D powder diffraction patterns. The in-plane diffraction arm is part of a system that also features a high-resolution, closed-loop goniometer drive mechanism. The new family of Cross-Beam-Optics (CBO) for the system are completely automated switchable optics that can reflect or transmit light (CBO-Auto).



Figure 3.3 SmartLab automated multipurpose XRD.

### 3.3.2 FEI Quanta 450 SEM at SLRI

This electron microscopy has a magnification of 6–1,000,000 times, making it possible to study structures as small as nanometers to micrometers. There is no need to put a conductive coating on a sample before taking a picture of it. For each type of sample, the right vacuum system is put in the sample chamber:

- High-vacuum system for solid, dry, and conductive samples such as metals, etc.

- Low-vacuum system for solid, dry, and non-conductive samples such as polymers, rubber, etc.

- Wet samples can be used with environmental vacuum systems (Environmental SEM) that can work at pressures between 10 and 2600 Pa. Contains water The humidity in the sampling chamber can be adjusted as required and can

measure low-temperature samples such as ice cream and frozen samples. Biological samples, medical, etc.

This instrument can measure in various modes. EDS is a piece of equipment that can look at elements from B (boron) to U (uranium) in samples and analyze the distribution of elements on the studied sample surface. Sample transformation study while adjusting the temperature: Have a high-temperature control type sampling stand from room temperature to 1400°C and a low-temperature sampling stand. Controllable in the -20 to 60°C range, video recording can be performed to monitor changes in the sample while adjusting to the desired temperature. Sample transformation study While tensioning, there is a set of mechanical analysis benches for samples with a tensile technique of 450 newtons, supporting a maximum sample size of 1x12x65 mm with a maximum strain travel of 31 mm, so it can shoot VDO to monitor changes in samples while applying tension.



**Figure 3.4** Scanning Electron Microscope QUANTA 450.

### 3.3.3 The Tecnai G2 20 S-TWIN TEM at SLRI

The Tecnai G2 20 S-TWIN Transmission Electron Microscope is intended to provide an imaging and analytical solution for use in the industries of life sciences, materials sciences, nanotechnology, semiconductor manufacturing, and data storage. The Tecnai G2 20 S-TWIN TEM supports a broad variety of applications and techniques, including, but not limited to, high contrast imaging, HR-TEM, SAED, CBED, EDX, and the use of embedded detectors and components like BF/DF, CCD, and corrected optics.



Figure 3.5 Tecnai G2 20 S-TWIN Transmission Electron Microscope.

### 3.3.4 Quantum Design VersaLab VSM at Khon Kaen University (KKU)

As a fast and sensitive DC magnetometer, the VersaLab VSM option is mostly made up of a linear motor transport (VSM head) for shaking the sample and a coil set for detecting (the pickup coil). The VSM head is located at the top of the instrument (pickup coil). The most fundamental method of measurement involves making synchronous detections of the voltage produced by oscillating the sample close to the pickup coil. The system can determine magnetization changes of less than 1 emu

with 1 s of data averaging using an oscillation amplitude of 1-3 mm at a frequency of 40 Hz. There are two types of coils available to accommodate a wide range of sample volumes: standard and large. In the case of planar samples (like a thin film on a substrate), it is feasible to take measurements in either the in-plane or the out-of-plane orientation (out-of-plane configuration only for large coil sets). The regular coil-set ball offers a good compromise between sensitivity and precision, making it the best option for most situations. As a result of the fact that the sensitivity is not substantially impacted by the presence of large magnetic fields, the VSM is able to carry out sensitive measurements up to a field strength of 3 T. For the VSM option, which requires a specialized sample holder and an oven kit to reach 1000 K, the VersaLab's normal working temperature range of 50–400 K is expanded to a maximum of 1300 K.



**Figure 3.6** Quantum Design VersaLab VSM.

### 3.3.5 Metrohm Autolab PGSTAT302N beamline 2.2 at SLRI

This device is made for electrochemical impedance spectroscopy. Its main instrument is a potentiostat or galvanostat with a compliance voltage of 30 V and a bandwidth of 1 MHz. With a highest current of 2 A, a current range of up to 20 A with the booster 20 A, and a current resolution of 30 fA at a current range of 10 nA. Autolab add-ons and external devices can be managed via analog and digital inputs and outputs, respectively. It has an analog integrator built right in. When coupled with the NOVA program, it can perform the majority of the common electrochemical procedures.

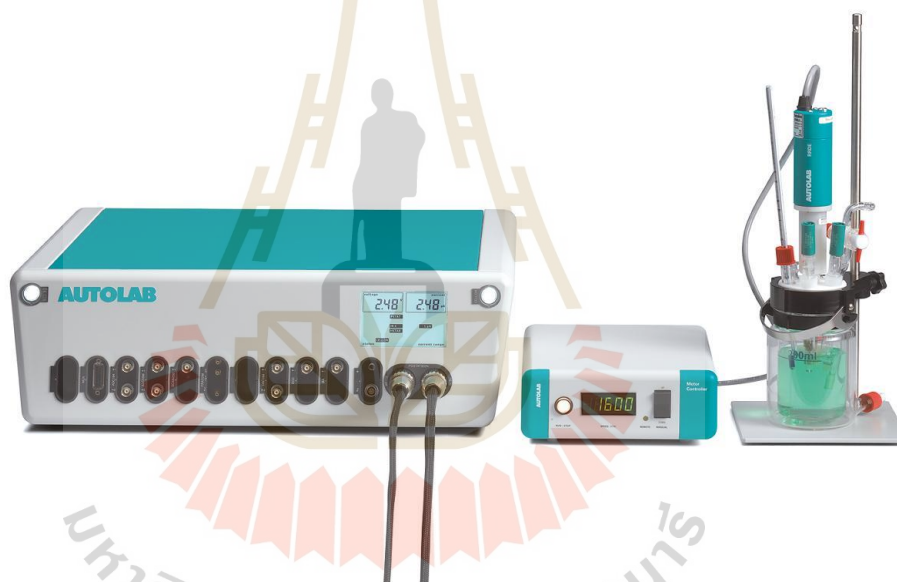


Figure 3.7 Metrohm Autolab PGSTAT302N at SLRI.

### 3.3.6 SUT-NANOTEC-SLRI XAS beamline5.2 at SLRI

XAS is the only focus of the SUT-NANOTEC-BL5.2 SLRI beamline. Chemical speciation and local structure (number of coordination complexes, inter-atomic distance, etc.) can both be determined with this method. XAS is a non-destructive technique that can be applied to any solid (crystalline or amorphous), liquid, or gas (pressure and temperature control) outside of ambient conditions. Real-world samples from fields as varied as materials science, biology, environmental science, archaeology,

and geology can all be studied with this method. To detect and quantify S species in difficult materials such as minerals, coals, sediments, and rubber, XANES spectroscopy is an excellent, non-destructive option. Materials in this category include minerals, coals, sediments, and even rubber. Differences in the S-K apex and XANES bands can oxidize sulfur compounds in either an inorganic or organic form. Like fingerprints, XANES bands can provide insight about a substance's coordination chemistry. The fundamental idea of both BL5.2 and BL8 is the same. It relies heavily on an in-house-built double-crystal monochromator (DCM) with a fixed outlet. To adjust the level of x-ray radiation, a DCM equipped with a wide range of crystals, from 1240 eV to 12100 eV, is employed. All the way from magnesium to gallium, you can do K-edge absorption tests. The L and M limits are useful for studying heavier atomic species.

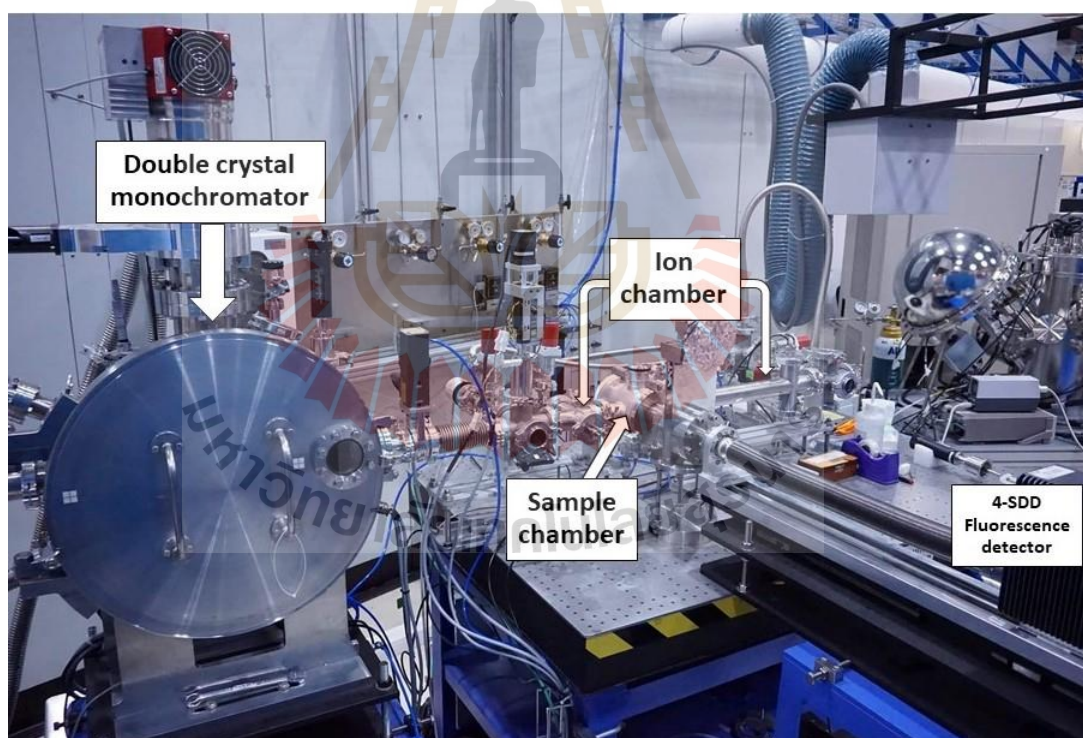
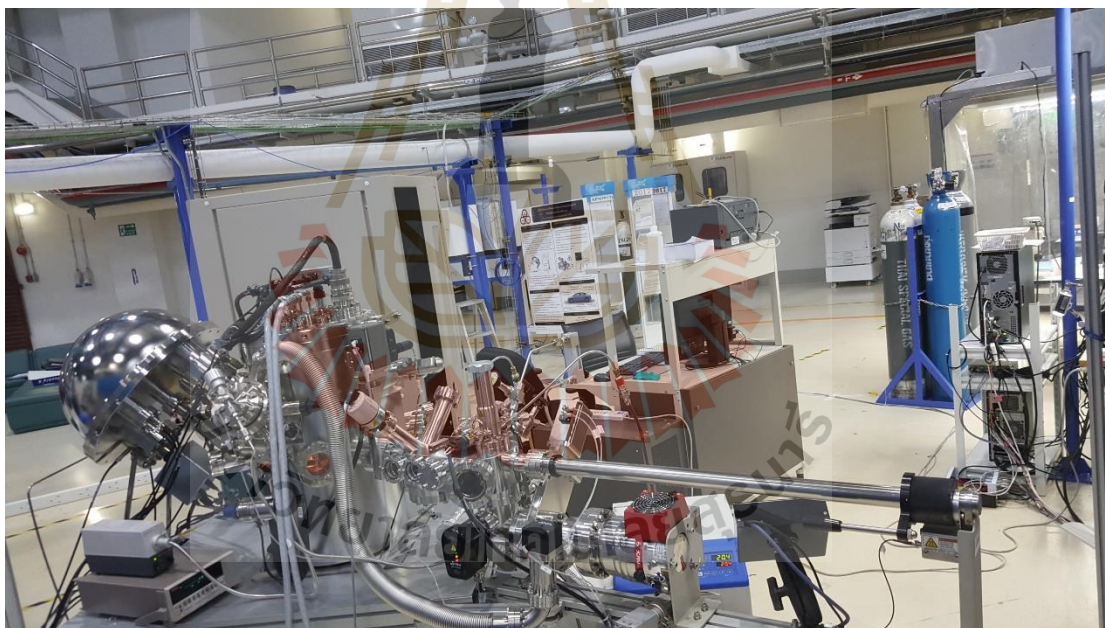


Figure 3.8 BL5.2 : SUT-NANOTEC-SLRI XAS Beamline.

### 3.2.7 PHI 5000 Versaprobe-II Focus XPS beamline 3.3 at SLRI

The PHI 5000 Versaprobe-II Focus XPS is made up of a scanning X-ray beam source, a focusing micro-monochrome, a 20 kV electron gun, and a floating argon ion gun. The X-rays are collected, filtered, and refocused onto the sample surface by an elliptical quartz monochromator, which can then be used for scanning and getting spectra. It uses a Zalar spin that is computer-controlled. capability for depth profiling via sputtering (5 V to 5000).

For XPS, X-ray beam sizes can be anywhere from 9 to 200 nanometers, while AES scans at 100 nm. SEM and Secondary X-ray Imaging (SXI) can also be used to figure out what elements are in something and what chemicals are in it, respectively.



**Figure 3.9** PHI 5000 Versaprobe-II Focus XPS beamline 3.3 at SLRI.

## CHAPTER IV

### RESULTS AND DISCUSSIONS

This chapter discusses the characterization and electrochemical properties of lithium borate-based glasses that have been doped with transition metals (Ni, Co, and Mn). The preparation of all glass samples involves melt quenching, and they all have different characteristics. X-ray diffraction (XRD) studies of the morphologies of the glass system demonstrated their amorphous nature. To find out about the valence state and the local structure, X-ray absorption near edge structure (XANES) and X-ray photoelectron spectroscopy (XPS) were used. Electrochemical performance was evaluated using cyclic voltammetry (CV) techniques, with a potentiostat/galvanostat (Metrohm Autolab) to quantify glass electrode electrochemistry.

#### 4.1 Single Doping

##### 4.1.1 Physical characteristics

Figure 4.1 presents the visual representation of the physical surface of the LiBO<sub>3</sub> glass samples, which have been doped with different concentrations of NiO (xNi: LiBO<sub>3</sub> glass, where x = 0, 0.15, 0.20, and 0.25). All prepared glasses after calcination showed a dense, transparent, and smooth surface structure with a brown color. Its hue originates from nickel doping.

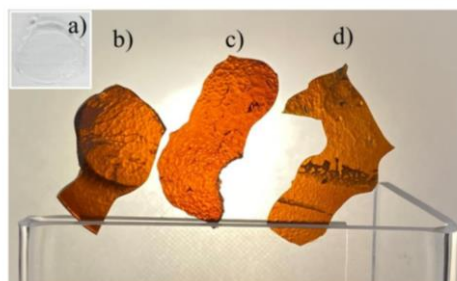


**Figure 4.1** Prepared xNi: LiBO<sub>3</sub> plate glasses where x = 0 (a), 0.15 (b), 0.20 (c) and 0.25 (d).

#### 4.1.2 Phase identification

Our goal in this study is to create a borate glass cathode for use in rechargeable batteries. The amorphous structure has the possibility of yielding a more effective cathode as a result of its unique features. In this study, we sought to synthesize samples with the most amorphous, glass-like, or least crystalline structure possible. Thus, the XRD method was applied in this situation so that the structure of the sample morphology could be verified. XRD pattern is the result of the combined efforts of all the individual phases. Periodically organized in three-dimensional space is what makes up a crystal. However, atoms in amorphous materials are dispersed randomly over three dimensions; therefore, they lack pattern. In that particular situation, the important thing to take into consideration is how atoms scatter X-rays. If the atoms are arranged in a periodic pattern, then the X-rays will scatter in only specific directions when they reach the lattice planes. Extreme peaks in intensity will result (the width of the peaks will be determined by other factors). Thus, in the amorphous phase, X-rays scatter in numerous directions, producing a broad, uneven peak (2 Theta) rather than sharp, concentrated peaks due to their high intensity. Figure 4.2 displays the XRD analytical data for the single-dope of  $\text{LiBO}_3$  glass samples were doped with varying concentrations of NiO, which exhibit huge broad peaks. This points to the fact that this sample has a rather amorphous structure.

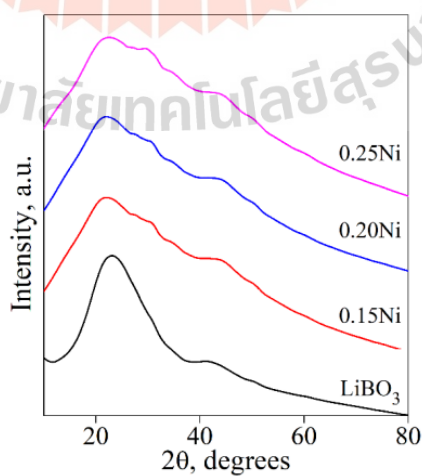


**Figure 4.2** XRD patterns of the xNi:  $\text{LiBO}_3$  glass system are being investigated, where x represents the varying compositions of 0, 0.15, 0.20, and 0.25.

Moreover, TEM technique was used to further identify the amorphous phase of glasses. Illustrated in Figure 4.3, the patterns are not available for any reflection. It can be confirmed that the prepared samples are amorphous (glass) materials. Figure 3 illustrates the bright field TEM technique performed to further identify the amorphous phase of glasses. There are also no reflection patterns as in the TEM image. The energy dispersive x-ray (EDS) technology was used to identify the components in the glass sample, which consists of boron (B), nickel (Ni), and oxygen (O), and the composition (wt%) is also shown in Figure 4.4.

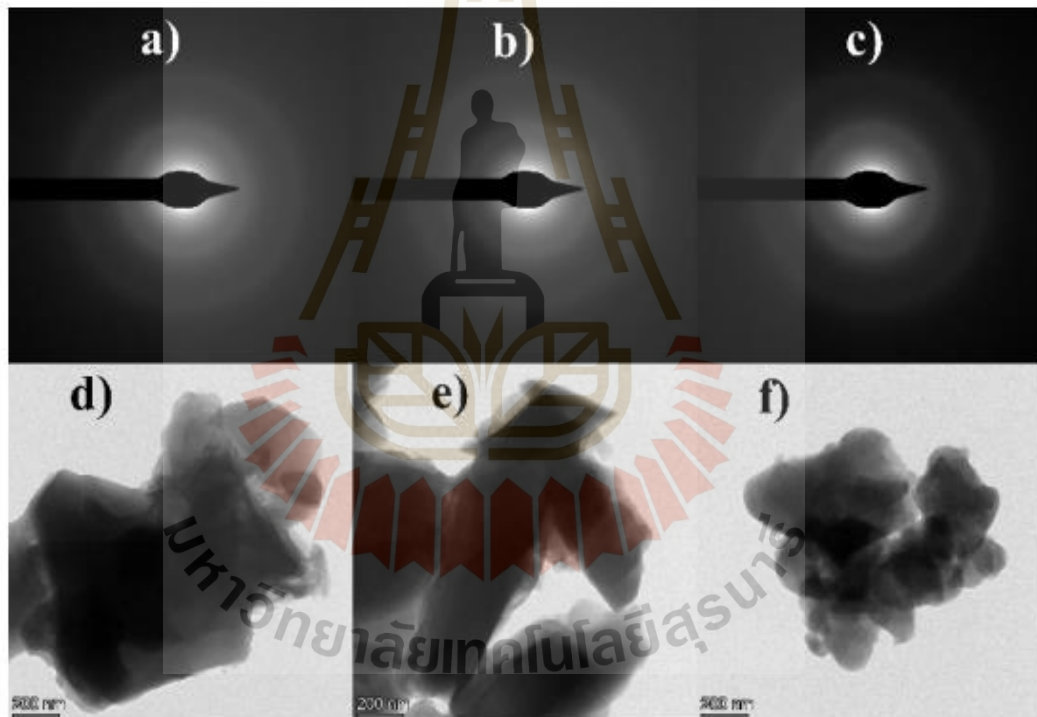


**Figure 4.3** TEM image and electron diffraction of  $x\text{Ni}:\text{LiBO}_3$  glass system where a,d)  $x = 0.15$ , b,e)  $x = 0.20$  and c,f)  $x = 0.25$

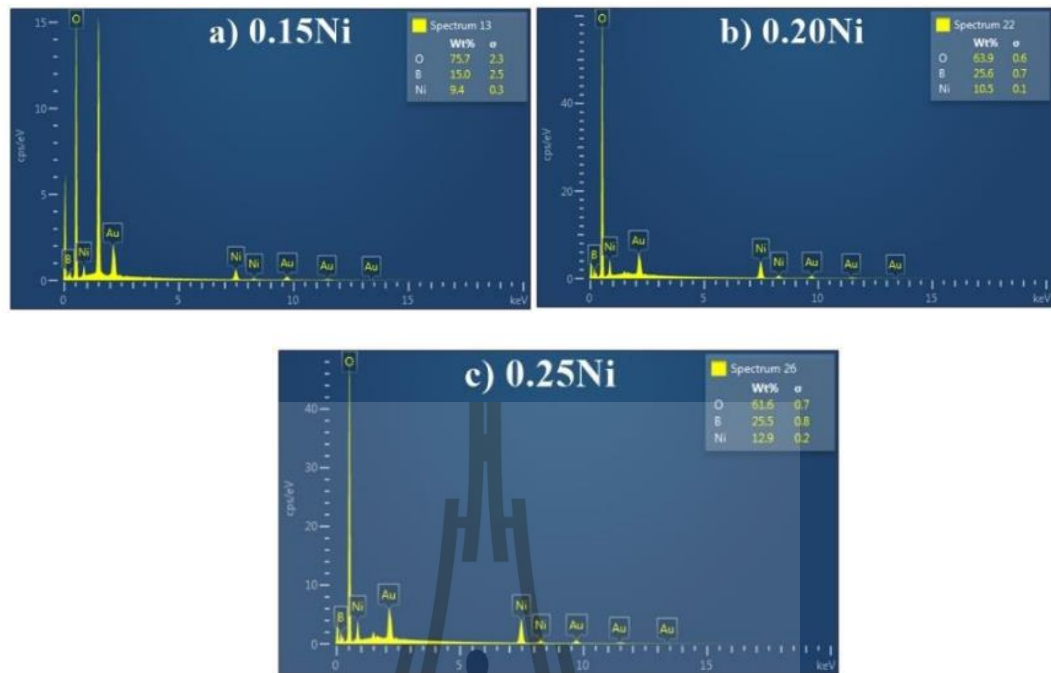


**Figure 4.4** EDS spectra of xNi: LiBO<sub>3</sub> glass system where a) x = 0.15, b) x = 0.20 and c) x = 0.25.

#### 4.1.3 Optical gap energy analysis

The use of UV-Vis spectroscopy is ubiquitous because of its many practical applications. When combined with mass spectroscopy, it becomes an even more potent instrument for calculating reaction rates and keeping tabs on many wavelengths simultaneously. One of the uses of UV-Vis in chemical engineering is the estimation of ion concentrations using Beer-Lambert's equation. For the UV-vis absorption spectra, xNi:LiBO<sub>3</sub> glass is a good approach utilized for the optical study of induced transitions. This consists of the band structure and the energy band gaps. As can be seen in Figure 8a-c, the absorption spectra were analyzed from a wavelength range of 200 to 800 nm. The absorption patterns of Ni-doped materials tend to seem very similar to one another. There are three distinct bands where absorption peaks occur: between 200 and 350 nm (band 1), between 350 and 600 nm (band 2), and between 600 and 800 nm (band 3). O<sup>2-</sup>-Ni<sup>2+</sup> charge transfer is responsible for the intense band at 220 nm,

whereas  $\text{Ni}^{2+}$  in octahedral coordination is responsible for the second zone at 430 nm, which corresponds to the  ${}^3\text{A}_{2g}(\text{F}) \rightarrow {}^3\text{T}_{1g}(\text{P})$  transition of  $\text{Ni}^{2+}$ . The  ${}^3\text{A}_{2g}(\text{F})$  and  ${}^3\text{T}_{1g}(\text{F})$  were displayed in the third spatial region.

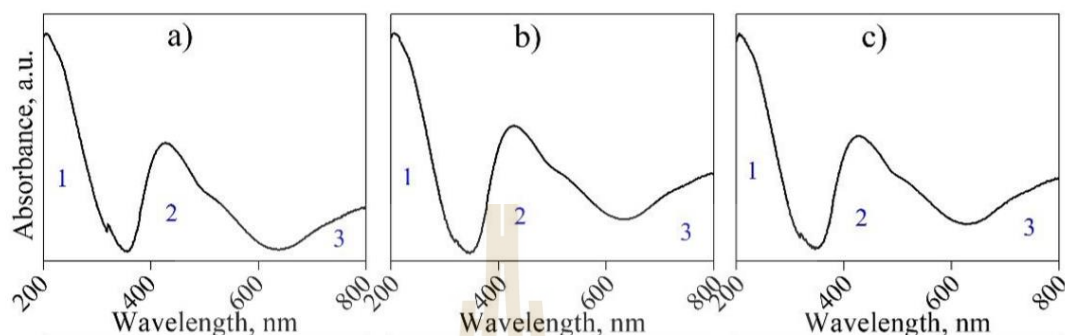


**Figure 4.5** Absorbance spectra of the optical variety for the  $x\text{Ni}:\text{LiBO}_3$  glass system for (a), (b), and (c)  $x = 0.15, 0.20,$  and  $0.25,$  respectively.

#### 4.1.4 XPS and XANES analyses

Electrochemical processes include the transfer of electrons from one chemical to another through an oxidation-reduction (redox) reaction. Therefore, understanding the oxidation state is crucial to explaining the shift in electrochemical charge that occurs when glass is doped with transition metals. Typically, the XPS binding energy measurements will be affected by the chemistry of the sample surrounding the atoms. By comparing the binding energy positions of the measured spectra to those in the published literature, the oxidation state of any element or ion can be determined via XPS. Similarly, XAS or XANES, is a powerful technique for investigating the oxidation state, which is closely related to the charge density of metals. Therefore, all glass samples were analyzed using these two methods to determine their oxidation levels.

The XPS technique was employed to confirm the existence of nickel (Ni) ions in lithium borate ( $\text{LiBO}_3$ ) glass samples and ascertain their oxidation status. XPS data depicted in Figure 4.6 illustrates the core level spectra of Ni 2p at energy values of 854, 856, and 861 electron volts (eV). The aforementioned energy levels are

representative of the peaks associated with  $\text{Ni}^{2+}$ ,  $\text{Ni}^{3+}$ , and Ni satellite. XPS results provide unequivocal evidence of a reduction in the concentration of  $\text{Ni}^{2+}$  ions as the amount of nickel (Ni) in the lithium borate ( $\text{LiBO}_3$ ) glass increased. The reconfirmation of Ni doping will be carried out in XANES analysis region.

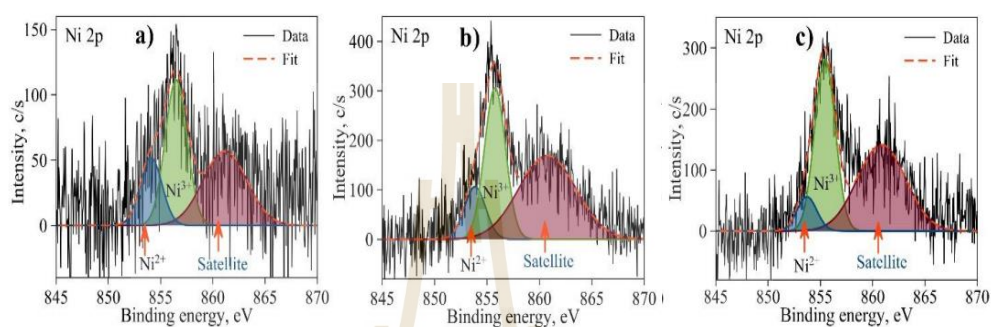


**Figure 4.6** XPS spectra for three different  $x\text{Ni}:\text{LiBO}_3$  glass samples, namely (a)  $x = 0.15$ , (b)  $x = 0.20$ , and (c)  $x = 0.25$ .

The XAS technique was employed to validate the oxidation state of nickel (Ni) ions in  $x\text{Ni}:\text{LiBO}_3$  glass where  $x = 0, 0.15, 0.20$ , and  $0.25$ . Normalized XANES spectra at Ni K-edge of all samples, which are compared with NiO as standard spectra are displayed in Figure 4.7. Initially, the Ni K-edge spectra of all samples exhibited a fine structure that closely resembled that of the standard NiO. Nevertheless, it is worth noting that the location of the  $1s \rightarrow 4p$  peak in all samples exhibits a displacement towards higher values compared to the NiO standard. This observation suggests a disparity in the oxidation state of nickel, namely a combination of  $\text{Ni}^{2+}$  and oxidation states higher than  $2+$ . Moreover, An observable phenomenon is the movement of the white line (WL) position towards higher energy (specifically, from peak  $1s$  to  $4p$ ) as the level of NiO doping increases from  $0.15\text{Ni}$  to  $0.25\text{Ni}$ . This shift provides confirmation of the alteration in the electronic structures of Ni ions in glasses that occurs with increased NiO doping. Based on the preceding XPS findings, it can be inferred that the composition of these glasses encompasses a combination of  $\text{Ni}^{2+}$  and  $\text{Ni}^{3+}$  ions.

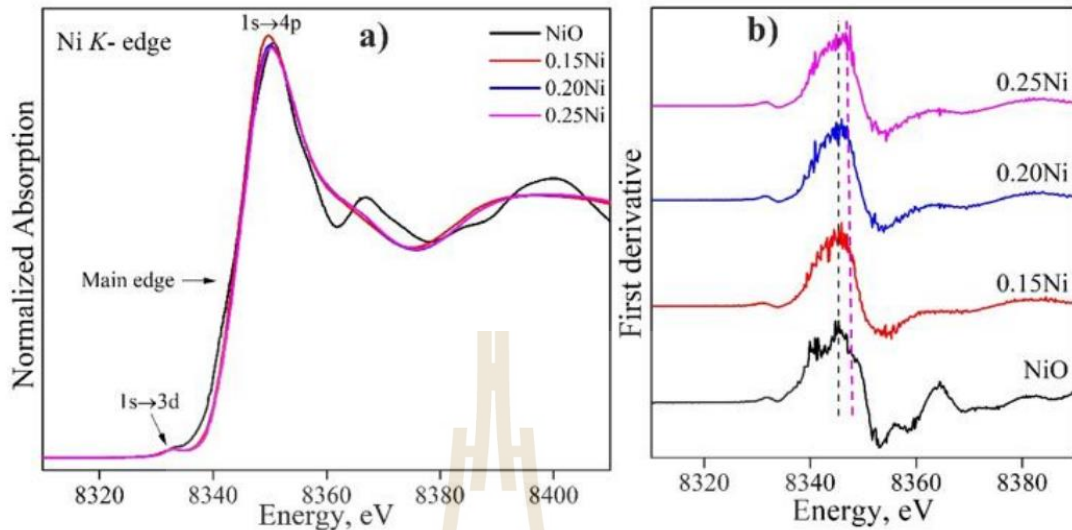


**Figure 4.7** XANES spectra for a) the nickel (Ni) K-edge and b) the first derivative of the Ni K-edge of a glass system consisting of  $\text{LiBO}_3$  doped with varying concentrations of NiO ( $x = 0.15, 0.20,$  and  $0.25$ ).

#### 4.1.5 Magnetic property

The magnetization curves of the  $x\text{Ni}:\text{LiBO}_3$  glass samples (where  $x = 0, 0.15, 0.20$  and  $0.25$ ) measured at room temperature with applied fields ranging from  $-10$  kOe to  $10$  kOe are illustrated in Figure 4.8. The M-H loops revealed the presence of a transitional phase between paramagnetic and soft ferromagnetic activity with clearly characterized magnetic anisotropy. The tendency toward saturation magnetization grows with increasing Ni concentration. The M-H loops have been shown to constantly rely on metal doping, even when the host matrix is the same and the metal additive is different. It was observed that higher magnetic fields were found to grow in correlation with rising nickel concentrations. This implies that the differences in magnetic properties are indicative of variances in the electrochemical behavior exhibited by these glasses.

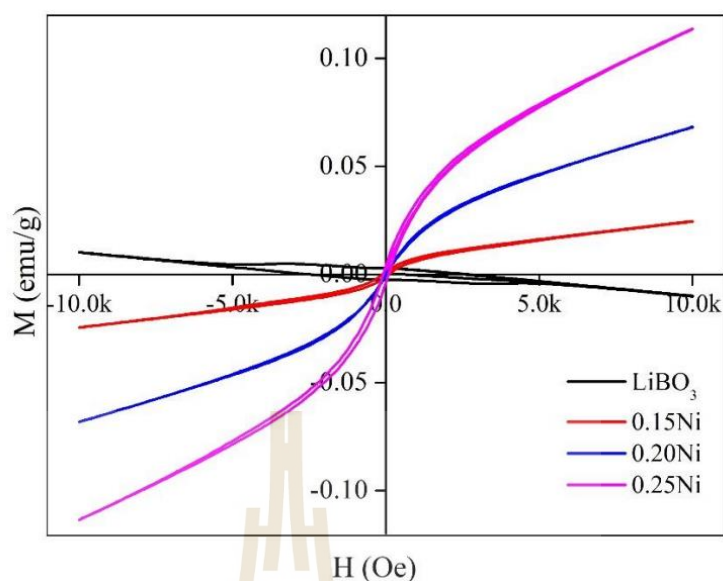


**Figure 4.8** The present study investigates the relationship between magnetization (M) and magnetic field (H) in the  $x\text{Ni}:\text{LiBO}_3$  glass system.

#### 4.1.6 Electrochemical properties

The electrodes that were constructed were evaluated in a 6 M KOH electrolyte using CV mode at various voltage scan rates of 5, 10, 20, 50, and 100 mV/s. This experimental setup is depicted in Figure 4.9. CV curves have non-rectangular shapes and display shifts in the redox peaks as the scan rates are raised. The curves show a pair of anodic and cathodic peaks arising from the fast-faradaic redox reactions of  $\text{Ni}^{2+}$  and  $\text{Ni}^{3+}$  during charge and discharge. The position of anodic and cathodic peaks was shifted when a scan rate increased. The results of this study exhibit exceptional high-rate performance and favorable electrochemical reversibility. The area capacitances of the  $x\text{Ni}:\text{LiBO}_3$  glass electrodes, namely 0.15Ni, 0.20Ni, and 0.25Ni electrodes, were determined by analyzing the area under CV curve at different scan rates ranging from 5 to 200 mV/s. It was observed that the specific area capacitances of these electrodes dropped as the scan rate increased. However, At low scan rates (5 mV/s), The specific capacity increases with the amount of NiO added to the glass sample, The

experimental findings yielded the following values: 5.34, 40.14, 90.01, and 91.06 F/g for the electrodes composed of 0.15Ni, 0.20Ni, and 0.25Ni, respectively.

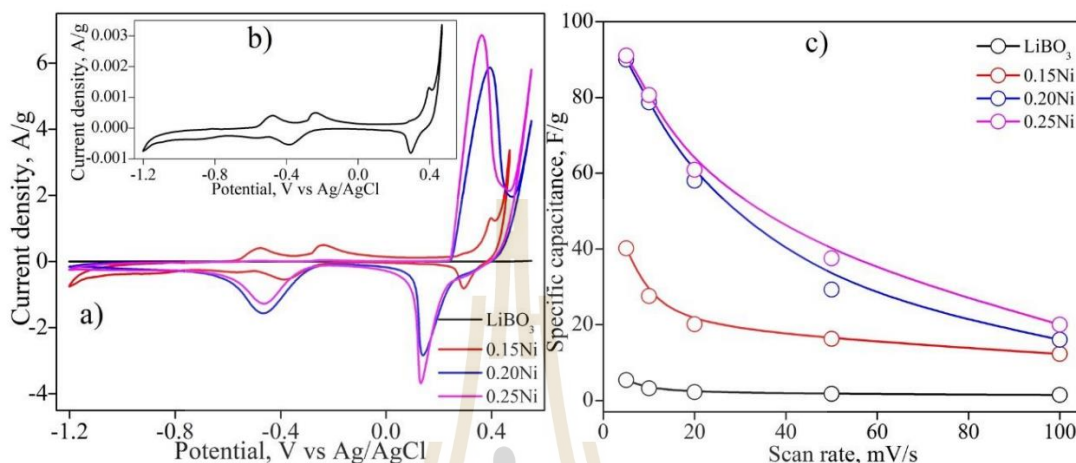


**Figure 4.9** a) CV analysis on the xNi:LiBO<sub>3</sub> glass system using a scan rate of 5 mV/s b) The LiBO<sub>3</sub>-based glass system with scan rates of 5 mV/s; c) A graphical representation illustrates the relationship between specific capacitance and scan rates.

## 4.2 Co-Doping

### 4.2.1 Physical characteristics

In contrast, the co-dope samples had a distinct hue. The first samples in this series are the LiBO<sub>3</sub> glass-doped nickel-manganese displays in Figure 4.10. The glass samples have a glossy, smooth surface; their hue and transparency are also similar to those of the single-doped sample, but their grain is significantly darker. The cobalt and nickel containing LiBO<sub>3</sub> glass samples in the second group (shown in Figure 4.11) appear opaque due to their smooth, shiny surfaces and deep, dark purple colors. This is the normal hue of glass after cobalt has been added.

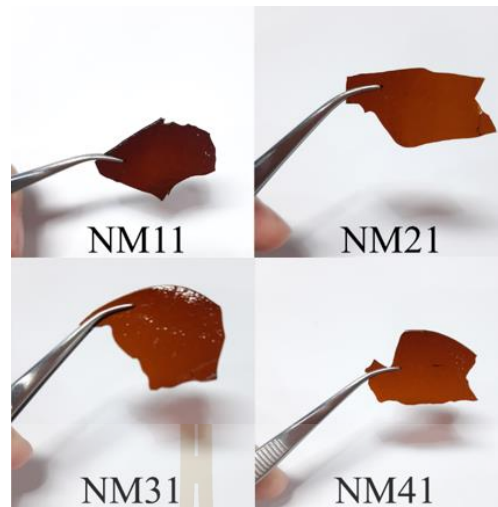


Figure 4.10 Prepared  $x\text{Ni}y\text{Mn}:\text{LiBO}_3$  plate glasses where  $y=1$  and  $x = 1, 2, 3$  and  $4$ .

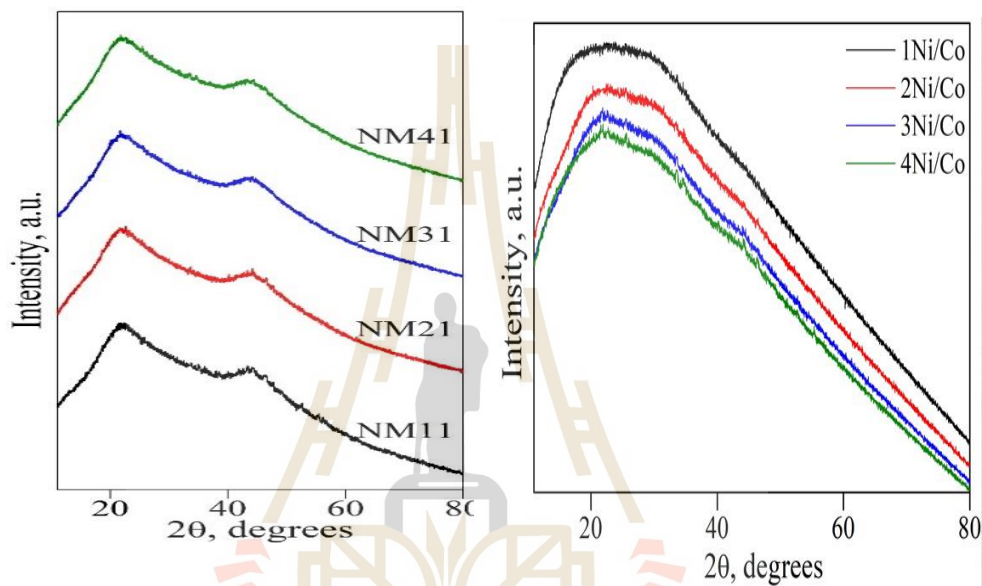


Figure 4.11 Prepared  $x\text{Ni}y\text{Co}:\text{LiBO}_3$  plate glasses where  $y=1$  and  $x = 1, 2, 3$  and  $4$ .

#### 4.2.2 Phase identification

Samples from the second group, the co-dope group, had lithium borate that had been doped with nickel manganese and nickel cobalt, and their XRD patterns all shared a similar peak feature, a large broad peak (Figure 4.12). Hence, it can be

observed that all the samples within the co-dope group exhibit amorphous phases. Lithium-borate-doped nickel manganese, on the other hand, exhibits two huge peaks in the sample set, whereas the amorphous phase will only show its greatest peak. It is possible to make out a second lithium peak if it is equally prominent, although it will not be as distinct.



**Figure 4.12** XRD patterns of lithium borate glass system that had been doped with nickel manganese and nickel cobalt.

Additionally, the TEM technique was employed to further characterize the amorphous phase of the  $x\text{Ni}_y\text{Mn}:\text{LiBO}_3$  glass system, where  $X = 1, 2, 3,$  and  $4$  and  $y = 1$ . As depicted in Figure 4.13, the patterns under consideration are not accessible for reflection. The amorphous (glass) nature of the produced samples has been verified. Figure 3 depicts the implementation of the bright-field TEM technique, which serves to enhance the identification of the amorphous phase in glasses. The identification of the components in the glass sample was facilitated by the utilization of an EDS picture. The components of  $x\text{Ni}_y\text{Co}:\text{LiBO}_3$  (with  $x$  values of  $1, 2, 3, 4,$  and  $y$  values of  $1$ ) were found to include boron (B), nickel (Ni), cobalt (Co), and oxygen (O), as indicated by the

composition (wt%) depicted in Figure 4.14.

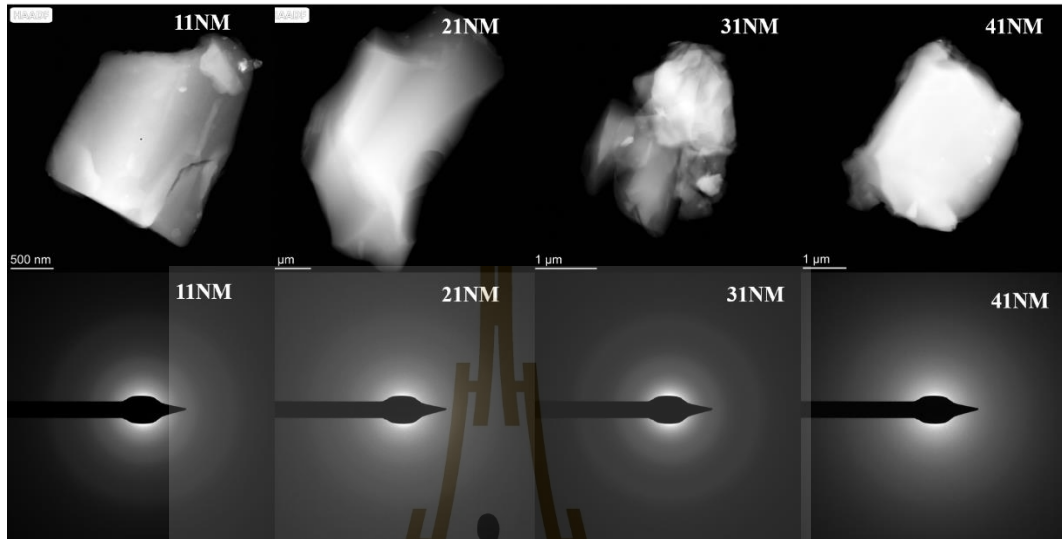


**Figure 4.13** TEM image and electron diffraction of  $x\text{NyMni}:\text{LiBO}_3$  glass system where  $X = 1, 2, 3$  and  $4$  and  $y = 1$ .

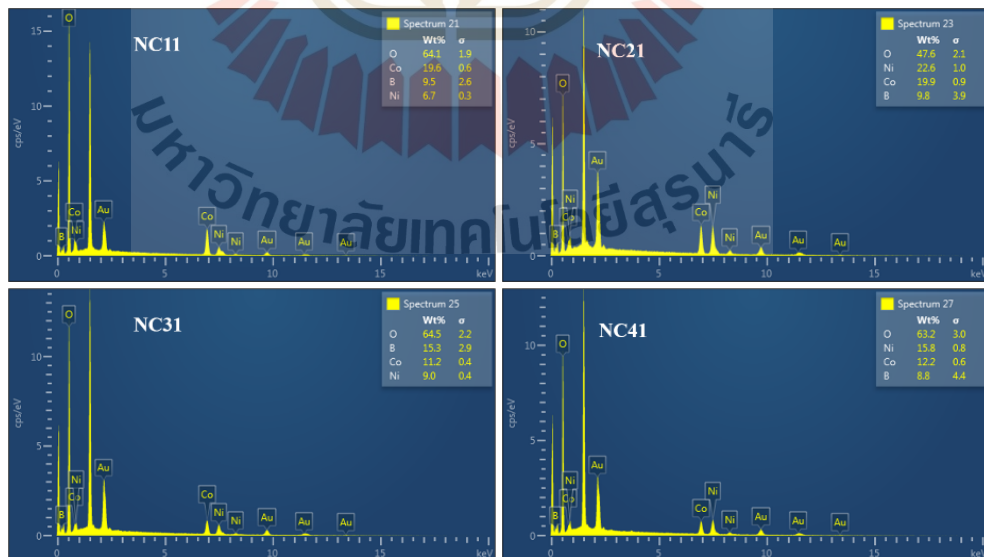


**Figure 4.14** EDS spectra of  $x\text{NiyCo}:\text{LiBO}_3$  (with  $x$  values of 1, 2, 3, 4, and  $y = 1$ ).

### 4.2.3 Optical gap energy analysis

The UV-vis spectrum of the  $x\text{Ni}_y\text{Co}:\text{LiBO}_3$  (with  $x$  values of 1, 2, 3, 4, and  $y = 1$ ) glass samples is shown in Figure 4.15. This shows how the Ni and Mn contents change. The absorption spectra were recorded at ambient temperature within the wavelength range of 200 to 800 nanometers. The absorption spectra of  $\text{Mn}_2\text{O}_3$  exhibit bands with a center wavelength ranging from 440 to 460 nm, which can be attributed to electronic transitions. On the other hand, bands centered at wavelengths between 575 and 700 nm characterize the electronic transitions seen in  $\text{MnO}$ . The d-d bands displayed by octahedrally coupled  $\text{Ni}^{2+}$  ions are responsible for the presence of another peak at around 720 nm (region 3). The absorption bands of all samples exhibit a consistent trend, with no significant change observed in the position of the peak. Absorbance bands with respective centers at 436 nm (region 1) and 530 nm (region 2) confirmed the existence of  $\text{Mn}^{2+}$  and  $\text{Mn}^{3+}$  ions. In addition, the presence of  $\text{Ni}^{2+}$  ions was detected in the glass samples through the observation of an absorption band with a wavelength of 729 nm.

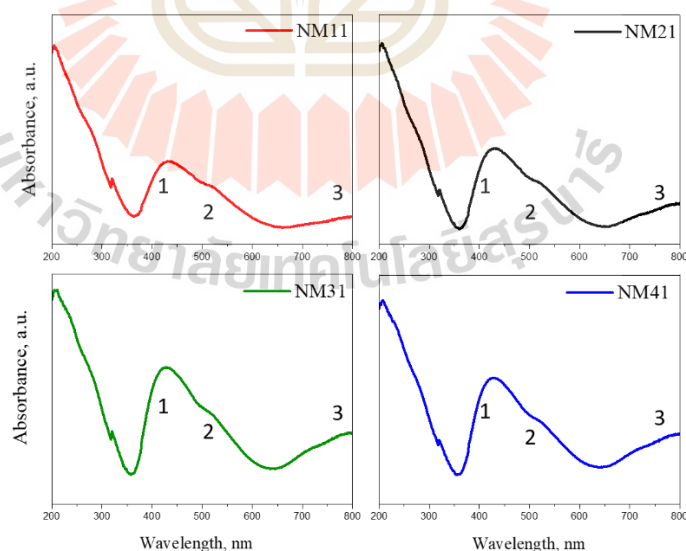


**Figure 4.15** Optical absorbance spectra of  $x\text{Ni}_y\text{Mn}:\text{LiBO}_3$  (with  $x$  values of 1, 2, 3, 4, and  $y$  values of 1).

In the instance of cobalt, a singular peak was detected in the acquired spectrum at a wavelength of 512 nm, which was identified as cobalt based on existing literature. This observation provides evidence for the presence of  $\text{Co}^{2+}$  ions. It was evident from the observations that the spectra at 512 nm exhibited a noticeable drop as the quantity of nickel in the glass sample increased. This observation suggests a variation in the concentration of  $\text{Co}^{2+}$  within the glass samples. The UV-Vis spectrum of the  $\text{Ni}^{2+}$  complex exhibited absorption peaks at wavelengths of 389nm and 645nm, which can be attributed to the  ${}^3\text{A}_{2g} \rightarrow {}^3\text{T}_{2g}$  and  ${}^3\text{A}_{2g} \rightarrow {}^3\text{T}_{1g}$  transitions, respectively. However, the oxidation states of Mn, Co, and Ni will be further verified through the analysis of XPS and XANES data in this study.

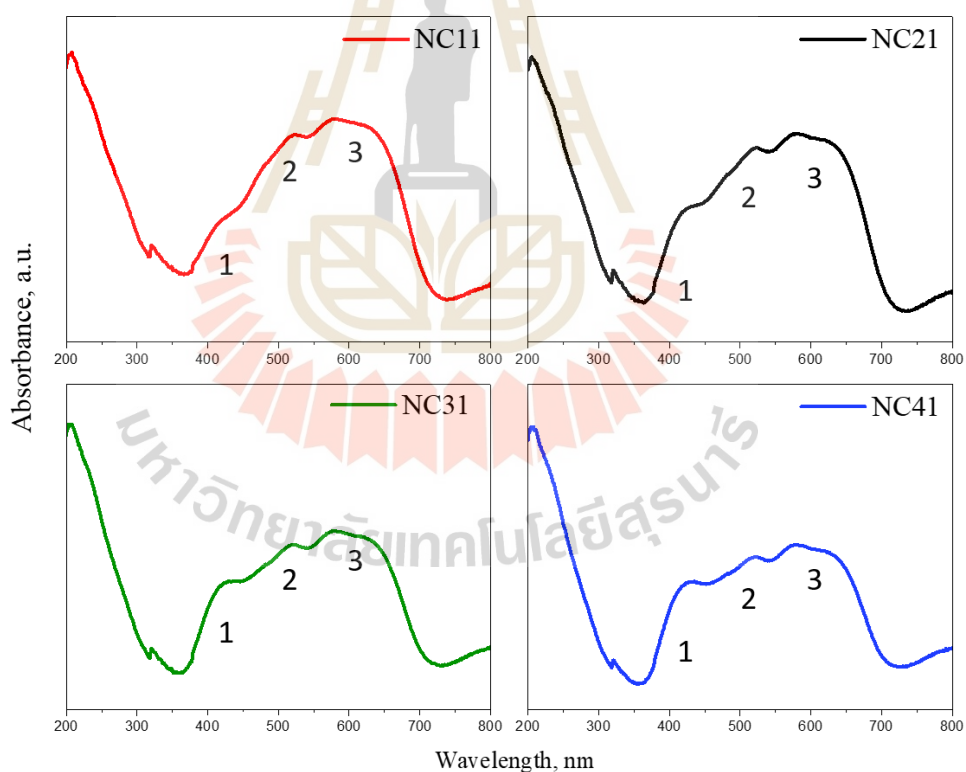


**Figure 4.16** Optical absorbance spectra of  $x\text{Ni}_y\text{Co}: \text{LiBO}_3$  (with  $x$  values of 1, 2, 3, 4, and  $y$  values of 1).

#### 4.2.4 XPS and XANES analyses

The XPS spectra of Ni 2p in glass sample  $x\text{Ni}y\text{Mn}:\text{LiBO}_3$  (where  $x = 1, 2, 3, 4$ , and  $y = 1$ ) have revealed that the sample contains  $\text{Ni}^{2+}$  and Ni satellite, which is used to analyze the oxidation state of the second set of samples (Co-Dope). When the nickel content reaches  $x = 4$ , the content of  $\text{Ni}^{2+}$  begins to drop, but at higher nickel concentrations,  $\text{Ni}^{2+}$  continues to rise. Even though the XPS data of Mn 2p showed similar trends, the concentration of  $\text{Mn}^{2+}$  and  $\text{Mn}^{3+}$  went up as the nickel ratio went up and went down as nickel was added, reaching peak ratios of  $x = 4$  and  $y = 1$ , with  $\text{Mn}^{2+}$ ,  $\text{Mn}^{3+}$ , and Mn satellite peaks at 640.7, 643.8, and 653.4 eV, respectively.

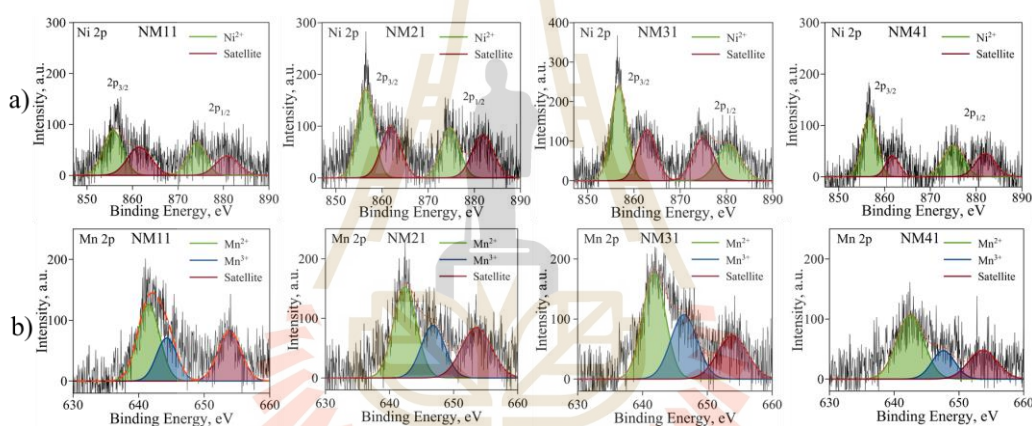


**Figure 4.17** XPS spectra were obtained for a series of  $\text{LiBO}_3$  glass samples containing  $x\text{Ni}y\text{Mn}$ , where  $y$  is fixed at 1 and  $x$  varies from 1 to 4.

In Figure 4.18, the normalized XANES spectra at the Ni K-edge of glass samples  $x\text{Ni}y\text{Mn}:\text{LiBO}_3$  (where  $x = 1, 2, 3, 4$ , and  $y = 1$ ) are shown. These spectra are compared with the standard materials for the oxidation of NiO. As compared to the NiO standard, the samples that were looked at show a clear shift in the location of the 1s-4p peak. This suggests that the oxidation state of nickel (a mix of  $\text{Ni}^{2+}$  and  $\text{Ni}^{3+}$ ) is changing. In the case of manganese, the two standard compounds are  $\text{MnO}$  and  $\text{Mn}_2\text{O}_3$ , with manganese occupied in the +2 and +3 valences, respectively. The increase in the

valence of manganese causes a shift in the positions of the absorption edges of manganese oxides to higher energy levels. The fact that the absorption edge position is between MnO and Mn<sub>2</sub>O<sub>3</sub> indicates that manganese ions have a mixed valence of +2 and +3. The position of the white line (WL) further reveals that the energy transition occurs between MnO and Mn<sub>2</sub>O<sub>3</sub>. This result agrees with the XPS result showing the presence of Mn<sup>2+</sup> and Mn<sup>3+</sup> in the sample.

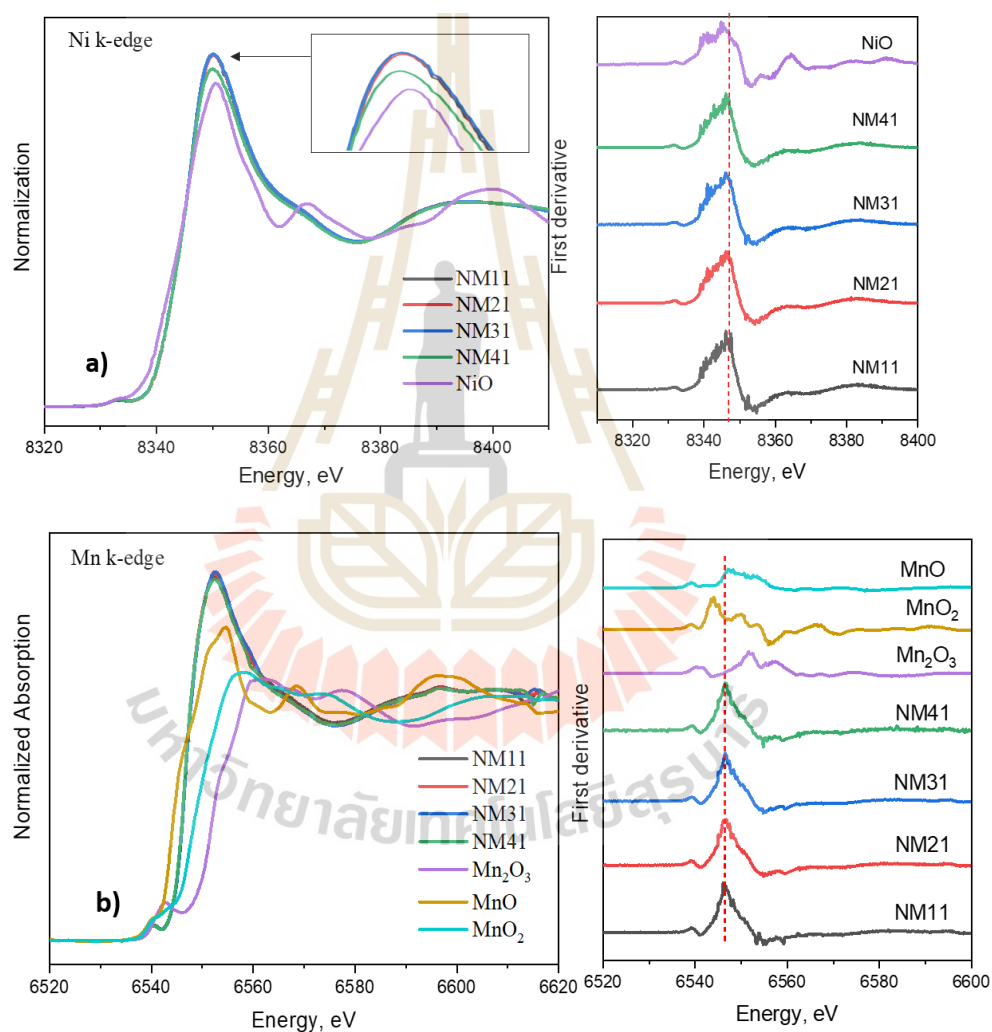


**Figure 4.18** XANES spectra of a) Ni K-edge and the first derivative of Ni K-edge; b) Investigation of the Mn K-edge and its first derivative in the LiBO<sub>3</sub> doped with NiMn glass system.

The XPS study of the Ni 2p spectra in the glass sample  $x\text{Ni}_y\text{Co}:\text{LiBO}_3$  (with  $x$  values of 1, 2, 3, 4, and  $y$  values of 1) showed that  $\text{Ni}^{2+}$  and Ni satellite species are present. The identification of the Ni satellite is utilized to assess the oxidation state of the second group of samples. The quantity of nickel exhibited a small rise when the nickel level in the glass sample rose. Additionally, the XPS data for  $\text{Co}^{2+}$  showed similar patterns. However, it was observed that the concentration of  $\text{Co}^{2+}$  rose as the nickel ratio rose, while it fell when nickel was added. Notably, the peak ratios of  $x = 4$  and  $y = 1$  were reached in this context. This observation indicates that the alteration in oxidation state transition was minimal for the glass samples containing nickel and cobalt dopants. This observation suggests that there may have been minimal electrochemical alteration. Nevertheless, the investigation of the oxidation state will be further examined by the utilization of the XANES technique.

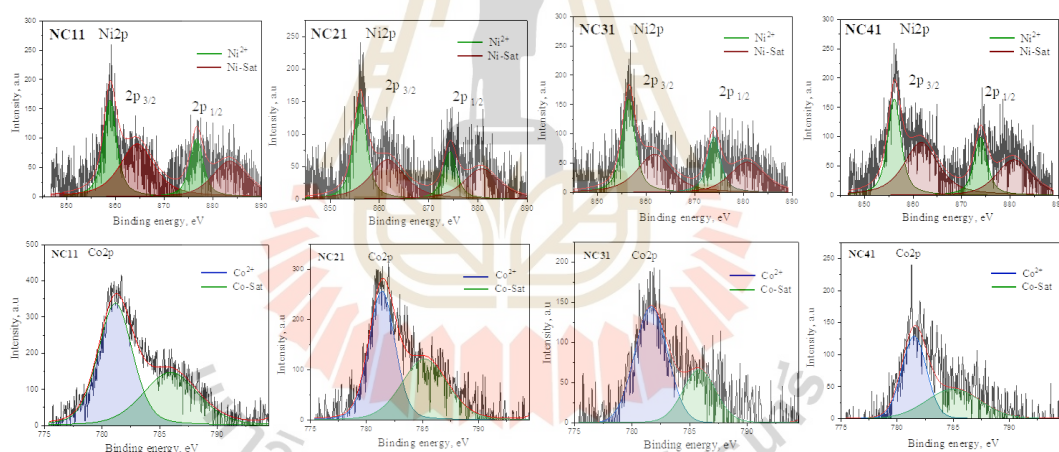


**Figure 4.19** XPS spectra of a series of  $\text{LiBO}_3$  glass samples containing  $x\text{Ni}_y\text{Co}$ , where  $y$  is fixed at 1 and  $x$  varies from 1 to 4.

Figure 4.20 shows the normalized XANES spectra at the Ni K-edge for both Ni/Co-doped  $\text{LiBO}_3$  glass and standard NiO. All the samples of Ni/Co-doped LBO glass showed an increase in energy level compared to the NiO reference. The peak of the first derivative of the data (Figure 4.20a) indicates that the Ni state of glass is greater than  $2+$ , consistent with the  $\text{Ni}^{2+}$  oxidation state in NiO. Figures 4.20b display the Co K-edge

XANES spectra obtained by investigating the oxidation of Co using  $\text{Co}_3\text{O}_4$  and  $\text{CoO}$  as reference materials. In addition, the results demonstrate that the spectra of the glass molecules correspond to those of  $\text{CoO}$  ( $\text{Co}^{2+}$  oxidation). This shows that the Ni/Co-doped  $\text{LiBO}_3$  glass has a  $\text{Co}^{2+}$  state. The inclusion of these cobalt elements significantly impacts the electrical properties of the glass samples. This phenomenon can be attributed to the fact that cobalt exhibits exceptional suitability for cathode use in batteries. The use of cobalt significantly enhances the specific capacity. Nevertheless, the utilization of cobalt has limitations due to its high toxicity.

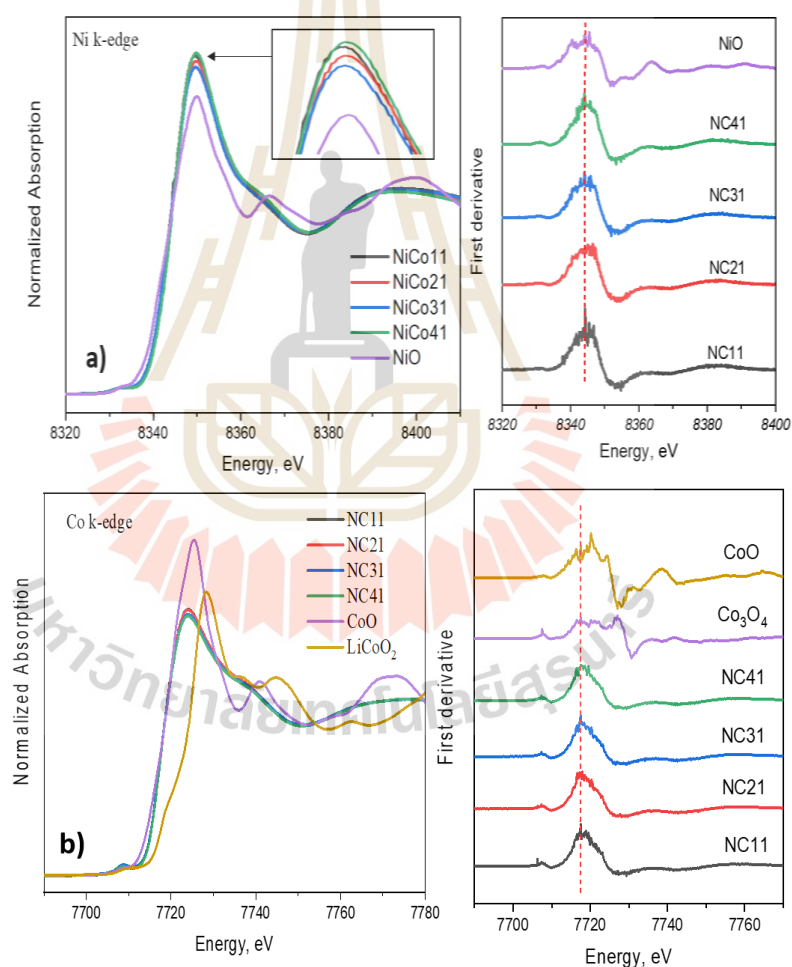


**Figure 4.20**  $\text{LiBO}_3$  doped with NiCo glass system XANES spectra of a) Ni K-edge and first derivative of Ni K-edge, b) Co K-edge and first derivative of Co K-edge.

#### 4.2.5 Magnetic property

The magnetization curves of  $x\text{Ni}_y\text{Mn}:\text{LiBO}_3$  (where  $x = 1, 2, 3, 4$ , and  $y = 1$ ) are illustrated in Figure 4.21. The M-H loops demonstrate the ferromagnetic nature of these materials. Nickel content is inversely correlated with its ferromagnetic properties. It is evident that the magnetic characteristics of an  $x\text{Ni}_y\text{Mn}:\text{LiBO}_3$  sample are directly influenced by the amount of nickel present in the sample. This could be connected to the fact that Li and Ni ions are only partially ordered in the cubic lattice planes. It was assumed that NiO has an antiferromagnetic spin structure, in which the magnetic exchange between the cubic planes is repelled.

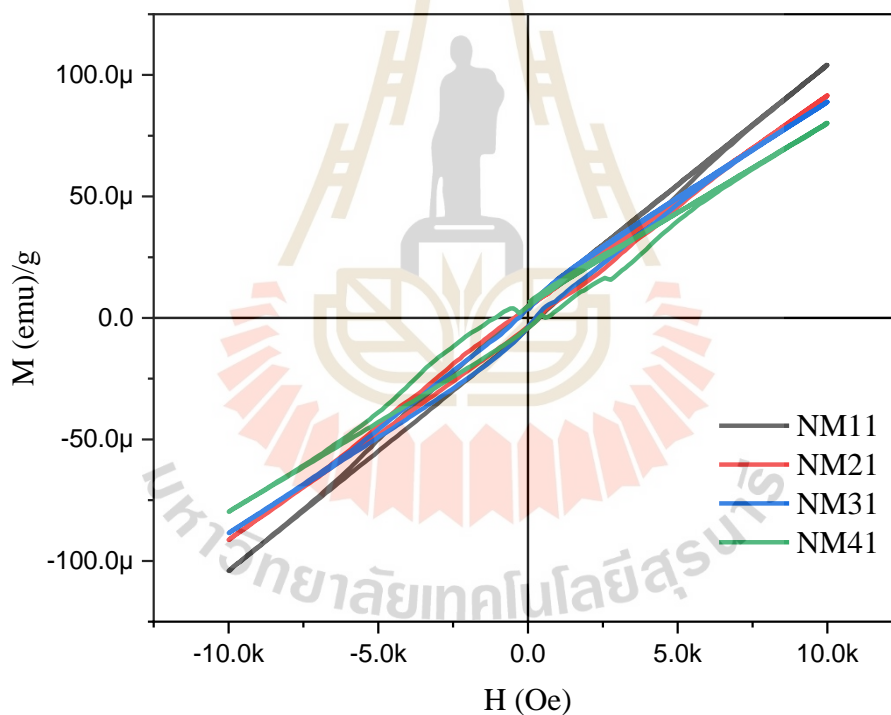


**Figure 4.21** The magnetization (M) versus magnetic field (H) of  $x\text{Ni}_y\text{Mn}:\text{LiBO}_3$  glass system.

Figure 4.22 illustrates the magnetization curves of  $x\text{Ni}_y\text{Co}:\text{LiBO}_3$ , where  $x$  takes the values of 1, 2, 3, 4, and  $y$  is fixed at 1. The ferromagnetic moment of glass samples doped with nickel and cobalt exhibits variation with increasing nickel content. The

study observed a decrease in ferromagnetic properties when the concentration of nickel initially increased. Furthermore, there was a linear correlation observed between it and the nickel quantities found in the samples. However, cobalt plays a crucial role in enhancing the electronic conductivity and layering characteristics of the structure. Additionally, it adds significantly to the overall layering phenomenon. The observed alteration in magnetic characteristics is indicative of a modification in the electrochemical properties of the specimen.

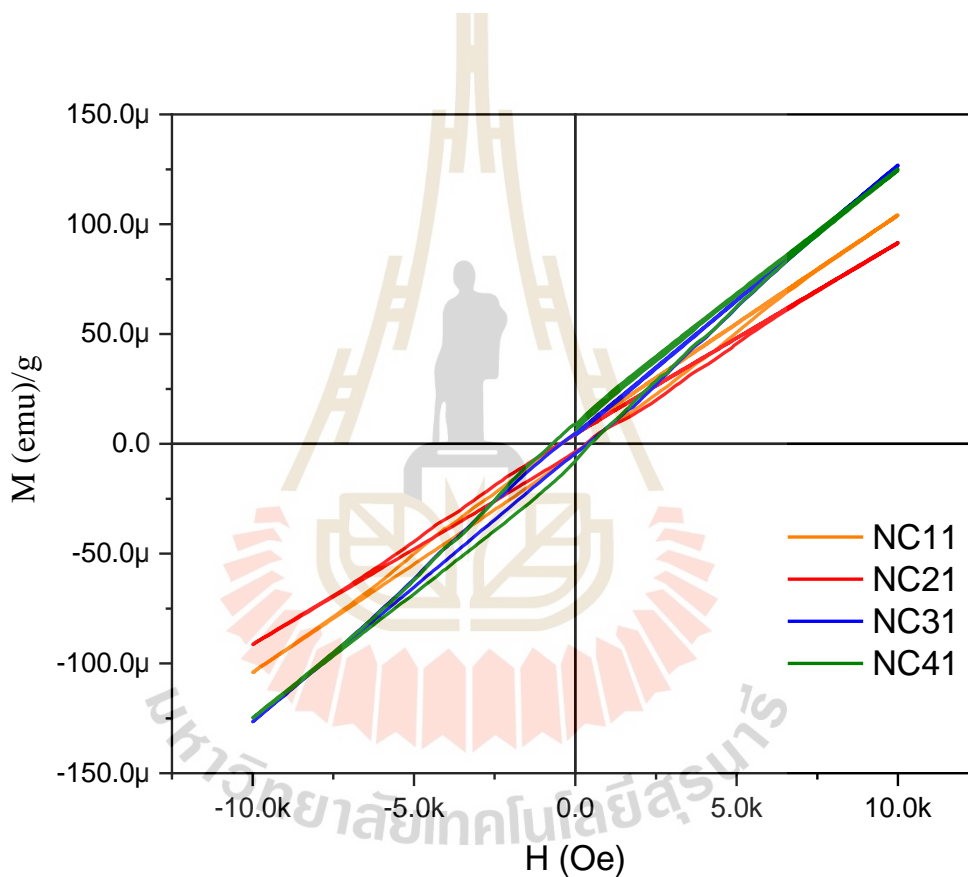


**Figure 4.22** The magnetization (M) versus magnetic field (H) of  $x\text{Ni}_y\text{Co}:\text{LiBO}_3$  (where  $x = 1, 2, 3, 4$ , and  $y = 1$ ) glass system.

#### 4.2.5 Electrochemical properties

For all of the samples in this set ( $\text{LiBO}_3$  dope with NiMn and NiCo),

Electrochemical characteristics were evaluated in advance using the cyclic-voltammetry method on the sample. Glass was powdered and then mixed with a solution of N-Methyl-2-pyrrolidone (NMP), carbon black (CB), and polyvinylidene fluoride (PVDF). The slurry was poured into nickel foam, heated to 90 degrees Celsius for drying, then subjected to a 1 ton press at 120 degrees Fahrenheit for one hour. The sample was then divided into  $1 \times 1 \text{ cm}^2$  squares before being examined in 6 M KOH solution at various scan rates (from 5 mV/s to 100 mV/s). Two peaks, anodic and cathodic (at 2/3 and 1/4 peak), are caused by  $\text{Ni}^{2+}$  redox reactions during charge and discharge. There was a noticeable shift when nickel was added to all of the peak glass samples. As a result, there will be alterations to the electrochemical properties. The specific capacity for each sample ranged from 60 to 80 F/g, with the 3Ni1Mn:LiBO<sub>3</sub> sample providing the highest value at 81.57 F/g. This finding is in agreement with what was found using XPS and XANES before. The values for specific capacity shifts depended on the amount of nickel and manganese added to the glass.

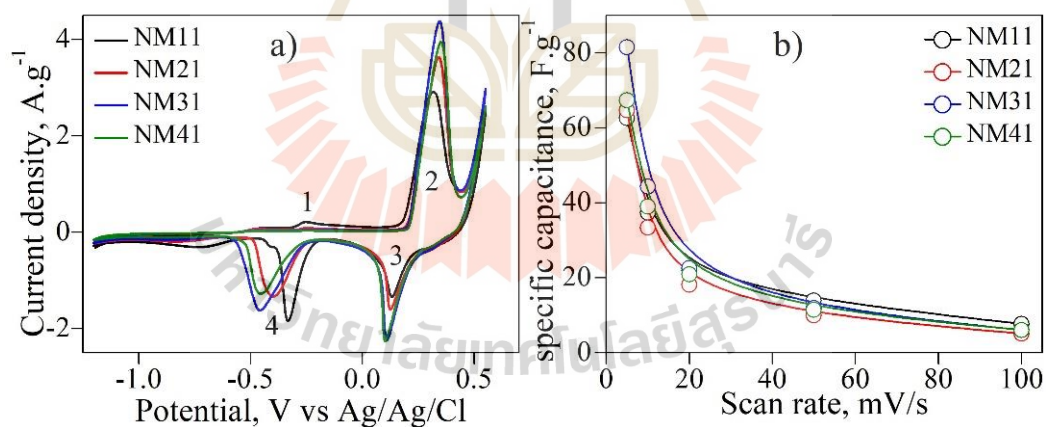


**Figure 4.23** a) The characterization of the  $x\text{Ni}_y\text{Mn}:\text{LiBO}_3$  glass system was conducted using scan rates of 5 mV/s, b) A graphical representation of the relationship between scan rates and specific capacitance.

For a glass sample containing the Ni/Co group, the potential measuring window is 1.5 V to 0.5 V. As can be observed in Figure 4.24, the results are bimodal, with a maximum in the oxidation zone and a maximum in the reduction zone. The peak between A3 and C3 is indicative of the oxidation reduction of Co. According to previous studies, Ni predominates the peak at A4 and C2, whereas Co and Ni appear to be coupling in the C4 region. After that, the precise capacitance was calculated with Equation (1). All of the conditions shown in Figure 2d had specific capacitances greater than 100F/g, and the Ni-rich condition appears to have the highest value, in agreement with the result of the single-dope group.

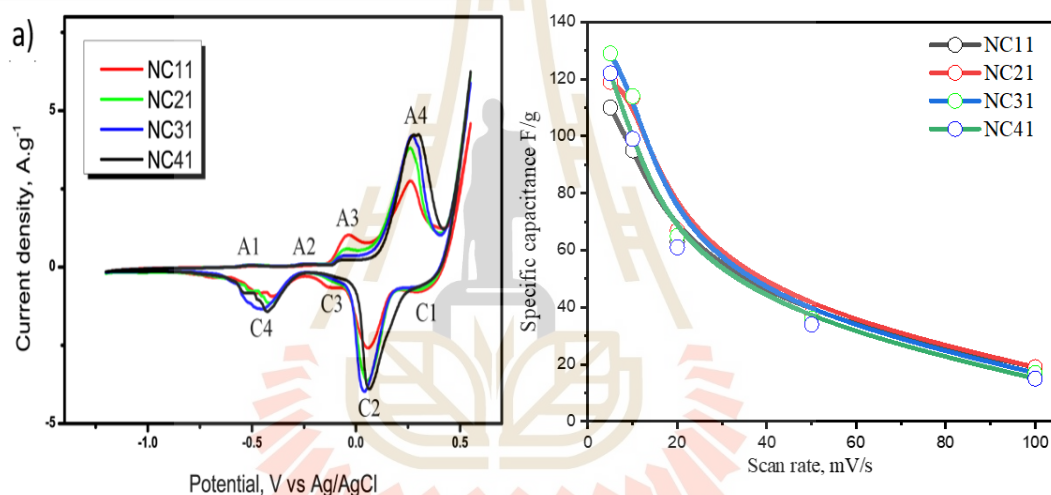


**Figure 4.24** a) The characterization of the  $x\text{Ni}_y\text{Co}:\text{LiBO}_3$  glass system using scan rates of 5 mV/s, and b) A graphical representation to illustrate the relationship between scan rates and specific capacitance in the  $\text{LiBO}_3$  glass system.

### 4.3 Triple-Doping

#### 4.3.1 Physical characteristics

Regarding the third bunch of glass samples (the Triple Doping). The glass sample has the same qualities that are typical of  $\text{LiBO}_3$  glass-doped nickel-cobalt,

including opacity, smoothness, and a high degree of shine. It appears black to the unaided eye but takes on a deep purple hue when viewed through light. In conclusion, the overall appearance of each instance is the same: smooth and shining. The color varies with the presence of different transition metals in the glass.



**Figure 4.25** Prepared  $x\text{Ni}_y\text{Mn}_z\text{Co}:\text{LiBO}_3$  plate glasses where  $y = 1, z = 1$  and  $x = 1, 2, 3$  and 4.

#### 4.3.2 Phase identification

XRD pattern of the most recent set of samples, specifically the triple-doped group, exhibited a significant resemblance, characterized by a broad peak, to that of the preceding group. As depicted in Figure 4.26, the X-ray diffraction (XRD) peak has a prominent and substantial shape. The presence of a wide peak in the pattern can be attributed to the phenomenon of diffuse scattering, which arises from the disordered nature of the amorphous material. This finding provides evidence that all specimens

possess an amorphous configuration. Consequently, it is evident that XRD patterns of all the samples indicate their amorphous nature. None of the samples exhibit a crystalline structure. The identification of the constituents within the glass sample was aided through the utilization of an EDS image. The composition of  $x\text{Ni}_y\text{Co}:\text{LiBO}_3$  (with  $x$  values of 1, 2, 3, 4, and  $y$  values of 1) was determined to consist of boron (B), nickel (Ni), cobalt (Co), manganese (Mn), and oxygen (O), as seen by the weight percentage (wt%) depicted in Figure 4.27.

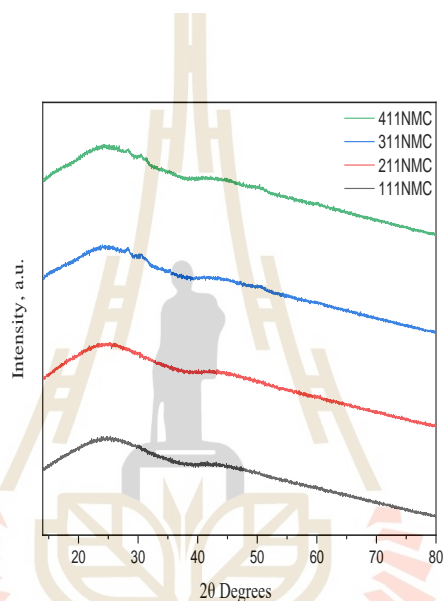


**Figure 4.26** XRD patterns of  $x\text{Ni}_y\text{MnzCo}:\text{LiBO}_3$  plate glasses where  $y = 1, z = 1$  and  $x = 1, 2, 3$  and 4.

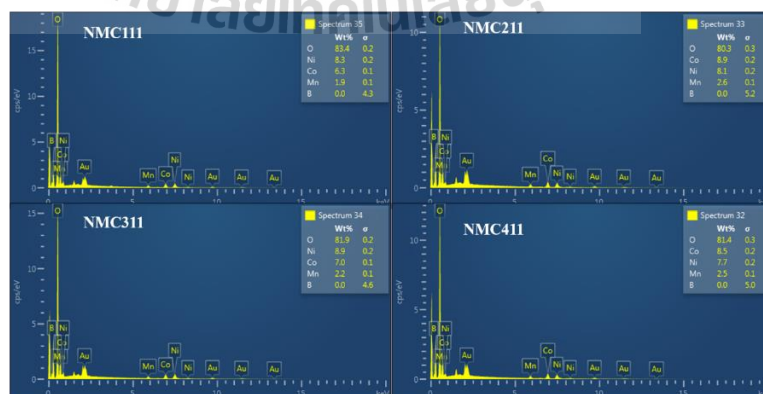


**Figure 4.27** EDS spectra of  $x\text{Ni}_y\text{Co}:\text{LiBO}_3$  (with  $x$  values of 1, 2, 3, 4, and  $y = 1$ ).

### 4.3.3 Optical gap energy analysis

Analogous to the co doping group, as exemplified in the aforementioned case. The UV-visible spectrum of the triple-doped material exhibits three distinct absorption zones at wavelengths of 425, 512, and 645 nm. The first region at a wavelength of 430 nm is ascribed to the presence of  $\text{Ni}^{2+}$  ions in an octahedral coordination environment. This corresponds to the transition of  ${}^3\text{A}_{2g}(\text{F})$  to  ${}^3\text{T}_{1g}(\text{P})$  of the  $\text{Ni}^{2+}$  ions. The change of nickel from  ${}^3\text{A}_{2g}$  to  ${}^3\text{T}_{1g}$  can be associated with region 3. The 645 nm region, specifically region 2, can be attributed to the  ${}^4\text{T}_{1g} \rightarrow {}^4\text{A}_{2g}$  transitions of  $\text{Co}^{2+}$ ,  $\text{Mn}^{2+}$ , and  $\text{Mn}^{3+}$  ions. However, it is evident that the intensity of region 2 diminishes with an increase in the concentration of nickel in the sample. This entails the reduction of  $\text{Co}^{2+}$ ,  $\text{Mn}^{2+}$ , and  $\text{Mn}^{3+}$  ions within the glass specimen. In the subsequent part, the examination of alterations in oxidation state as observed in the UV-vis spectrum will be conducted through the utilization of XPS and XANES techniques.

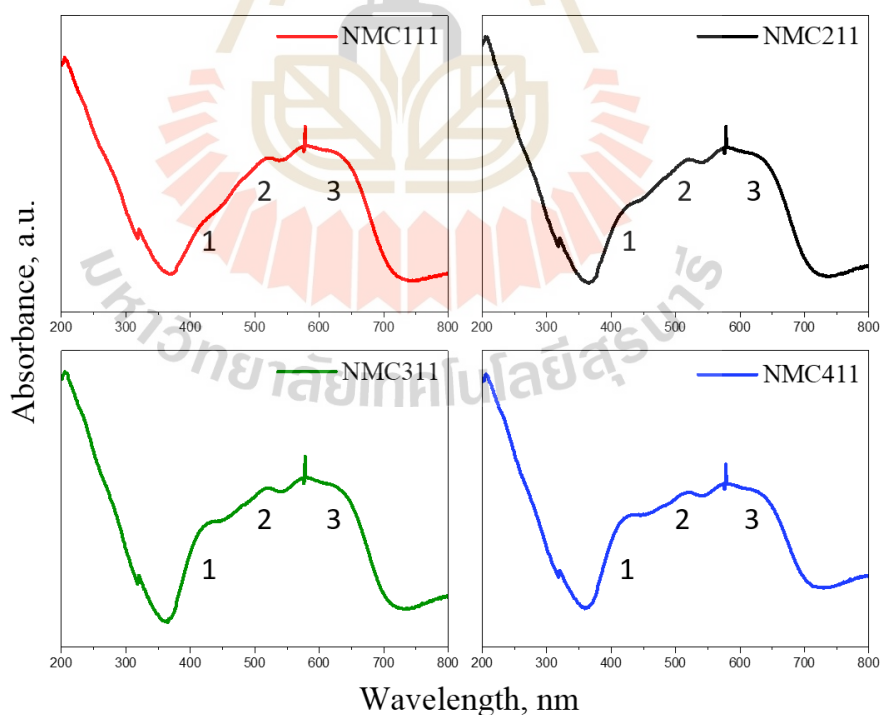


**Figure 4.28** Optical absorbance spectra of  $x\text{Ni}y\text{Mn}z\text{Co}:\text{LiBO}_3$  (with  $x$  values of 1, 2, 3, 4, and  $y, z$  values of 1).

#### 4.3.4 XPS and XANES analyses

Regarding the final specimen (triple dope), the XPS data showed that the oxidation state of the sample changed as the nickel doping level increased. As can be seen from the XPS fitting of the sample  $x\text{Ni}_y\text{Mn}_z\text{Co}:\text{LiBO}_3$  (where  $x = 1, 2, 3, 4$ , and  $y, z = 1$ ), the concentration of  $\text{Ni}^{2+}$  increases noticeably as  $x$  increases, while Mn2p is composed of  $\text{Mn}^{2+}$  and  $\text{Mn}^{3+}$  and changes inconsistently. On the other hand, as  $x$  increased, there was a significant decrease in the level of  $\text{Co}^{2+}$  in the sample.

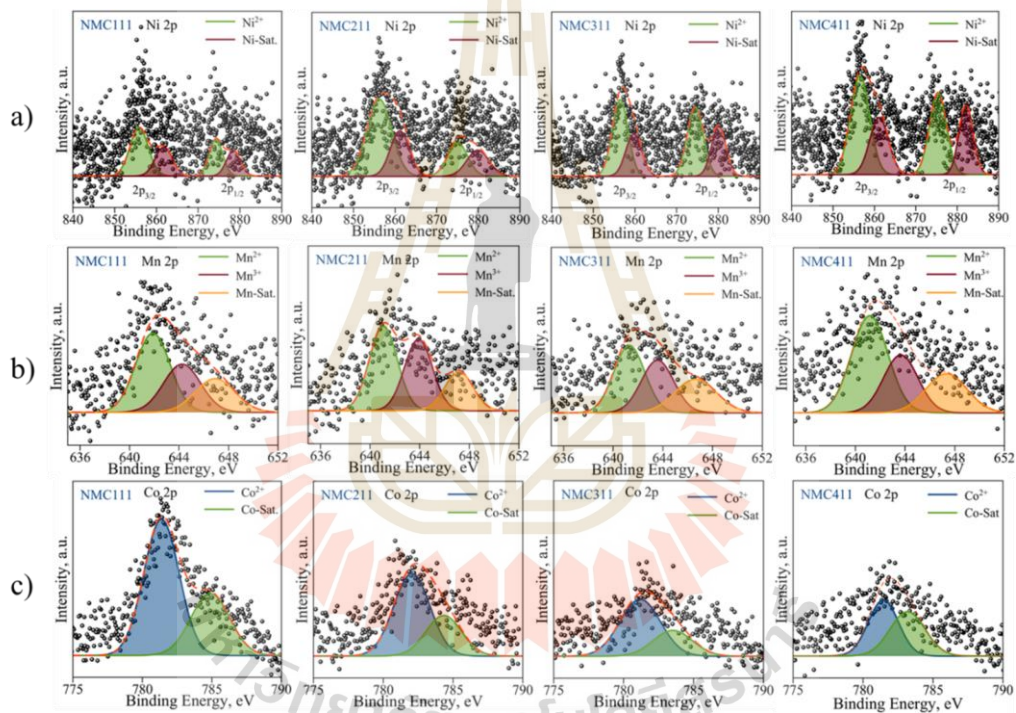
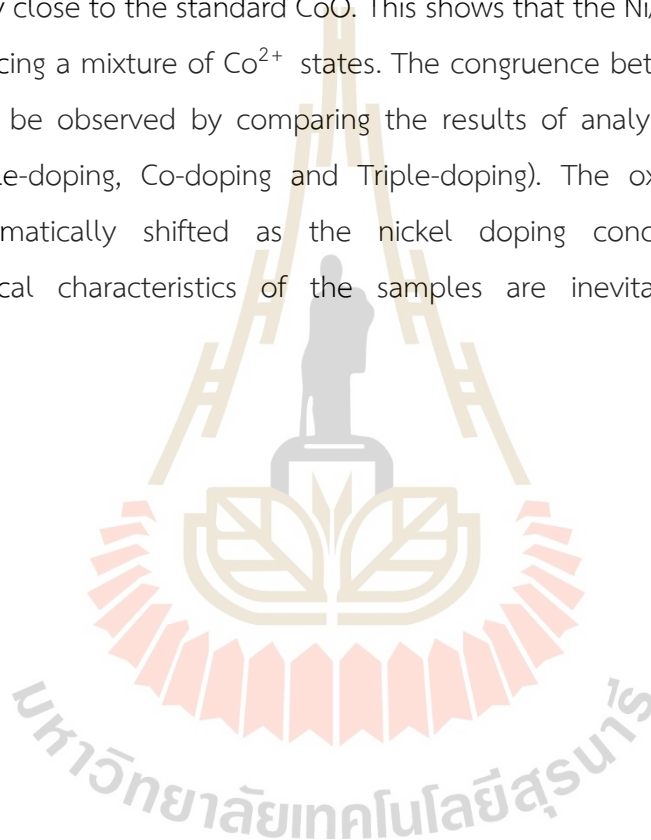
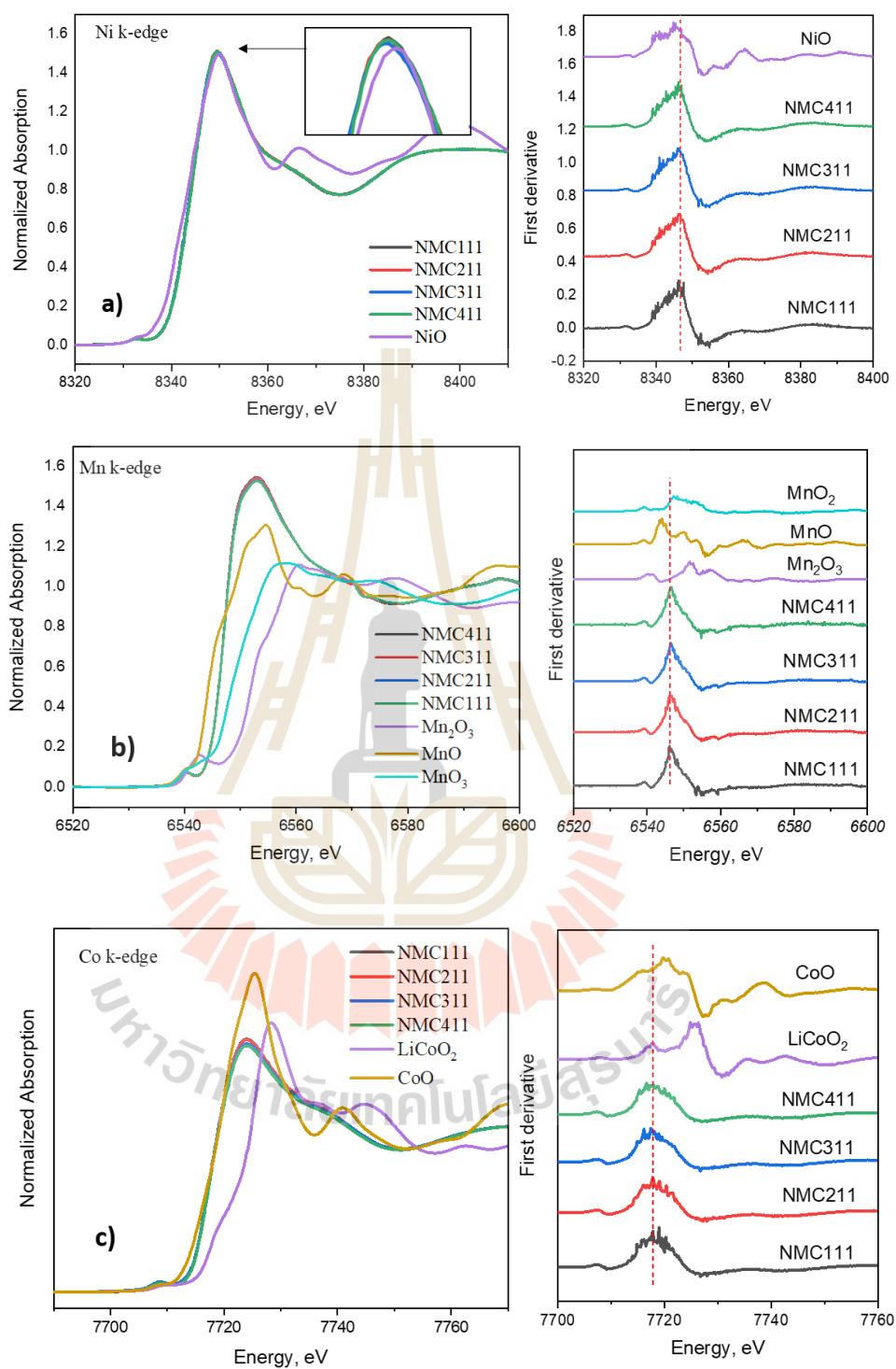


Figure 4.29 XPS spectra of NMC:LiBO<sub>3</sub> glass.

Figure 4.30a shows the traditional XANES spectra for NiO and the normalized absorption spectra at the Ni K-edge for  $x\text{Ni}_y\text{Mn}_z\text{Co}:\text{LiBO}_3$  (where  $x = 1, 2, 3$ , and  $y, z = 1$ ). When compared to the NiO standard, all samples have a change in the position of the 1s to 4p peak, which shows that the oxidation state of Ni has changed ( $\text{Ni}^{2+}$  and higher than 2+ are mixed together). The absorption Mn K-edge XANES spectra and the

white line position of all samples in this set are shown in Figure 11. It is apparent that the absorption edge of all samples has energy between MnO and Mn<sub>2</sub>O<sub>3</sub>, as indicated by the position of the white line. This demonstrates that the Mn in the sample exists in both the 2+ and 3+ oxidation states. Figures 4.15c and 4.15f show the Co K-edge XANES spectra that were made by studying the oxidation of Co with Co<sub>3</sub>O<sub>4</sub> and CoO as reference materials. The results also reveal that the spectra of glass agree with those of CoO (Co<sup>2+</sup> oxidation). The position of the white line (WL) shows that all the energies are extremely close to the standard CoO. This shows that the Ni/Co-doped LiBO<sub>3</sub> glass was experiencing a mixture of Co<sup>2+</sup> states. The congruence between XPS and XANES analyses can be observed by comparing the results of analyses performed on all samples (Single-doping, Co-doping and Triple-doping). The oxidation state of the material dramatically shifted as the nickel doping concentration rose. The electrochemical characteristics of the samples are inevitably altered by this modification.





**Figure 4.30** XANES spectra of a) Ni K-edge, b) Mn K-edge, c) Co K-edge, d) first derivative of Ni K-edge, e) first derivative of Mn K-edge and f) first derivative of Co K-edge of LiBO<sub>3</sub> doped with NMC glass system.

### 4.3.5 Magnetic property

In comparison to the other specimens, the glass sample  $x\text{Ni}y\text{Mn}z\text{Co}:\text{LiBO}_3$  (where  $x = 1, 2, 3$ , and  $y$  and  $z = 1$ ) exhibits reduced values for both saturation magnetization ( $M_s$ ) and coercive field ( $H_C$ ). Furthermore, it has been shown that there is a significant decrease in the remanent magnetization ( $M_r$ ) when the  $x$  ratio grows. The specimens from this particular group exhibit paramagnetic characteristics. This implies that glass samples belonging to these groups may demonstrate inferior electrochemical properties in comparison to the remaining groups. This problem could perhaps be attributed to an inaccurate ratio between nickel, manganese, and cobalt.

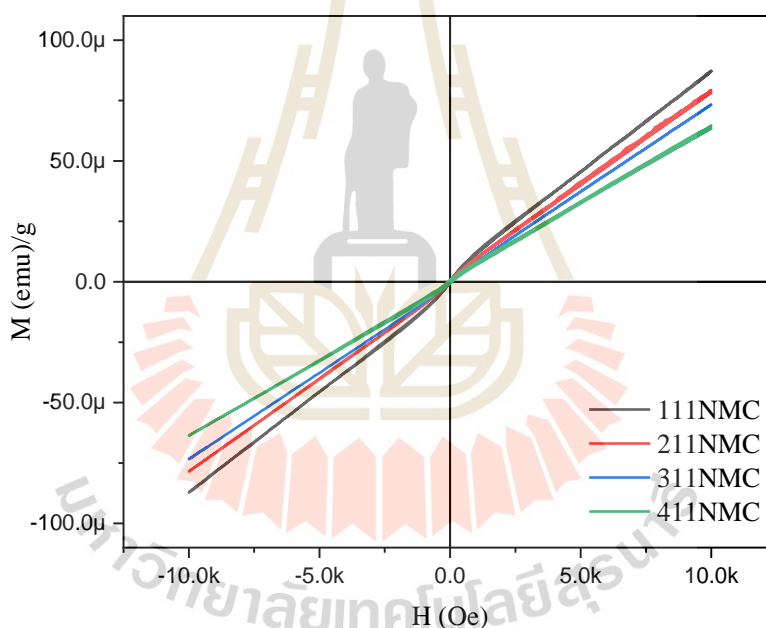


**Figure 4.31** The magnetization ( $M$ ) versus magnetic field ( $H$ ) of  $x\text{Ni}y\text{Mn}z\text{Co}:\text{LiBO}_3$  (where  $x = 1, 2, 3$ , and  $y$  and  $z = 1$ ) glass system.

### 4.3.6 Electrochemical properties

Cyclic voltammetry was used to conduct an in-depth analysis on the specimen in order to make an accurate prediction of its electrochemical properties. Glass was

ground into a powder and combined with a solution of N-Methyl-2-pyrrolidone (NMP), carbon black (CB), and polyvinylidene fluoride (PVDF). The slurry was put into nickel foam, dried at 90 degrees Celsius, and then pressed for one hour at 120 degrees Fahrenheit using a one-ton press. After cutting the sample into 1x1 cm<sup>2</sup> squares, we scanned it at different speeds (from 5 mV/s to 100 mV/s) in 6 M KOH solution to see how it responded. The charge and discharge processes induce the Ni<sup>2+</sup> redox reactions that cause the peaks at A4 and C2. When the nickel concentration is raised, the peak shifts visibly. Furthermore, the peak between A3 and C3, which subsequently lowered as nickel was added, was suggestive of the oxidation reduction of Co. Specific capacitances of LiBO<sub>3</sub>: xNiyMnzCo electrodes (where x = 1, 2, 3, and y and z = 1) were calculated using Eq. (1), obtaining values of 66.46, 72.35, 59.5, and 54.06 F/g at a scan rate of 5 mV/s. Glass electrodes exhibit higher specific capacitance values, albeit solely at low scan rates. This phenomenon can be attributed to the fact that a reduced scan rate allows ions a longer duration to traverse the distance to the electrode surface, thereby facilitating a more effective transfer of ions.

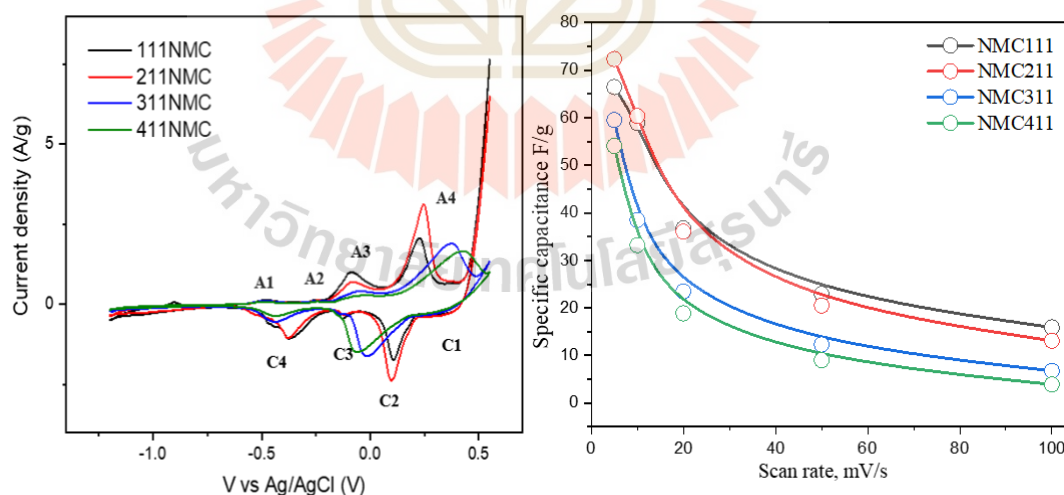


**Figure 4.32** a) CV analysis was performed on the LiBO<sub>3</sub> glass system using a scan rate of 5 mV/s, and b) The specific capacitance was shown as a function of scan rates for the LiBO<sub>3</sub> glass system.

## CHAPTER V

### CONCLUSIONS AND REMARKS

This thesis demonstrates that the electrochemical characteristics of lithium borate glasses can be improved by doping them with transition metals. Different amounts and proportions of transition metals have distinct results for properties. In this thesis, the effects of transition metal alloying have been investigated using a number of different methods. The following is a synthesis of all experimental findings.

The production of lithium borate glass samples doped with transition metals was accomplished effectively by the utilization of the melt-quenching approach. Upon initial observation, the samples had a luminous and transparent appearance, characterized by diverse hues that indicated the existence of several transition metals. The fundamental objective of this inquiry is to examine the features of lithium-borate glass. In order to preserve the amorphous structure of all samples, XRD was employed. XRD analysis unequivocally demonstrates that all samples exhibit an amorphous state.

The transference of electrons in the context of an oxidation-reduction (redox) reaction is a fundamental component of electrochemical phenomena. Understanding the phenomenon of electrochemical charge variation resulting from the introduction of transition metals into glass necessitates a comprehensive knowledge of their respective oxidation states. Therefore, the utilization of XPS and XANES techniques is employed to investigate the aforementioned scenario. In the initial set of samples (referred to as Single-doping), both  $\text{Ni}^{2+}$  and  $\text{Ni}^{3+}$  oxidation states of nickel are present. The concentration of  $\text{Ni}^{3+}$  in the glass increases proportionally with the rise in the nickel-to-nickel ratio. In alternative specimens, such as Co-Doping and Triple-Doping, the manipulation of the nickel ratio resulted in a modification of the oxidation state of the transition metals within the glass sample. These metals included  $\text{Mn}^{2+}$ ,  $\text{Mn}^{3+}$ ,  $\text{Co}^{2+}$ , and  $\text{Ni}^{2+}$ . Changes in these oxidation states can affect electrochemical characteristics for a variety of reasons.  $\text{Li}^+$  and  $\text{Ni}^{2+}$  tend to combine when the latter is more abundant. Cation mixing can reduce specific capacity in high-nickel NCM-based materials, for

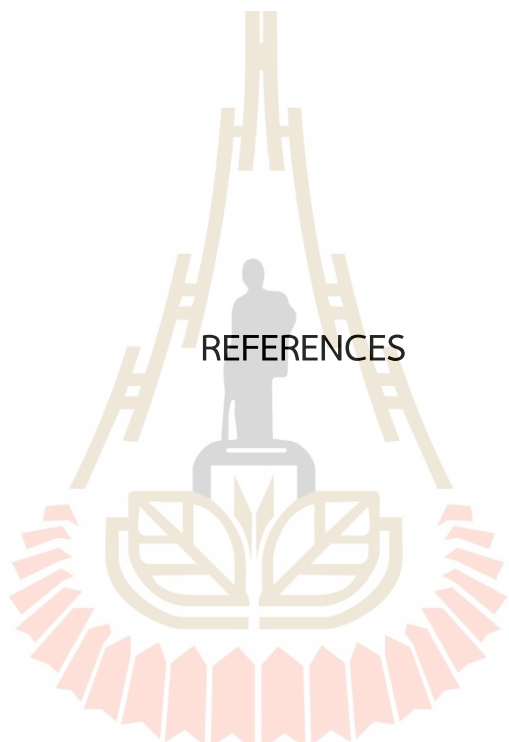
example, if  $\text{Ni}^{2+}$  replaces  $\text{Li}^+$ . The low-valence nickel ion from the transition metal (Co, Mn) layer can migrate to the lithium layer, filling up the lithium vacancies and disturbing the diffusion of  $\text{Li}^+$ , further limiting the capacity of the battery to charge. However, by impeding  $\text{Ni}^{2+}$  transport into the Li layer, even a trace amount of cobalt ( $\text{Co}^{2+}$ ) can preserve the structure. The presence of Co also improves electric conductivity and allows for high-rate capability. The thermal stability of materials in the delithiated state can also be improved by adding a small amount of Mn dopant. The surface structure of Ni-rich cathode material might be stabilized by Mn ions in one way: they might stop side reactions that cannot be undone between the electrolyte and the electrode surface.

The examination of the magnetic properties of glass doped with transition metals demonstrates a discernible modification in its magnetic features. In the case of a single dopant, it was seen that the alteration in the concentration of nickel resulted in a substantial modification of the magnetic characteristics of the glass specimen, transitioning from diamagnetic behavior to ferromagnetic behavior. Scientific research substantiates the notion that ferromagnetic materials possess superior electrochemical characteristics compared to paramagnetic and diamagnetic materials. The triple dope group has unique characteristics in comparison to other samples and is notably defined by its paramagnetic properties. This phenomenon has the potential to result in a decrease in the electrochemical properties of glass when compared to other categories.

In order to investigate the electrochemical characteristics of all specimens. The glass electrodes used in this study were manufactured as samples immersed in a potassium hydroxide (KOH) electrolyte. The alteration in nickel content was shown to have a discernible impact on the specific capacity. In the initial sample (single-doping), the glass exhibited a substantial enhancement in specific capacity upon the introduction of nickel doping. The co-doped glass group, particularly the nickel-cobalt-doped glass subgroup, exhibited superior or elevated specific capacity values compared to the remaining groups. The observed phenomenon can be attributed to the inclusion of a minute quantity of cobalt in the specimen, which successfully mitigates the occurrence of cation mixing involving lithium and nickel ions ( $\text{Li}^+/\text{Ni}^{2+}$ ).

Nevertheless, the final set of samples, referred to as the triple-dope group, had comparatively inferior electrochemical characteristics in relation to the previous groups. The glass samples are composed of cobalt, which hinders the transportation of  $\text{Ni}^{2+}$  ions into the Li layer, and manganese, which contributes to the preservation of thermal stability in the glass samples. However, the observed electrochemical characteristics of this particular group of glass samples were comparatively lower when compared to the other groups. This phenomenon could arise because of an imbalanced proportion of nickel, manganese, and cobalt. Hence, the observed value of the capacity in this particular set of glass samples is the minimum.





REFERENCES

มหาวิทยาลัยเทคโนโลยีสุรนารี

## REFERENCES

- Afyon, S., Krumeich, F., Mensing, C., Borgschulte, A. and Nesper, R. (2014). New High Capacity Cathode Materials for Rechargeable Li-ion Batteries: Vanadate-Borate Glasses. *Scientific Reports*, 4, 7113.
- Annibale, M. and Augusto, M. (2015). The Historical Development of X-ray Absorption Fine Spectroscopy and of Its Applications to Materials Science. book series, *HMMS*, volume 27.
- Barpanda, P., Dwibedi, D., Ghosh, S., Kee, Y. and Okada, S. (2015). Lithium metal borate (LiMBO<sub>3</sub>) family of insertion materials for Li-ion batteries: a sneak peek. *Ionics*, 21(7), 1801–1812.
- Barpanda, P., Yamashita, Y., Yamada, Y. and Yamada, A. (2013). High-Throughput Solution Combustion Synthesis of High-Capacity LiFeBO<sub>3</sub> Cathode. *Journal of The Electrochemical Society*, 160(5), A3095–A3099.
- Borisov, S.V., Golovachev, V.P., Ilyukhin, V.V. and Kuzmin E.A. (1981). Symmetric Relations in the Patterson Function [in Russian], Nauka, Novosibirsk.
- Brusentsev, F.A. and Dvoryankin, V.F. (1963). ANALYTIC REPRESENTATION OF ATOMIC SCATTERING FACTORS FOR ELECTRONS. *Crystallography*, 8, ed. 1, 10-15.
- Burger, M. and Belov, N.V. (1961). Crystal Structure and Vector Space, Lit-ra, Moscow.
- Butnoi, P., Chanlek, N., Poo-arporn, Y., Pinitsoontorn, S., Maensiri, S. and Kidkhunthod, P. (2019). Structure-function of novel glasses for possibility as cathode of Li-ion battery: Lithium manganese borate glasses. *Journal of Alloys and Compounds*, 151811.
- Carlo, L. and Jeroen A. (2016). Chapter 1 Introduction: Historical Perspective on XAS.

- Cheng, Y., Feng, K., Song, Z., Zhang, H., Li, X. and Zhang, H. (2018). Li<sub>0.93</sub>V<sub>2</sub>O<sub>7</sub>BO<sub>5</sub>: a new nano-rod cathode material for lithium ion batteries. *Nanoscale*, 10(4), 1997–2003.
- Chi, Y., Guo, S.-P., Kong, H.-J. and Xue, H.-G. (2016). Crystal and electronic structures, and optical and magnetic properties of novel rare-earth sulfide borates RE<sub>3</sub>S<sub>3</sub>BO<sub>3</sub> (RE = Sm, Gd). *New Journal of Chemistry*, 40(8), 6720–6727.
- Chi, Y., Xue, H.G. and Guo, S.P. (2020). *Designing Sulfide Borate as a Novel Type of Second-Order Nonlinear-Optical Material. Inorganic Chemistry*.
- Dong, Y. Z., Zhao, Y. M., Shi, Z. D., An, X. N., Fu, P. and Chen, L. (2008). The structure and electrochemical performance of LiFeBO<sub>3</sub> as a novel Li-battery cathode material. *Electrochimica Acta*, 53(5), 2339–2345.
- En-Lai, Z., Shi-Xi, Z., Xia, W., Jing-Wei, L., Lü-Qiang, Y., Ce-Wen, N. and Guozhong C. (2019). Electrochemical performance of Li<sub>2</sub>O-V<sub>2</sub>O<sub>5</sub>-SiO<sub>2</sub>- B<sub>2</sub>O<sub>3</sub> glass as cathode material for lithium ion batteries. *Journal of Materiomics*. 663-669.
- Fan, L., Wei, S., Li, S., Li, Q. and Lu, Y. (2018). Recent progress of the solid-state electrolytes for high-energy metal-based batteries. *Advanced Energy Materials*. 8, 1702657.
- Gamilton U.K. (1972). *Russian Chemical Reviews*, 41, ed. 3, 566-583.
- Goodenough, J.B. and Park, K.S. (2013). The Li-Ion Rechargeable Battery: A Perspective. *Journal of the American Chemical Society*, 135(4), 1167–1176.
- Hang, M.N., Gunsolus, I.L., Wayland, H., Melby, E.S., Mensch, A.C., Hurley, K.R. and Hamers, R.J. (2016). *Chemistry of Materials*, 28(4), 1092- 1100.
- Hari P.K., Subramanian, S., Sairam, T.N., Amarendra, G., Srinadhu, E.S. and Satyanarayana, N. (2017). Structural, electrical and dielectric properties of nanocrystalline LiMgBO<sub>3</sub> particles synthesized by Pechini process. *Journal of Alloys and Compounds*. 718, 459–470.

- Il'ina, E., Druzhinin, K., Saetova, N. and Antonov. B.D. (2018). Interface features between  $30\text{Li}_2\text{O} \cdot 47.5\text{V}_2\text{O}_5 \cdot 22.5\text{B}_2\text{O}_3$  glassy cathode and  $\text{Li}_7\text{La}_3\text{Zr}_2\text{O}_{12}$  solid electrolyte. *Electrochimica Acta*. 326-335.
- Liu, P., Zhu, K., Gao, Y., Luo, H. and Lu, L. (2017). Recent Progress in the Applications of Vanadium-Based Oxides on Energy Storage: from Low-Dimensional Nanomaterials Synthesis to 3D Micro/Nano-Structures and Free-Standing Electrodes Fabrication. *Advanced Energy Materials*, 7(23), 1700547.
- Jochen, F. (2001). Crystalline Nanoparticles in Glasses for Optical Application Handbook of Surfaces and Interfaces of Materials. 311-350.
- Jun, Y., Junpeng, L., Zhuangjun, F., Tong, W. and Lijun, Z. (2012). High-performance supercapacitor electrodes based on highly corrugated graphene sheets. 50(6), 2179–2188.
- Kang, B. and Ceder, G. (2009). Battery materials for ultrafast charging and discharging. *Nature*, 458(7235), 190–193.
- Kang, H.S., Santhoshkumar, P., Park, J.W., Sim, G.S., Nanthagopal, M. and Lee, C.W. (2020). Glass ceramic coating on  $\text{LiNi}_0.8\text{Co}_0.1\text{Mn}_0.1\text{O}_2$  cathode for Li-ion batteries. *Korean Journal of Chemical Engineering*, 37(8), 1331–1339.
- Karmakar. B. (2016). Chapter 1 - Fundamentals of Glass and Glass Nanocomposites Glass Nanocomposites Synthesis, Properties and Applications. 3-53.
- Kaymaksiz, S., Wilhelm, F., Wachtler, M., Wohlfahrt-Mehrens, Ma., Hartnig, C., Tschernych, I. and Wietelmann, U. (2013). Electrochemical stability of lithium salicylato-borates as electrolyte additives in Li-ion batteries. *Journal of Power Sources*, 239, 659–669.
- Kitaigorodsky, A.I. (1957). Theory of Structural Analysis, Izd. AN SSSR, Moscow.
- Li, A., Xu, L., Li, C. M. and Qian, Y. (2016). Mesh-like  $\text{LiZnBO}_3/\text{C}$  composites as a prominent stable anode for lithium ion rechargeable batteries. *Journal of Materials Chemistry A*, 4(15), 5489–5494.

- Li, S., Xu, L., Li, G., Wang, M. and Zhai, Y. (2013). In-situ controllable synthesis and performance investigation of carbon-coated monoclinic and hexagonal LiMnBO<sub>3</sub> composites as cathode materials in lithium-ion batteries. *Journal of Power Sources*, 236, 54–60.
- Liu, P., Zhu, K., Gao, Y., Luo, H. and Lu, L. (2017). Recent Progress in the Applications of Vanadium-Based Oxides on Energy Storage: from Low-Dimensional Nanomaterials Synthesis to 3D Micro/Nano-Structures and Free-Standing Electrodes Fabrication. *Advanced Energy Materials*, 7(23), 1700547.
- Liu, S., Tong, Z., Zhao, J., Liu, X., Wang, J., Ma, X., Chi, C., Yang, Y., Liu, X.X. and Li, Y. (2016). Rational selection of amorphous or crystalline V<sub>2</sub>O<sub>5</sub> cathode. *Physical Chemistry Chemical Physics*, 18(36), 25645–25654.
- Montreeupathum, A., Kidkhunthod, P., Rujirawat, S., Yimnirun, R., Pinitsoontorn, S. and Maensiri, S. (2020). Effect of borate glass network to electrochemical properties: Manganese-doped lithium borate glasses. *Radiation Physics and Chemistry*, 170, 108677.
- Muraliganth, T., Stroukoff, K.R. and Manthiram, A. (2010). Microwave Solvo thermal Synthesis of Nanostructured Li<sub>2</sub>MSiO<sub>4</sub>/C (M = Mn and Fe) Cathodes for Lithium-Ion Batteries. *Chemistry of Materials*, 22(20), 5754–5761.
- NIST Inorganic Crystal Structure Database (ICSD) SRD 3.
- Sarawut Sujitjorn. (2015). THAI SYNCHROTRON FACILITY: IT'S PAST AND PRESENT.
- Sheldrick G.M. (1998). SHELX97 Release 97-2, Univ. Göttingen, Germany.
- Shi, Z.H., Chi, Y., Yang, M., Liu, W. and Guo, S.P. (2020). A Series of Chalcogenide Borates RE<sub>6</sub>Ta<sub>2</sub>MgQB<sub>8</sub>O<sub>26</sub> (RE = Sm, Eu, Gd; Q = S, Se) Featuring a B<sub>4</sub>O<sub>10</sub> Cluster. *Inorganic Chemistry*.
- Stoch, S. (1999). Flexibility of structure and glass-forming ability: a chemical approach. *J. Glass Physics and Chemistry*. 27(2), 167–174.

- Swiderska, M.A. and Naparstek, D. (2016). Physical and electrochemical properties of lithium bis(oxalate) borate organic mixed electrolytes in Li-ion batteries. *Electrochimica Acta*, 204, 6977.
- Tae, H.N. and Ee L.S. (2017). Study of CuO content on physical and structural properties of Li<sub>2</sub>O-B<sub>2</sub>O<sub>3</sub>-CuO glasses using electron paramagnetic resonance. *Journal of Non-Crystalline Solids*. 37-42.
- Tsai, Y.T., Wu, C.Y. and Duh, J.G. (2021). Synthesis of Ni-rich NMC cathode material by redox-assisted deposition method for lithium ion batteries. *Electrochimica Acta*, 381, 138244.
- Vainshtein B.K. (1979- 1981). Modern Crystallography, 4 vol., Nauka, Moscow.
- Wang, H., Isobe, J., Matsumura, D. and Yoshikawa, H. (2018). In situ X-ray absorption fine structure studies of amorphous and crystalline polyoxovanadate cluster cathodes for lithium batteries. *Journal of Solid State Electrochemistry. Journal of Solid State Electrochemistry*, 22(7), 2067–2071.
- Wei, Z., Wang, D., Yang, X., Wang, C., Chen, G. and Du, F. (2018). *Advanced Materials Interfaces*, 1800639.
- Wu, X., Zhao, S.X., Yu, L.Q., Li, J.W., Zhao, E.L. and Nan, C.W. (2019). Lithium storage behavior of MoO<sub>3</sub>-P<sub>2</sub>O<sub>5</sub> glass as cathode material for Li-ion batteries. *Electrochimica Acta*, 297, 872–878.
- Yang, S.H., Xue, H. and Guo, S.P. (2021). Borates as promising electrode materials for rechargeable batteries. *Coordination Chemistry Reviews*, 427, 213551.
- Yamada, A., Iwane, N., Harada, Y., Nishimura, S., Koyama, Y. and Tanaka, I. (2010). Lithium Iron Borates as High-Capacity Battery Electrodes. *Advanced Materials*, 22(32), 3583–3587.
- Yamada, A., Iwane, N., Nishimura, S., Koyama, Y. and Tanaka, I. (2011). Synthesis and electrochemistry of monoclinic Li(MnxFe<sub>1-x</sub>)BO<sub>3</sub>: a combined experimental and computational study. *Journal of Materials Chemistry*, 21(29), 10690.

- Yihan, X., Yan, W. and Gerbrand, C. (2019). Computational Screening of Cathode Coatings for Solid-State Batteries. *3, 5*, P1252-1275.
- Zeng, X., Kuang, Q., Fan, Q., Dong, Y., Zhao, Y., Chen, S. and Liu, S. (2020). Synthesis, structure, and electrochemical performance of V<sub>3</sub>BO<sub>6</sub> nanocomposite: A new vanadium borate as high-rate anode for Li-ion batteries. *Electrochimica Acta, 335*, 135661.
- Zhang, B., Ming, L., Zheng, J., Zhang, J., Shen, C., Han, Y. and Qin, S. (2014). Synthesis and characterization of multi-layer core-shell structural LiFeBO<sub>3</sub>/C as a novel Li-battery cathode material. *Journal of Power Sources, 261*, 249–254.
- Zhang, J., Zhang, H. and Xu, J. (2019) Surface-Coated LiNi<sub>0.8</sub>Co<sub>0.1</sub>Mn<sub>0.1</sub>O<sub>2</sub> (NCM811) Cathode Materials by Al<sub>2</sub>O<sub>3</sub>, ZrO<sub>2</sub> and Li<sub>2</sub>O-2B<sub>2</sub>O<sub>3</sub> Thin-Layers for Improving the Performance of Lithium Ion Batteries. *Front. Mater. 6*, 309.
- Zhao, E.L., Zhao, S.X., Wu, X., Li, J.W., Yu, L.Q., Nan, C.W. and Cao, G. (2019). Electrochemical performance of Li<sub>2</sub>O-V<sub>2</sub>O<sub>5</sub>-SiO<sub>2</sub>-B<sub>2</sub>O<sub>3</sub> glass as cathode material for lithium ion batteries. *Journal of Materiomics, 5*, 663-669.

## CURRICULUM VITAE

**Name** Miss Jidapa Lomon

**Date of birth** April 15, 1994

**Contact** jiapalomon@gmail.com  
+66649487171

**Education** **2012-2016** B.Sc. (Physics) Ubon ratchathani university, Ubon ratchathani, Thailand.  
**2016-2019** M.sc. (Applied Physics) Suranaree University of Technology with Scholarship, Nakorn Ratchasima, Thailand.  
**2019-2023** Ph.D. (Applied Physics) Suranaree University of Technology with Scholarship, Nakorn Ratchasima, Thailand

**Publications**

Jidapa, L., Jintara, P., Amorntep, M., Sumeth, S., Narong, C., Yingyot, P., Supree, P., Prayoon., S. and Pinit, K. (2022). Effect of Ni content in lithium nickel borate glasses: Structure and electrochemical studies. Journal of Alloys and Compounds. 911, 164994.

Jidapa, L., Jintara, P., Amorntep, M., Sumeth, S., Narong, C., Yingyot, P., Supree, P., Prayoon., S. and Pinit, K. (2022). Nickel and manganese on lithium borate glass cathode for energy storage materials. Materialia. 26, 101583.

Jidapa, L., Jintara, P., Amorntep, M., Sumeth, S., Narong, C., Prayoon., S. and Pinit, K. (2023). Effect of Ni-Co transition metal ratios on structure-function of Lithium Aluminium Borate Glasses for battery electrode. Journal of Physics: Conference Series. 2431, 012066.